EFFECTS OF IRON AND NICKEL ON THE PROCESSING AND PERFORMANCE OF AN EMERGING ALUMINUM-COPPER-MAGNESIUM POWDER METALLURGY ALLOY

By

Eric D. Moreau

Submitted in partial fulfillment of the requirements
for the degree of MASTER OF APPLIED SCIENCE

at

Dalhousie University
Halifax, Nova Scotia
June 2012

DALHOUSIE UNIVERSITY

Department of Process Engineering and Applied Science

The undersigned hereby certify that they have read and recommend to the Faculty of Graduate Studies for acceptance a thesis entitled "EFFECTS OF IRON AND NICKEL ON THE PROCESSING AND PERFORMANCE OF AN EMERGING ALUMINUM-COPPER-MAGNESIUM POWDER METALLURGY ALLOY" by Eric D. Moreau in partial fulfilment of the requirements for the degree of Master of Applied Science.

Dated: June 21 2012

Supervisor: _____

Readers: _____

_____

Departmental Representative: _____

DALHOUSIE UNIVERSITY

DATE: June 21 2012

AUTHOR: Eric D. Moreau

TITLE: EFFECTS OF IRON AND NICKEL ON THE PROCESSING AND PERFORMANCE OF AN EMERGING ALUMINUM-COPPER-MAGNESIUM POWDER METALLURGY ALLOY

DEPARTMENT OR SCHOOL: Department of Process Engineering and Applied Science

DEGREE: M.A.Sc. CONVOCATION: October YEAR: 2012

_____

Signature of Author

Table of Contents

List of Tables

List of Figures

Abstract

Aluminum (Al) powder metallurgy (PM) provides a cost effective and environmentally friendly means of creating lightweight, high performance, near net shape components, relative to conventional casting/die casting technology. Unfortunately, the current lack of commercially available Al alloy powder blends has hindered development in this field as a result of the limited scope of mechanical properties available; especially under elevated temperature conditions common to many automotive applications. As such, the objective of this research was to attempt to improve the versatility of current Al PM technology through the incorporation of Fe and Ni transition metal additions into an emerging Al-4.4Cu-1.5Mg-0.2Sn alloy, as this technique is known to enhance the elevated temperature stability of wrought/cast Al alloys through the formation of stable, Fe/Ni aluminide dispersoids.

Initial experimentation consisted of evaluating the feasibility of incorporating Fe and Ni both elementally and pre-alloyed, through a series of tests related to their PM processing behaviour (compressibility, sintering response) and sintered product performance (ambient tensile properties). Results confirmed that pre-alloying of the base Al powder was the most effective means of incorporating Fe and Ni as all such specimens achieved properties similar or slightly superior to the unmodified alloy. Of the pre-alloyed systems considered, that containing 1%Fe+1%Ni displayed the most desirable results in terms of mechanical performance and microstructural homogeneity of the Fe/Ni dispersoid phases present in the sintered product.

Bars of the baseline system and that modified with pre-alloyed additions of 1Fe/1Ni were then sintered industrially to gain a preliminary sense of commercial viability and obtain additional specimens for elevated temperature exposure tests. Results confirmed that the sintering response, tensile properties and microstructures were essentially identical in both alloys whether they were sintered in a controlled laboratory setting or an industrial production environment. Furthermore, DSC data indicated that S (Al_2CuMg)-type phases were the dominant precipitates formed during heat treatment. The effects of elevated temperature exposure were assessed in the final stage of research. Both alloys were found to exhibit comparable behaviour when exposed to the lowest (120°C) and highest (280°C) temperatures considered. Here, the alloys showed no obvious degradation at 120°C. Conversely, exposure at 280°C prompted a steady decline in yield strength for both alloys with significant precipitate coarsening noted as well. Despite these similarities, differences emerged during isochronal tests at intermediate temperatures. Here, DSC data indicated that the precipitates present in the pre-alloyed material were stable at temperatures up to 160°C while those in the unmodified alloy had begun to overage under the same exposure conditions. These differences were accompanied by increased stability in tensile yield strength for the pre-alloyed material. In all, this study has indicated that the use of Al powder pre-alloyed with Fe/Ni additions is feasible for press-and-sinter PM technology and that the sintered product exhibits improved elevated temperature stability under certain conditions.

List of Abbreviations and Symbols Used

Item	Description
θ	$CuAl_2$ precipitate
θ'	Metastable $CuAl_2$ precipitate
θ'' (GP2 Zones)	Guinier-Preston II Zones
ρ	Density
AA2014	Wrought alloy Al-4.4Cu-0.8Si-0.5Mg
PM2014	PM equivalent of wrought AA2014
Alumix 123	Commercial PM2014 alloy
BCT	Body Centered Tetragonal
D_i	Initial dimensional measurement
D_f	Final dimensional measurement
DSC	Differential Scanning Calorimetry
E	Young's Modulus
EC	Evaporation-condensation
EDS	Energy Dispersive Spectroscopy
F	Force
FCC	Face Centered Cubic
GBD	Grain Boundary Diffusion
G.S	Green Strength
L	Length
LPS	Liquid Phase Sintering
M	Mass
IM	Ingot Metallurgy
OAL	Overall Length
PLP	Persistent Liquid Phase
PM	Powder Metallurgy
S	Al_2CuMg
SD	Surface Diffusion
SEM	Scanning Electron Microscopy
SSSS	Super Saturated Solid Solution
T	Temperature
t	Thickness
T1	As-sintered heat-treatment

T6	Solutionized and artificially aged
TLP	Transient Liquid Phase
TRS	Transverse Rupture Strength
UTS	Ultimate Tensile Strength
V	Volume
VD	Volume Diffusion
W	Width
XRD	X-Ray Diffraction

Acknowledgements

The author would like to acknowledge the work of Dr. D.P Bishop, for his support and leadership throughout the entirety of this project. Furthermore, the author would like to thank Dr. Georges Kipouros and Mr. Ian Donaldson for their input. I would also like to extend my gratitude to the staff at GKN Sinter Metals in Conover, North Carolina for their technical support. I would also like to thank the Powder Metallurgy group at Dalhousie University including, Randy Cooke, Clark Murray, Winston Mosher, Dan Cluff, Gavin Steedman and Logan Smith. Furthermore I would like to acknowledge the technical support staff at Dalhousie University including, Mr. Dean Grijm, Mr. Ray Dube, and Mrs. Patricia Scallion as well as Dr. Stephen Corbin for his assistance with DSC experiments.

Chapter 1 Introduction

Powder metallurgy (PM) is the science of the consolidation of powder particles through elevated pressure and/or temperature in order to create near net shape components possessing mechanical properties similar those obtained through Ingot metallurgy (IM). The advantages of PM over conventional IM include, but are not limited to:

- Tight dimensional tolerance
- Near-net-shape
- ~ 100% material utilization
- Unique properties (controlled porosity)
- High throughput
- Material flexibility
- Reduced secondary operations (i.e. machining)

Near-net-shape and tight dimensional tolerance are the greatest advantages of PM, relative to IM. Cast products require a considerable amount of secondary machining in order to attain the required dimensional tolerances and to remove process-related features such as sprues and risers. This adds considerably to operational costs and negatively impacts the efficiency of material utilization. PM is also a very versatile material forming technique commonly used in the creation of a wide variety of metals, alloys, composites, ceramics, etc.. Since the majority of the powder particles remain in the solid state during consolidation, high-temperature refractory materials can be produced at much lower sintering temperatures. Also, as a result of the rapid solidification rates employed during powder atomization, equilibrium-based solubility limitations can be surpassed and a greatly refined dispersion of secondary phases can be realized.

Unfortunately, relative to their fully dense wrought counterparts, most PM components exhibit some degree of porosity which typically reduces mechanical properties. This behaviour is particularly pronounced in the ductility of PM parts, and therefore full-density processing techniques are generally applied in cases where optimal performance is required at the expense of process efficiency and cost.

PM processing ultimately begins with the creation of one or more powders through techniques such as mechanical comminution, chemical deposition, atomization, etc.. The finished powder is then generally screened to the desired particle size distribution to modify its packing and flow characteristics. Next, depending on which powder forming technique is used the powder is blended along with other elemental or alloyed powders, lubricants, dispersants and binders to attain proper homogeneity of the desired alloy chemistry and facilitate forming respectively. The properly blended powder is then formed into the desired shape (so called "green body") using some means of compaction such as uniaxial die-compaction, cold/hot isostatic compaction, metal injection moulding, etc.. Green bodies are then heated in a furnace under controlled atmosphere through an appropriate thermal profile. If delubrication of the powder compact is necessary, it is first held at intermediate temperature for a period of time after which it is then heated to the sintering temperature and held once again. In some full-density operations such as hot-isostatic pressing, pressure and heat are applied simultaneously, providing thermal softening which facilitates densification. At this point the as-sintered material is, for the most part, complete. However, secondary operations such as heat treatment, repressing, and de-burring are commonly performed to modify the mechanical properties and improve dimensional accuracy.

Aluminum PM has recently begun to receive a great deal of attention due to appealing attributes that include good compressibility, a high strength to weight ratio, excellent thermal conductivity, good corrosion resistance, etc.. For instance, Aluminum PM blends are known to compact to relatively high green densities under relatively low pressures. Once sintered, many of these alloys exhibit near-full densities (> 99% of theoretical) and as a result, relatively high mechanical properties for as-sintered PM alloys. At present, Aluminum PM alloys are typically utilized in the manufacture of automotive engine components such as gears and bearing caps where they substitute for ferrous components so as to impart considerable weight savings. For instance, a considerable amount of research and development has been invested in the creation of Aluminum Silicon carbide metal matrix composites for automotive applications via PM processing [1-4]. The addition of SiC reinforcement yields considerable improvements in the properties of Aluminum alloys, such as the coefficient of thermal expansion, wear resistance, strength

and stiffness with only a minor increase in the overall density. The following sections will briefly examine the fundamental principles of PM and the current state of commercial Aluminum PM processing.

1.1 Powder Fabrication: Atomization

Particulate materials are commonly manufactured through the application of mechanical communition, chemical and electrolytic precipitation, liquid metal atomization, etc.. Each technique instils unique properties (particle morphology, size distribution, and chemistry) and characteristics to the powder. Such properties have a significant effect on the compressibility and sintering response of powder compacts and therefore must be considered when choosing a proper powder manufacturing process. Costs, production rates, and quality also play a pronounced role in determining which method is ultimately used. For example, rod or ball mills are relatively inexpensive and have reasonable output rates. However, the powders they produce typically suffer from contamination and possess a relatively wide particle size distribution. Conversely, those formed via electrolytic decomposition are typically characterized by exceptionally high purity and a very fine mean particle size albeit at the expense of low yields and increased costs [5].

A more common technique employed in the production of metal, alloy and intermetallic powders is atomization of a molten metal stream via high pressure gas into droplets that solidify within a sealed vessel [6]. Denoted as gas atomization, the advantages of this technique relative to mechanical and chemical methods are an exceptionally high output rate, better control over powder particle characteristics, and the ability to create spherical and nodular powders which are highly desirable in terms of their flow and packing characteristics. Figure 1 schematically illustrates the appearance of horizontal and vertical gas atomization arrangements. The former are typically used for low melting point metals such as Tin and Lead, while the latter are employed for higher melting point metals (Al, Fe, Cu, etc.)..

Horizontal atomizers take advantage of the high velocity gas that passes through the atomizer nozzle thereby creating suction of the melt and subsequent atomization. The powder particles then accumulate in a chamber designed to filter the gas from the

particulates. In contrast, vertical atomizers operate in a manner whereby the melt is gravity fed into the atomization zone. Upon exiting the nozzle, the stream is atomized by the rapid depressurization of a gas (air, He, N_2, Ar). This disrupts the stream into many droplets that solidify in-flight and are eventually collected at the bottom of the atomizing chamber. Most vertical atomizers are also equipped with a cyclone as a means of separating out the finest particles and thereby avoiding their re-entry into the atomization zone when the gas is recycled. Such particles can also represent a considerable safety hazard which also warrants their removal.

Figure 2 provides a detailed schematic representation of how a depressurizing gas impinges on a gravity fed stream of molten metal. Initially, it creates a gas expansion zone which disrupts the stream, so as to shear it into sheets. The sheets then become increasingly more spherical as the allowable solidification time is prolonged. Techniques such as superheating the melt and using gasses with higher thermal conductivities may be practiced to effectively reduce the solidification rate, yielding finer and more spherical powders. Figure 2 also illustrates the close proximity of the gas nozzles to the melt stream required for effective gas atomization.

During gas atomization, the median particle size (D_{50}) can be approximated using the mass flow rates of the liquid metal $\dot{M}_M$ and the atomizing gas $\dot{M}_G$ in addition to the constants, N and α. N typically varies between 0.5 to 1.0 as a result of differences between the design and efficiency of gas atomizers, while α is parameter that is dependent upon the nozzle design, gas type, melt temperature, and pressures. Although α may be difficult to approximate, the mass flow rates have a much more significant impact on the particle size as shown in the following equation [7]:

$$D_{50} = \alpha \left[\frac{\dot{M}_M}{\dot{M}_G}\right]^N \qquad \textbf{Equation 1}$$

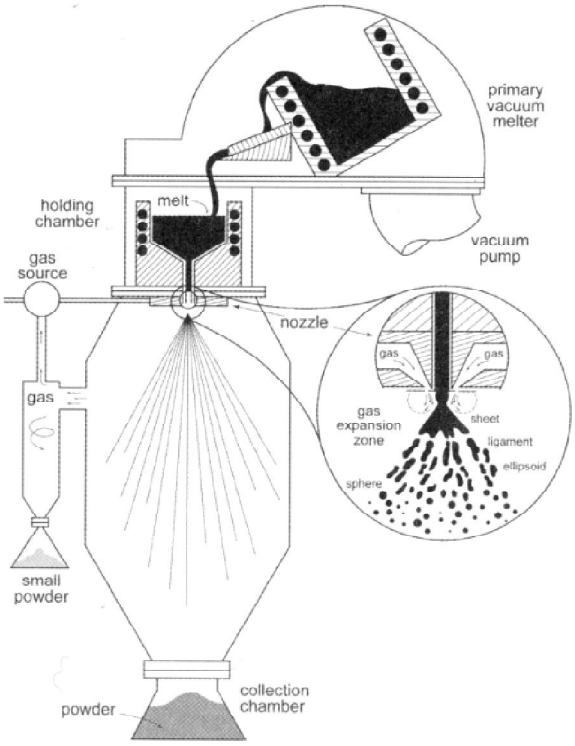

(a)

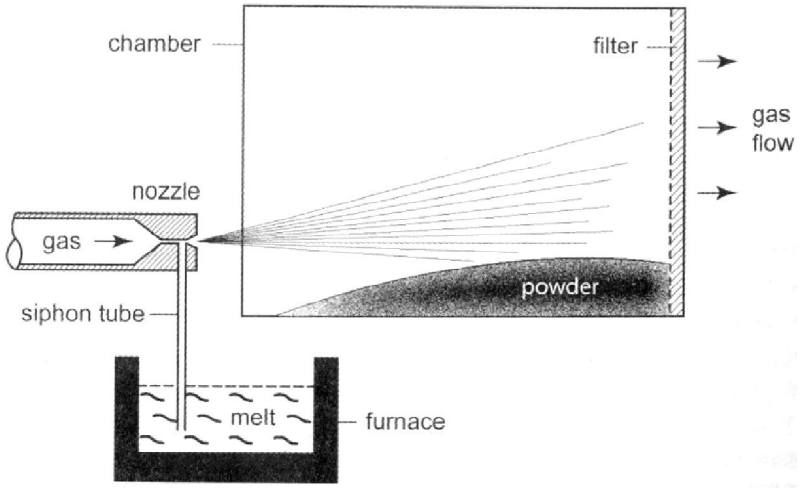

(b)

Figure 1 – Schematics of common gas atomization systems. (a) Vertical and (b) horizontal arrangements [5].

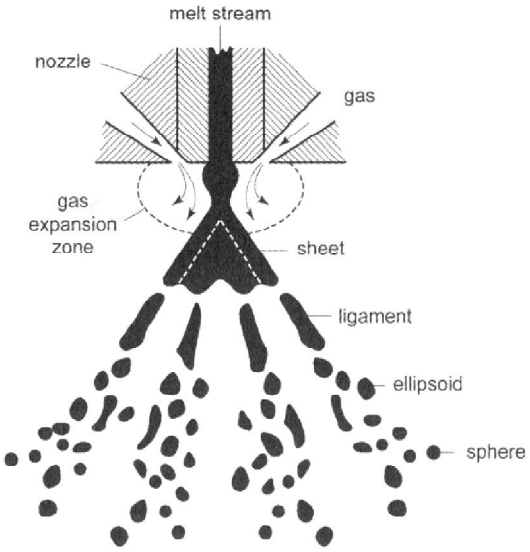

Figure 2 – Schematic of gas atomization illustrating the evolution of the disturbed liquid melt into progressively more spherical powder particles [5].

Therefore, reducing the mass flow rate of the melt and increasing the gas flow rate will decrease the median particle size of the atomized powder. More efficient transfer of the gas expansion energy to the melt stream can be achieved using close-coupled gas nozzles. In which case, the median particle size can be determined using the following refinement of the previous equation [7]:

$$D_{50} = Kd \cdot \left[1 + \frac{\dot{M}_M}{\dot{M}_M}\right] \cdot \frac{1}{We}\left(\frac{\eta_M}{\eta_G}\right) \qquad \textbf{Equation 2}$$

Where K is an empirical constant, d is the diameter of the melt stream, η_M and η_G are the viscosities of the melt and gas respectively, and We is the dimensionless Webber number which takes into account the effect of the inertia and surface tension of the melt. Since gasses typically have far lower viscosities then liquid metals, one means of reducing the median particle size is by increasing the superheat of the metal which generally decreases viscosity. Furthermore, the increased heat would reduce the solidification rate yielding more spherical particles.

An alternative to gas atomization of liquid metal is centrifugal atomization via the rotating electrode process. Here, a potential is applied between a tungsten cathode and a rod of the desired powder composition (anode) as it is rotated and slowly fed toward the cathode. When the separation between the two electrodes reaches a certain distance an electrical arc is created that continuously melts the tip of the anode, as shown schematically in Figure 3. Increasing the rotational velocity of the anode yields an increase in the centrifugal force, and hence a decrease in the median particle size [6]. A fine particle size many also be realized through the use of relatively high density metals and increasing the radius of the anode. One disadvantage of this technique is that despite its high melting point, the tungsten cathode is gradually consumed and therefore must be carefully monitored to ensure adequate electrode working distance and minimized contamination of the powders. Powders produced through this technique possess a narrow particle size distribution and exhibit high packing densities and exceptional flow characteristics, as a result of their large (>200μm) and highly spherical nature.

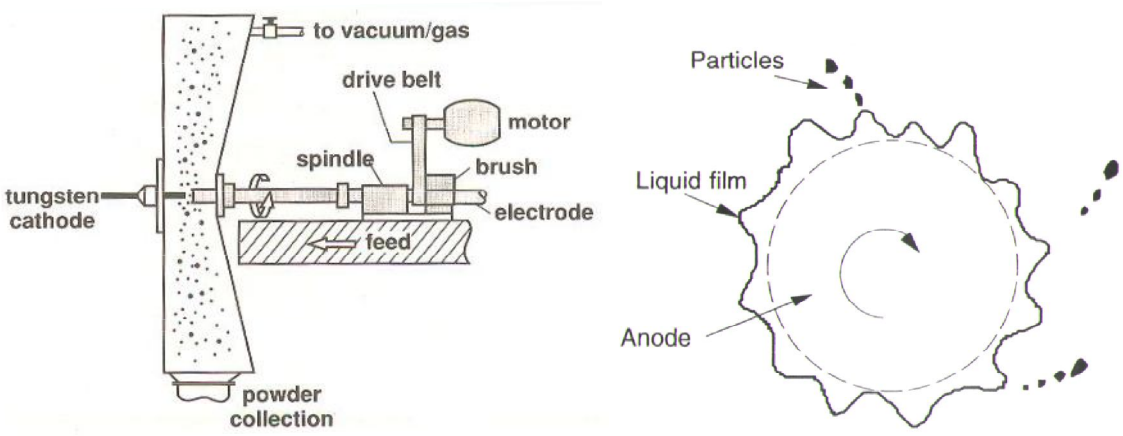

Figure 3 – Schematic of a typical rotating electrode atomization apparatus (left) and liquid film break up at the tip of the anode (right) [5][8].

Preventing cooling induced chemical segregation and the creation of amorphous powders are two examples of circumstances where rapid solidification is desirable. In such scenarios, several variations of the centrifugal atomization technique exist, yet they all follow the same principal of using centrifugal force and cooled melt collision plates to rapidly solidify the molten metal and break it up it into small particles. The powders

created are usually of a large flake or ribbon-type morphology and therefore require further processing such as milling to further reduce their size.

Water is a common alternative to using gasses in the atomization of less reactive metals such as Iron, steel, and Copper. Metallurgical grade Iron powder is commonly produced from scrap Ironvia arc melting and water atomization followed by a series of purification, annealing and milling steps, as illustrated in Figure 4. Scrap Iron provides an abundant and inexpensive feedstock that can be easily water atomized once melted down using an electric arc furnace. Water is generally used for its low cost and availability as well as the superior solidification rates achieved due to its high specific heat capacity. The disadvantages of water atomized powders are their elevated oxygen content, the common need for additional processing steps to alleviate residual stress, and their lower apparent density relative to gas atomized counterparts.

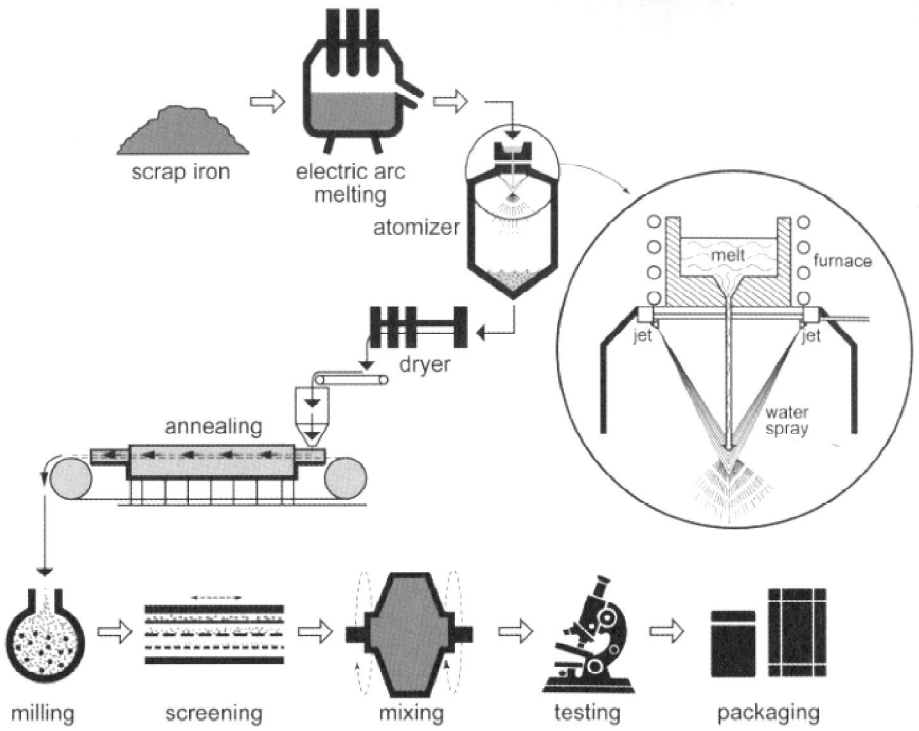

Figure 4 – The water atomization process for Iron powder [5].

Due to the highly reactive nature of molten Aluminum, air and inert gas atomization are the most common methods used to create Aluminum-based powders. Furthermore, air atomization is preferentially used given its lower cost, superior thermal conductivity, and

the requirement that Aluminum powders be intentionally oxidized to reduce the likeliness of explosion during transportation and handling. The process adopted by Alcoa for the atomization of Aluminum and Aluminum alloy powders is shown below in Figure 5. In this process, molten metal supplied by the melting/holding furnace is sent to the atomizing bay where it is heated to the required temperature before being drawn to the nozzle by the aspirating effect of the high-pressure compressed air output located in the nozzle. As the melt encounters the high-velocity gas, the liquid is broken up into droplets and sprayed as a jet within the atomizing chamber. The atomized droplets are quickly solidified into powder particles by the chilled gaseous atmosphere, and then sent through ducts to the cyclones. Finally, the powders are classified according to their size using a series of screens and then packaged for transport via truck or railroad cars, all under inert gas atmosphere.

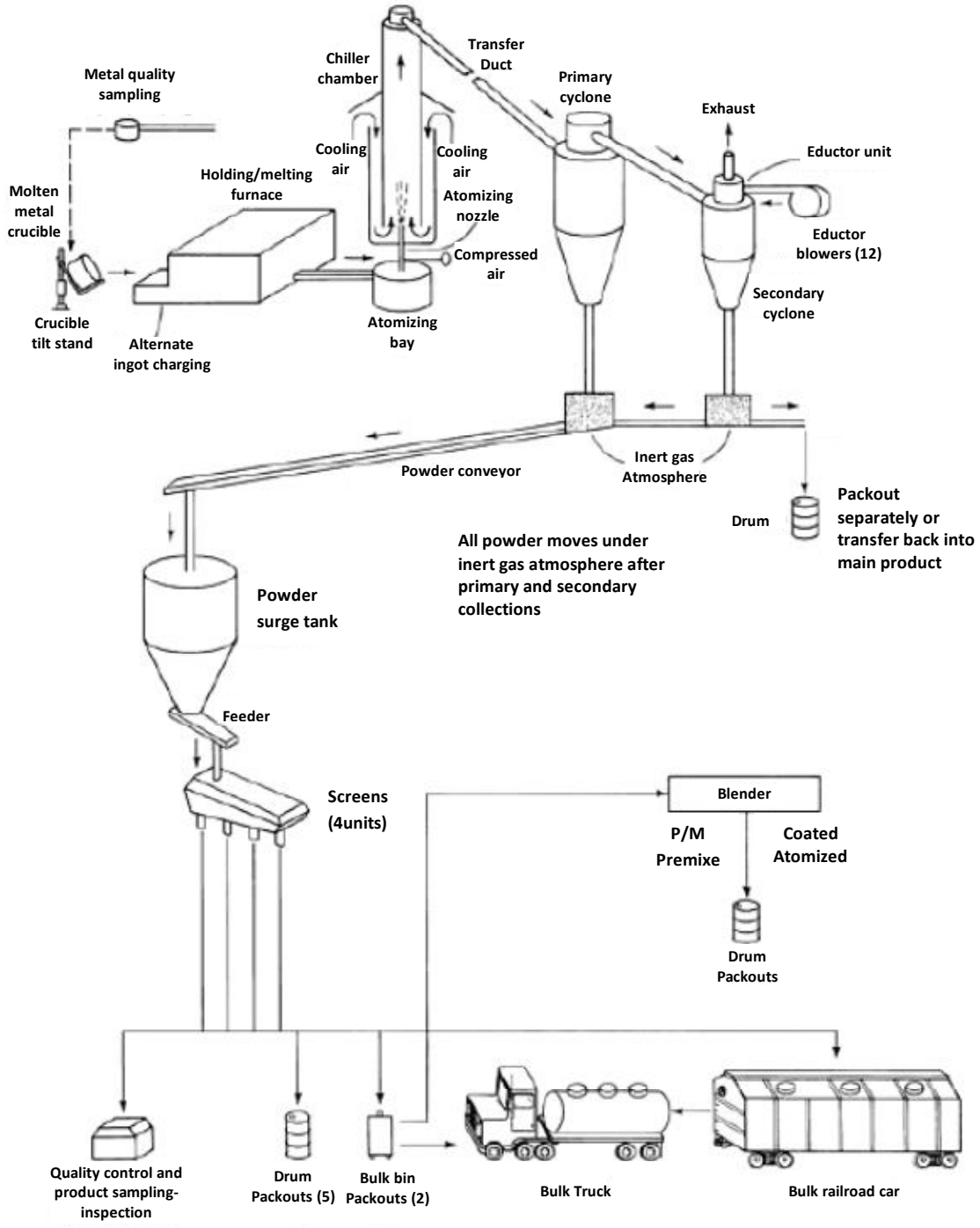

Figure 5 – Schematic of the Alcoa computer controlled process for producing atomized Aluminum powders [9].

1.2 Powder Blending/Mixing

Once the desired powder(s) have been created, the next step in PM processing is blending to achieve a homogenous mixture. Blending is required as commercial powders typically exhibit a distribution in particle size, rather than a narrow range. This is advantageous as such powders exhibit superior packing characteristics therefore aiding subsequent compaction processing. Large particles tend to flow better and are far more compressible than small particles, yet small particles are preferred as they typically result in superior chemical homogenization during sintering. It is therefore desirable to have a combination of small and large particles, for their individual attributes as well as the superior packing density achieved with their combination as illustrated in Figure 6.

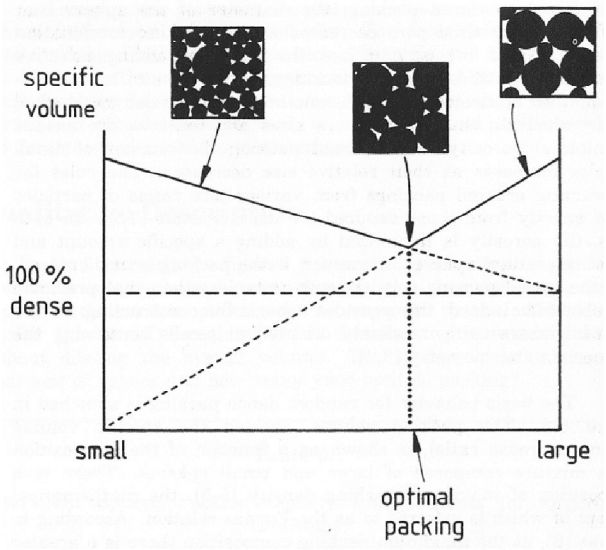

Figure 6 – Hypothetical diagram of apparent density as a function of the ratio of small to large particle sizes [10].

In industry, dry blending of powder particles is achieved through three primary mechanisms: diffusion, convection, and shear (Figure 7) [5]. Diffusion occurs due to the displacement of individual powder particles throughout the powder lot. In a rotating

drum, diffusion mixing is achieved via continuous break down of the outer edge shear plane of the powder bed as a result of the powder being raised against the flow, continuously introducing fresh powder and shear planes. Convection mixing is defined as the displacement of a group of adjacent powder particles throughout the batch from the lower surface, while shear mixing is achieved through continuous division and flow of the powder particles over slip planes [5]. In practice, all three modes of mixing are active and responsible for adequate blending.

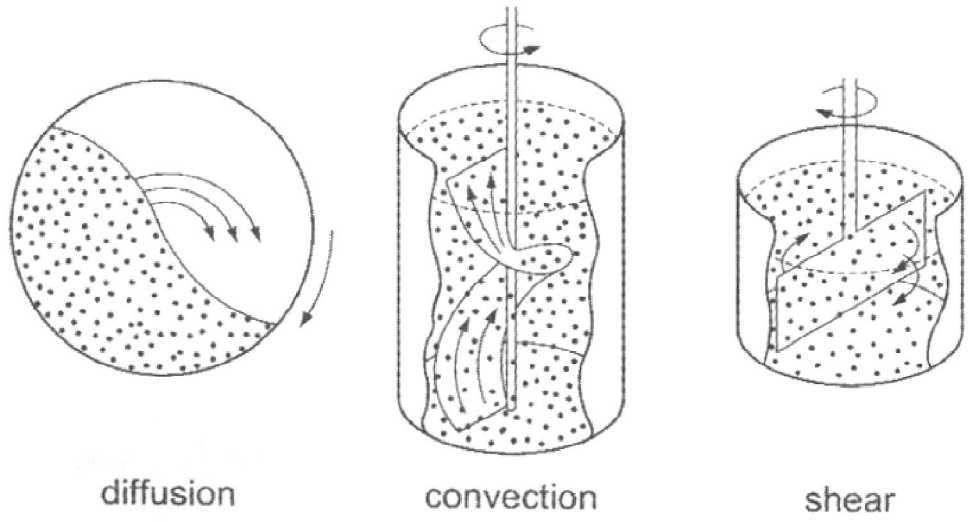

Figure 7 – The three primary modes of dry powder mixing [5].

Aside from preparing a starting homogenous blend, powder blending is also frequently applied to commercial blends immediately prior to use. Here, the goal is to mitigate the inevitable occurrence of settling that transpires when the blend is shipped from the producing facility to the end user. For powders of a single chemistry, such blending reduces the preferential rearrangement and flow of finer particles. For those possessing multiple chemical constituents, blending is required to reduce settling effects that stem from differing particle densities, shapes, and sizes (Figure 8).

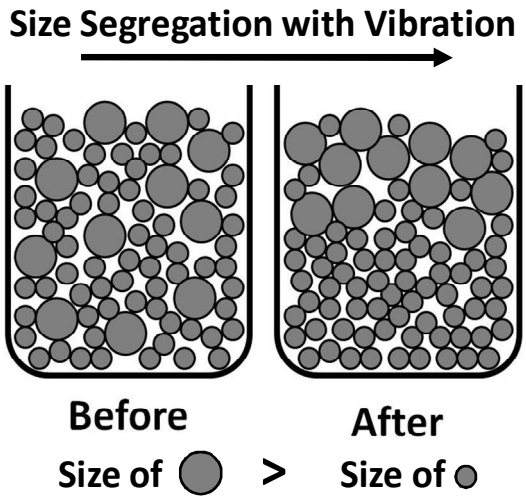

(a)

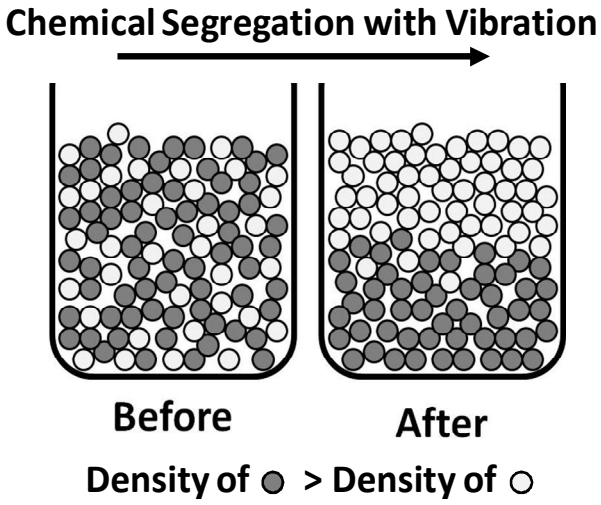

(b)

Figure 8 – Schematic illustrating (a) size and (b) chemical segregation resulting from vibration of the powder blends.

1.3 Powder Compaction

Once a powder has been properly blended it requires some form of consolidation to achieve its desired shape with sufficient green strength for handling. Highly compressible and relatively inexpensive powders such as Aluminum, Iron, and Copper are typically formed using die compaction. This technique has enjoyed a great amount of commercial use in the production of gears, connecting rods, self-lubricating bearings, and cam shaft bearing caps to name but a few of the many automotive components produced. Industrially, uniaxial die-compaction is revered for its use in high throughput production of small (< 250 cm^2) components possessing tight dimensional tolerance. Die compaction is, at present, the most commonly practiced technique employed in the shaping of powders into a desired shape. As such, a great deal of interest has been devoted towards a better understanding of the role that key parameters (pressure, tooling complexity, component size, die wall friction and the intrinsic material properties of the powder) have on the attributes of the green compact as well as the as-sintered component.

Fundamentally, die compaction (a.k.a. uni-axial die compaction) consists of filling the die with the powder + lubricant blend, followed by the application of pressure via an upper and/or lower punch. Once the desired pressure is attained the punches are typically held for a brief period prior to withdrawal and subsequent ejection of the green compact. During this process, the density of the powder enclosed in the die increases from its initial apparent density, or loose packing condition as the particulates are rearranged as a result of the applied force (Figure 9). As the powder particles continue to rearrange themselves, their coordination number increases linearly with increasing density. Densification becomes progressively slower as the large pores are eliminated. Furthermore, greater stresses are required to reduce the remaining porosity since the particles become significantly work hardened and in turn, less compressible. The contribution of each stage to the overall densification of a powder is shown in Figure 10, as a function of increasing compaction pressure. In practice, most die compaction operations achieve localized/homogenous deformation, as higher pressures generally require longer processing times, greater tooling wear, and require large presses which increase in cost exponentially with higher pressure capabilities.

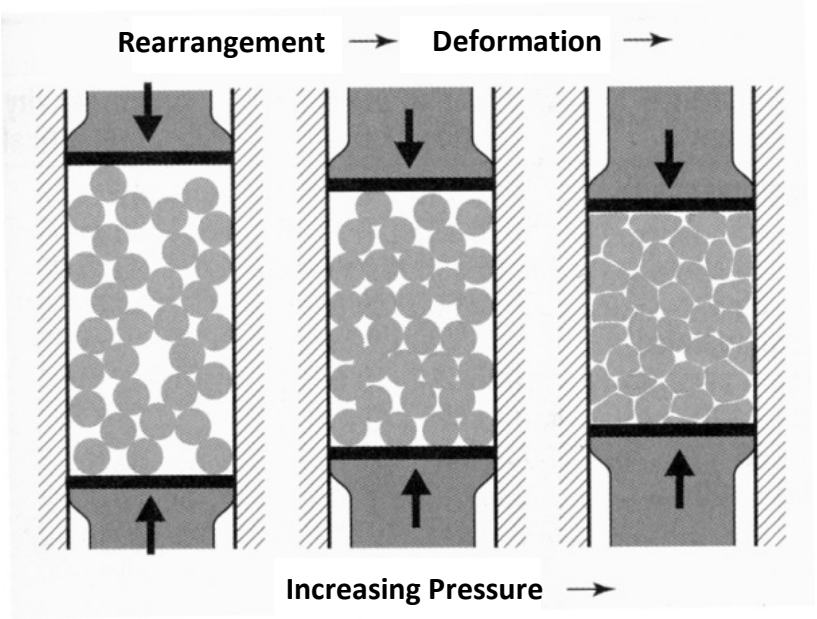

Figure 9 – Basic stages in powder compaction [5].

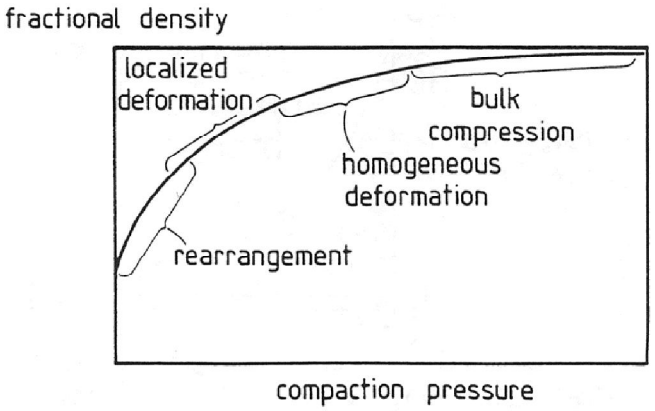

Figure 10 – Idealized plot of fractional density versus compaction [10].

Uni-axial compaction is commonly classified as either single action or double action depending on whether or not the lower punch is fixed. Alternatively, double action pressing can be simulated using a fixed lower punch and a floating die through the motion of the upper punch and friction induced motion of the die made possible by several springs fixed between the lower punch and the die. Figure 11 provides a more detailed step-by-step illustration of the double action compaction process typically used

in industrial PM processing. Here, the lower punch is first lowered to allow the powder feed from the feed shoe to fill the die. After the upper punch is lowered to the powder, both punches exert pressure on the powder in opposing directions. Finally, once the desired pressure is achieved the upper punch is raised followed by the lower punch, ejecting the green compact.

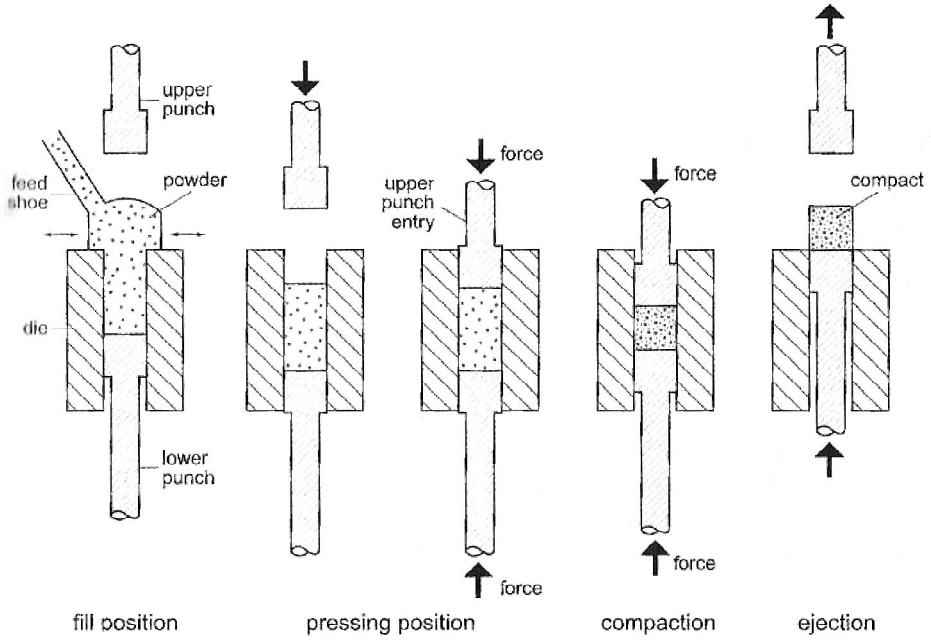

Figure 11 – Stages of a typical double action compaction process [5].

Die pressing technology necessitates the use of a lubricant, whether applied directly to the die or admixed with the powder during blending. The cause of this is the presence of friction generated between the die wall and the powder during compaction. Termed die wall friction, this phenomenon disperses the applied stress in the form of heat, creating pressure gradients, which are then manifested as density gradients in the green compacts, as shown in Figure 12. Once sintered, such compacts may exhibit uneven shrinkage, warpage, inhomogeneous mechanical properties, etc., if the gradients are not carefully controlled and accounted for. Other reasons for using a die wall lubricant include increased tooling life and the reduced likelihood of generating defects during compact ejection.

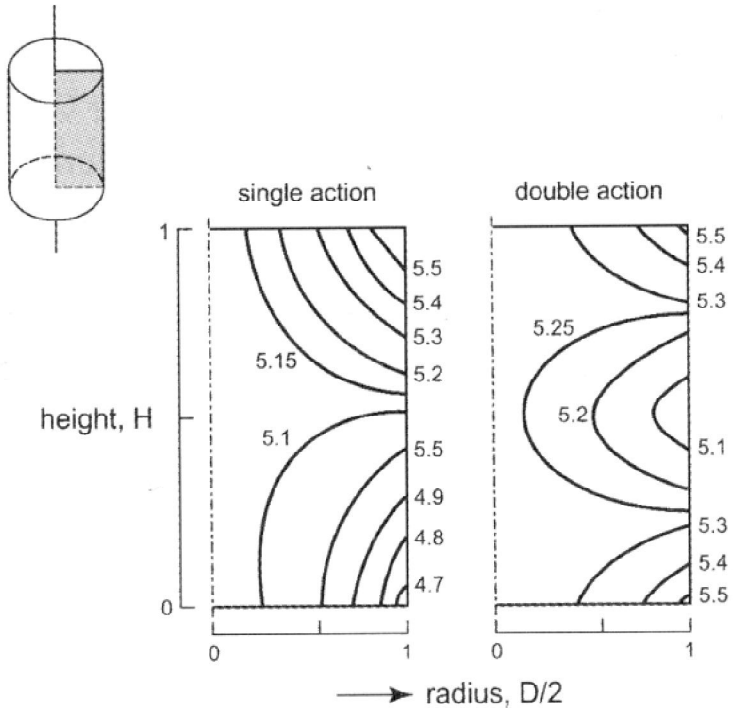

Figure 12 – Schematic of the density gradients present in single and double action die-compaction (contours in g/cm^3) [5].

During ejection the green compact undergoes expansion, or "springback" due to the release of the compressive pressures that had previously constrained the compact within the die cavity. Springback is beneficial in that it prevents the green compact from falling back down into the die after ejection. However, if the expansion is too severe it may lead to delamination and cracking. Lubricants reduce the force required to eject the powder compact after being pressed, and in turn, the likelihood of springback related defects. Figure 13 shows the progression of the stress created during ejection. The maximum stress observed is that required to surpass the initial adhesive friction between the powder compact and the die wall. The measured fracture stress of a powder compact obtained using a 3-point bend test can provide a rough indication of whether or not a powder compact can be successfully ejected without detrimental defects.

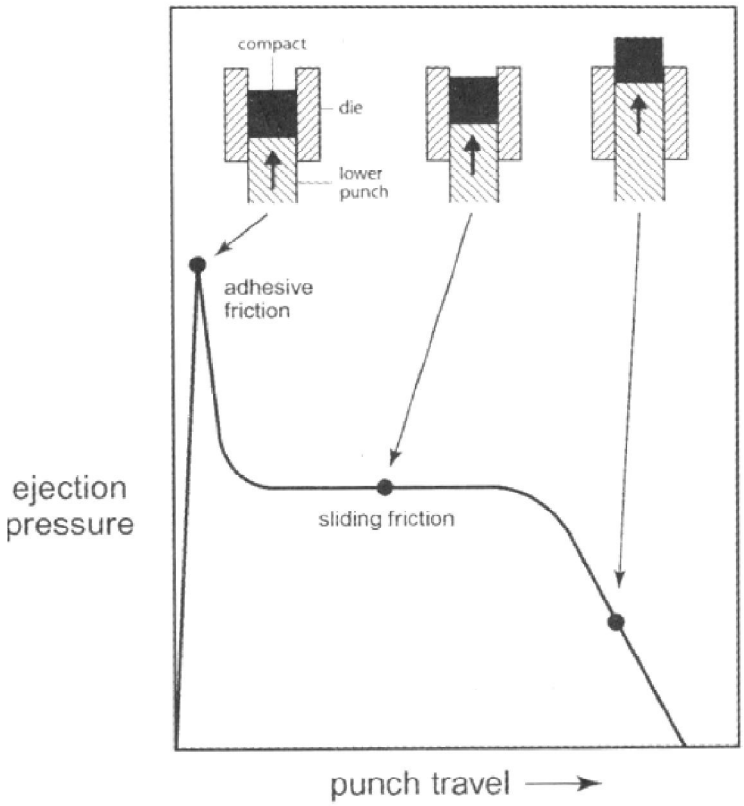

Figure 13 – Ejection pressure versus punch travel during ejection of the powder compact from the die [5].

The geometry and size of PM components are critical aspects taken into consideration when determining whether or not a design is feasible for die compaction. For example, squat shapes possessing small H:D (Height to diameter) such as gears and connecting rods are ideal for die compaction, while tall shapes with small diameters (cylinders) are generally formed by alternate means (i.e. cold isostatic compaction).

Commercial Aluminum-based PM blends are generally processed using die compaction, given the relatively low cost and exceptional compressibility exhibited by such powders. Figure 14 compares the fractional densities attained by several materials as a function of compaction pressure. Clearly, Aluminum can be compacted to very high densities at relatively low pressures. The fractional density which asymptotically reaches a plateau at approximately 200 MPa indicates the point at which additional gains in density resulting from increasing pressure are negligible.

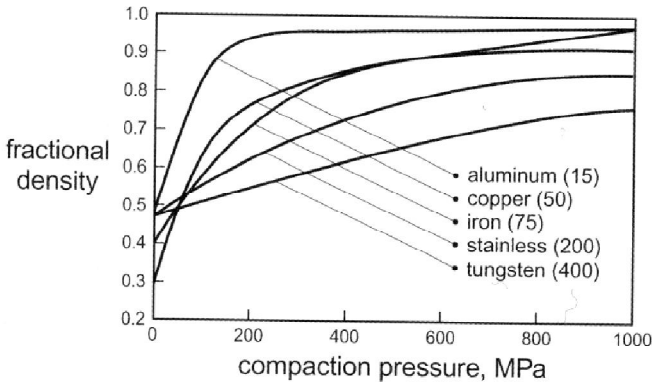

Figure 14 – Plot of fractional density versus compaction for various metals, illustrating the exceptional compressibility of Aluminum [5].

Most Aluminum PM alloys contain Copper, Magnesium, and Silicon in variable concentrations, and therefore adequate compaction requires sufficient pressure to accommodate the lower compressibility of the alloying additions. Furthermore, pre-alloyed and master alloy powders, as commonly used in commercial PM systems, are considerably harder and prove to be significantly more difficult to compress [11]. Therefore, when identifying a particular processing route the advantages and disadvantages of using alloyed powders must be carefully evaluated. Additionally, Aluminum powders designed for die pressing are generally large and soft, as these attributes improve packing, flow, and compressibility.

1.4 Sintering

Sintering is a thermal process used to improve the bulk mechanical properties of a mass of powder particles after preliminary consolidation. Such elevated temperature exposure enhances atomic mass transport mechanisms thereby enabling interparticle bonding as a result of the inherent driving force to reduce the surface area to bulk volume ratio of the compressed powder compact. This material processing technique greatly improves the mechanical properties of the fragile green compact, making PM a very efficient means of manufacturing high tolerance, near-net shape components.

1.4.1 Liquid Phase Sintering Theory

Although often completed as a solid state process, sintering may also be assisted by the presence of a liquid phase depending on the temperature and alloy chemistry. This form of sintering is generally preferred due to the enhanced densification enabled through capillary forces and superior diffusion rates within the liquid. Termed liquid-phase sintering (LPS), this approach is employed in thousands of different material systems on an industrial scale. However, it is a complex process and if completed in the presence of an excessive amount of liquid, slumping and warpage often ensue. Nonetheless, LPS remains the dominant commercial/industrial method used in the sintering of a wide variety of materials (in particular, Aluminum alloys) and will therefore be reviewed in some detail.

In LPS, the sintering temperature is generally above the solidus line, allowing the formation of a liquid phase which enhances sintering through capillary forces, and improved mass transport rates within the liquid. LPS can further subdivided into persistent, transient and super solidus liquid-phase sintering, depending on the behaviour of the liquid phase during the course of sintering. Classical LPS involving the formation of a liquid that does not react extensively with the solid phase is shown in Figure 15. Initially the mixed powders consist of the base powder (grey solid), the liquid forming additive (black), and a considerable amount of porosity (white). As sintering progresses, the additive melts and wets the surface of the solid base powder within the network of pores. This enables the liquid to flow into the micro pores thereby giving rise to capillarity forces that act on the solid particles. Such forces cause the solid grains to rearrange themselves into a more cohesive structure. Termed particle rearrangement, this stage of the LPS process provides the first major increase in fractional density. Next, dissolution of the smaller grains into the liquid occurs followed by reprecipitation on to the larger grains. This stage causes the average grain size to approach a more uniform value as well as grain shape accommodation through a flattening of the facets on adjacent particles. The net result is a continuance in porosity removal and additional gains in densification, as shown in Figure 16. Eventually, the sintering structure reaches a condition where significant contact between solid grains occurs and the bulk of porosity

is removed. At this point, further densification is only possible through solid state sintering. This is known as the final stage of LPS but is typically not achieved in practice given that the corresponding gains are minor and are achieved at a rate that is prohibitively slow.

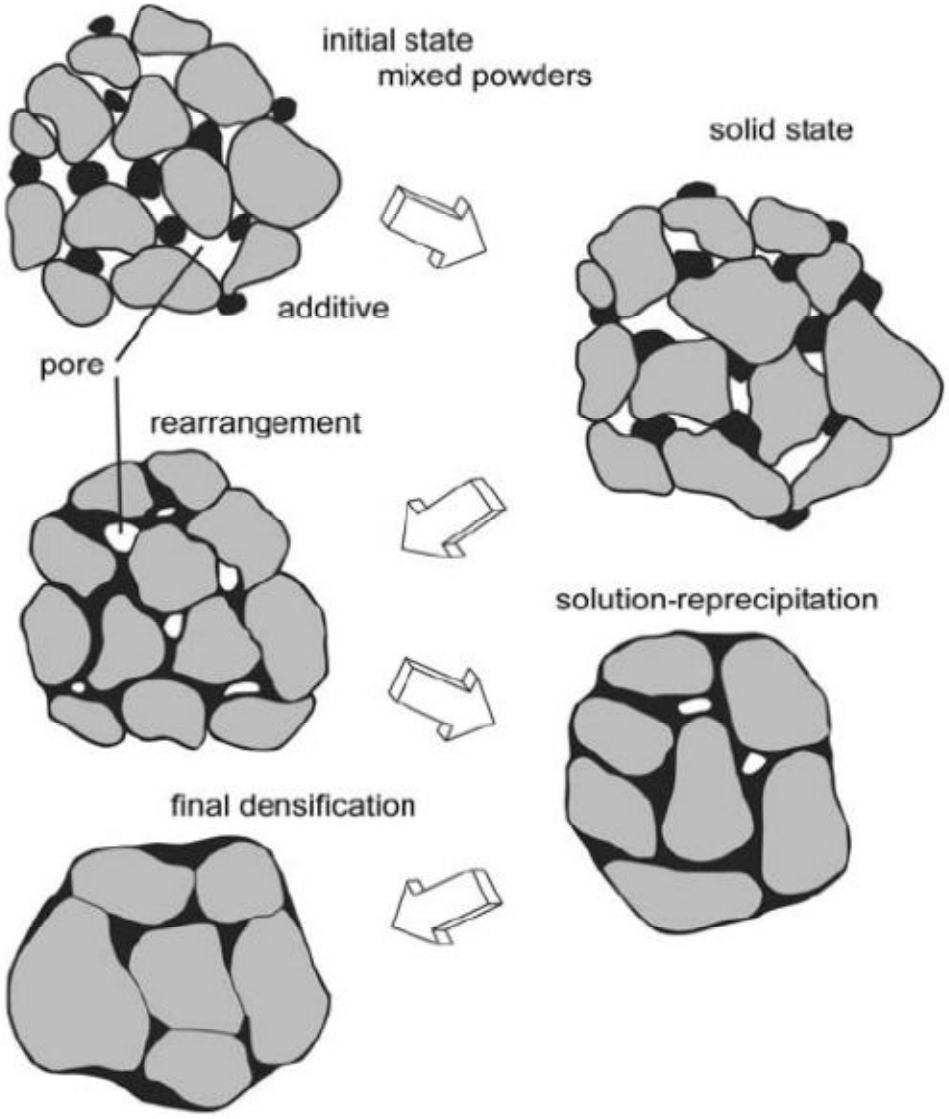

Figure 15 – Stages of liquid phase sintering [12].

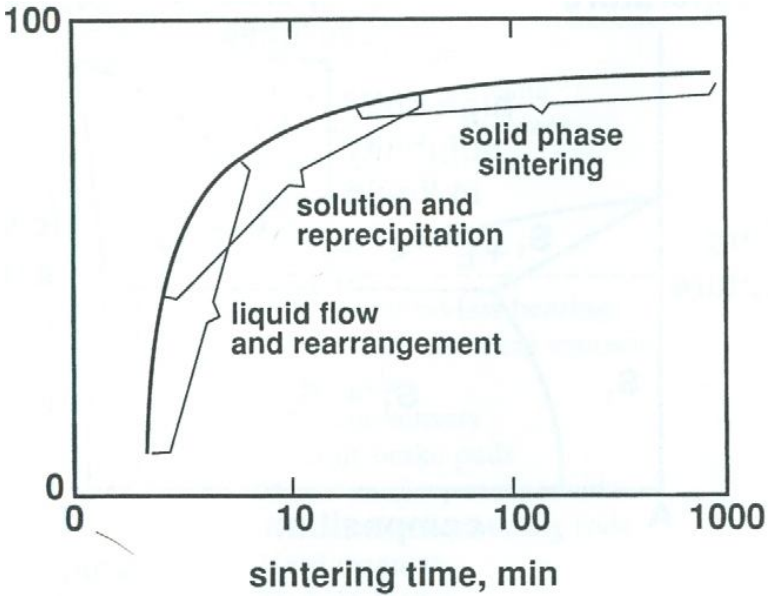

Figure 16 – Contribution of each stage of LPS to densification versus sintering time [13].

The presence of a solid-liquid-vapour interface during LPS makes the wetting behaviour of the melt on the solid surface a significant factor on the final microstructure and mechanical properties. At low interfacial energies wetting is favoured and the liquid clings to solid phase where it provides bonding between powder particles and allows grain shape accommodation and rearrangement through capillary phenomena. In contrast, poor wetting behaviour leads to generally undesirable swelling of the compact, as well as possible exudation of the melt from the compact. Chemical interactions at the solid-liquid interface generally indicate good wetting, as commonly seen with metals of high oxygen affinity exhibiting wetting of metallic oxides, and systems where the liquid is highly soluble in the solid phase.

When conditions are such that the sintering temperature is above the alloy solidus, the solid phase has a high solubility in the liquid phase, and the liquid phase has a low solubility within the solid (Figure 17) a stable liquid is formed [12]. Known as persistent liquid phase sintering (PLPS), this style of LPS typically leads to extensive densification through a combination of good wetting and solubility properties. Conversely, when the solid phase has low solubility in the liquid and the liquid has a high solubility in the solid

(Figure 18), transient liquid-phase sintering (TLPS) transpires. Here, a liquid is formed when the powders initially react but eventually dissolves into the solid phase as a result of the high solubility. Sintering under TLPS is typically difficult to control in a robust manner and often yields a product with inferior sintered density.

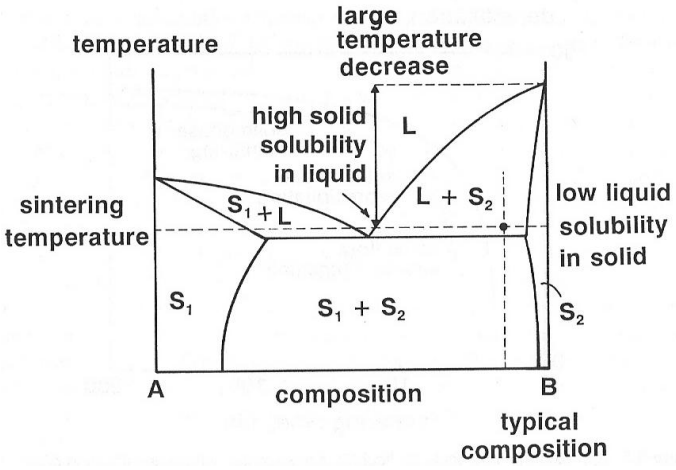

Figure 17 – Hypothetical binary diagram illustrating solubility and temperature requirements for PLPS [12].

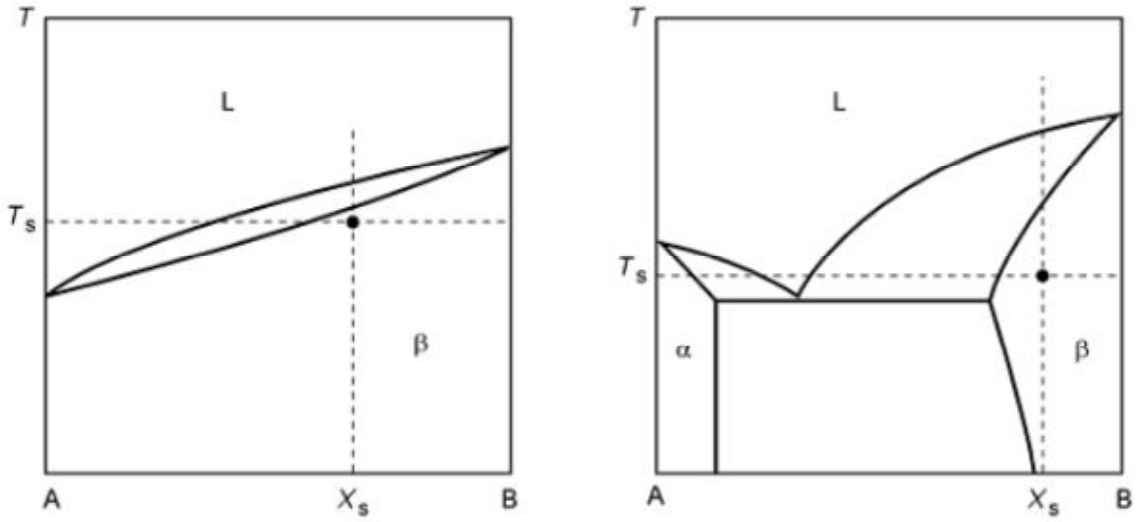

Figure 18 – Examples of temperature and solubility conditions required for transient liquid-phase sintering [13].

Commercial Aluminum PM alloys are most commonly sintered via PLPS for several reasons [14]. Included are (a) the considerably faster processing rates are achieved given the occurrence of beneficial sintering mechanisms such as rearrangement and solution-reprecipitation, (b) the enhanced homogenization of the alloying additions achieved via the superior diffusion rates within the liquid phase, and (c) the improved alteration of the surface oxide layer through the presence of Magnesium and the liquid phase. The main drawbacks of PLPS are the increase in dimensional change and increased risk of warpage. Many authors have achieved PLPS in Aluminum PM alloys through the use of suitable liquid forming additive such as Al_2Cu (θ) master alloys and elemental Sn [15] [16][17][18][19], both of which exhibit the conditions necessary for PLPS, as shown from the following Aluminum-Copper and Aluminum-Tin binary phase diagrams, Figure 19 and 20, respectively. Furthermore, the use of an Al-Cu master alloy avoids complications arising from the relatively high melting point required to melt elemental Copper which typically leads to undesirable TLPS, as well as compressibility issues in forming fully pre-alloyed powders.

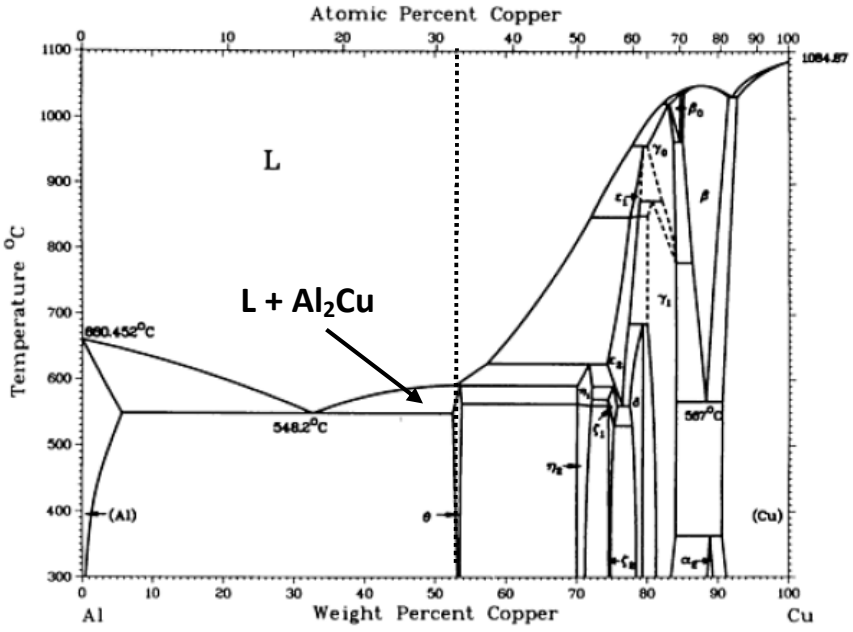

Figure 19 – Aluminum-Copper binary phase diagram indicating the conditions necessary for PLPS using Al_2Cu as a liquid former [20].

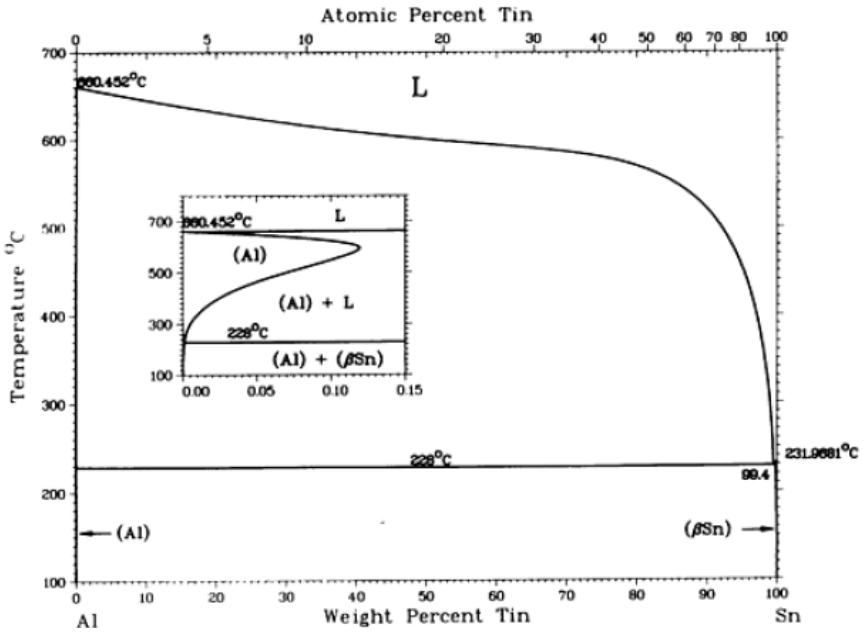

Figure 20 – Aluminum-tin binary phase diagram [21].

Another important aspect in the commercial sintering of Aluminum PM is that the powders are generally atomized through the use of air, leading to surface oxidation (Al_2O_3) of the powder particles. Because sintering is primarily a surface phenomenon and relies on mass transport between adjacent powder particles, the presence of a highly stable insulating oxide film will otherwise inhibit diffusion and neck growth [22][22][24][25][26]. The thermodynamic stability of the oxide layer prevents chemical reduction through conventional techniques such as hydrogen gas reduction. Hence, alternative means of disrupting the film must be implemented. Typically, this is achieved with additions of Magnesium given that it has a greater affinity for oxygen as illustrated in the following chemical reaction:

$$\frac{4}{3}Al_2O_3 + Mg \rightarrow MgAl_2O_4 + \frac{2}{3}Al \qquad \Delta G^{\circ} < 0\ (@\ T_{Sintering}) \qquad \textbf{Equation 3}$$

In addition to this it is also postulated that fracturing of the oxide shell may also occur during compaction when powder particles are heavily deformed. The newly exposed Aluminum metal is then capable of reacting with the alloying elements (i.e. Copper,

Magnesium, Silicon) so as to invoke the formation of a liquid phase as well as their diffusion into the α-Al grains.

1.4.2 Sintering Furnaces and Atmospheres

Sintering furnaces can be categorized as either batch or continuous processes. The former have relatively low capital costs, gas flow rates and production throughput. Comparatively, the latter are generally more costly to purchase and operate yet they permit the attenuation of exceptionally high production rates on a continuous basis. Examples of these common furnace styles are shown in Figure 21. Batch furnaces are generally similar in design, with the exception of their heating elements, and atmosphere control systems. However, continuous furnaces are available in many different configurations such as a pusher style system, ceramic or metallic belt conveyor, roller hearth, and walking beam. A particular system is chosen based on a number of factors including cost, the material of interest, sintering temperature requirements, and permissible contamination limits.

Heating can be achieved using resistive heating elements, fuel combustion, induction, etc. depending on the temperature range and desired sintering atmosphere. Fuel combustion is normally the most inexpensive. However, fluctuations in its chemistry, high moisture and oxygen content, and the reducing behaviour of its combustion by-products (H_2 and carbon monoxide), have typically reserved its use in the sintering of Fe and Cu parts. The atmosphere used during sintering is crucial in the sintering of metallic components, as it provides oxidation protection, as well as intentional reduction in many materials. Inert gasses such as argon are typically used in applications requiring very good protection and when the materials may be too volatile for vacuum sintering. To ensure a final high quality part, high purity gasses are generally used principally for their reproducibility. Table 1 lists a variety of common sintering atmospheres along with information regarding their principal use, cost, and other key attributes.

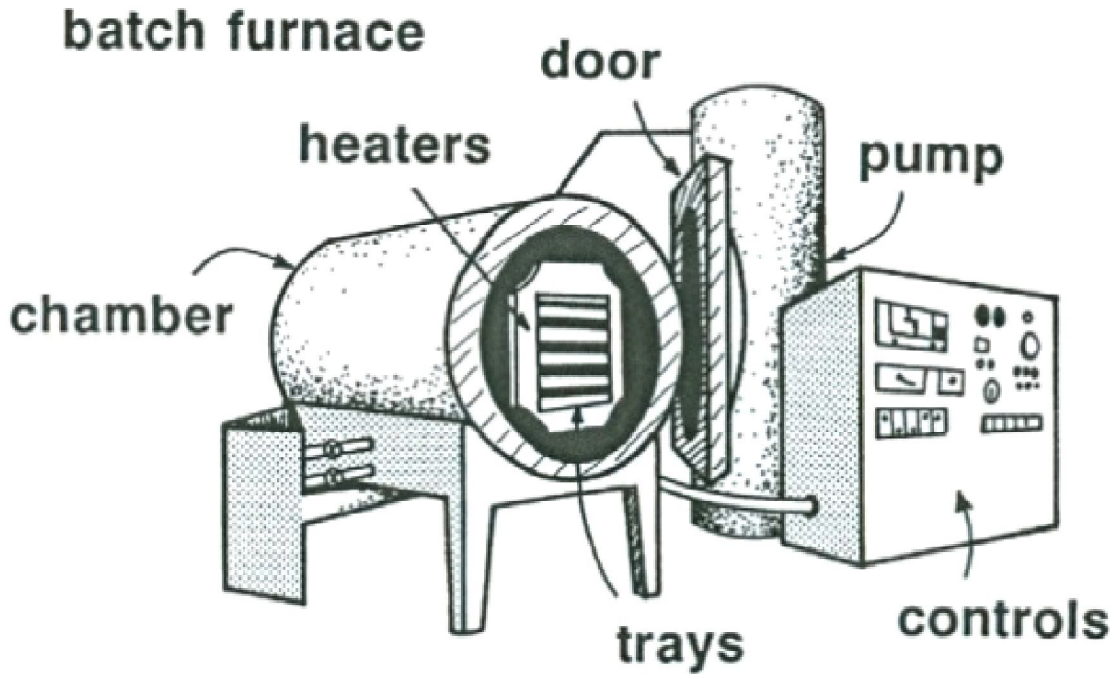

(a)

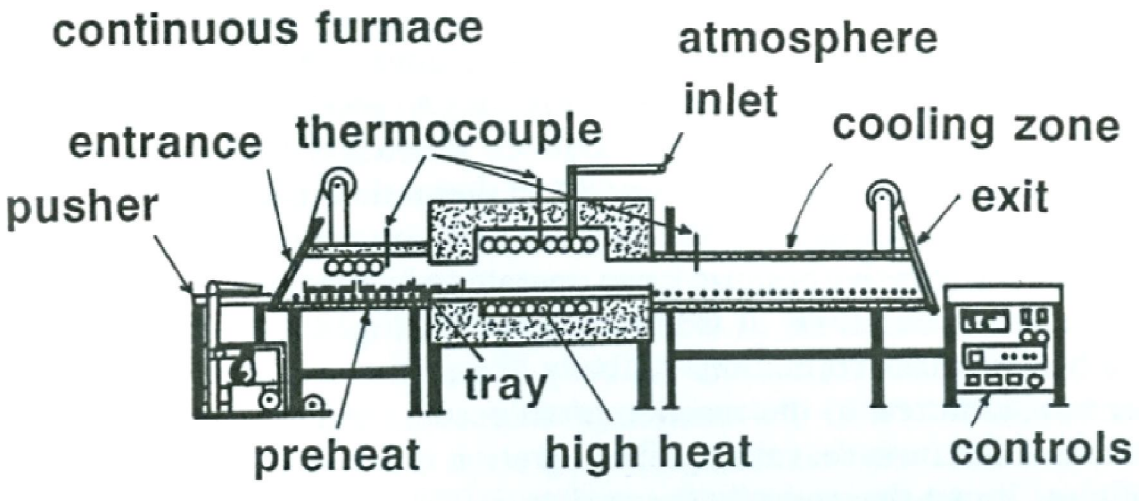

(b)

Figure 21 – Schematic of typical batch (a) and (b) continuous pusher-type sintering furnaces [12].

Table 1 – Various atmospheres commonly used in PM processing of a variety of materials [5].

Atmosphere	Type	Common Applications	Other
Nitrogen	Semi-Inert	Aluminum PM	Safe and relatively inexpensive, possible nitridation
Dissociated Ammonia	Reducing	Ferrous PM, Aluminum PM	Possible hydrogen reduction contamination
Argon	Inert	Mg, Ti, Li alloys	Expensive, high purity
Vacuum	N/A	Ti, Be, Ta alloys	Batch Process, Costly
Hydrogen	Reducing	Ferrous PM	Expensive cost and storage
CO	Reducing	Ferrous PM	-
Air	Oxidizing	Ceramics	Inexpensive
Pure Oxygen	Oxidizing	Oxide Ceramic	Storage

1.4.3 Industrial Sintering of Aluminum PM Alloys

Die casting has maintained its role as the major forming technique for Aluminum alloys primarily because of its high output rates and adequate mechanical properties. However, disadvantages of this technique include heightened erosion of tooling, the presence of macro porosity, and the requirement that Silicon be present in significant concentrations for its ability to improve the fluidity of molten Aluminum alloys. Recently, Aluminum PM has proven to be a competitive, cost effective alternative to die casting in a growing number of applications, and as such, specialized processes have been developed to maximize efficiency while maintaining quality.

In order to maintain low operational costs Aluminum PM alloys are typically sintered in large lots using continuous belt furnaces similar to that shown in Figure 22. Continuous furnaces are open to the atmosphere and as such require a constant flow of nitrogen gas to minimize contamination and oxidation. Nitrogen is the atmosphere gas of choice for press-and sinter Aluminum components primarily due to its relatively low cost, ease of storage, and ability to invoke good sintering characteristics [18].

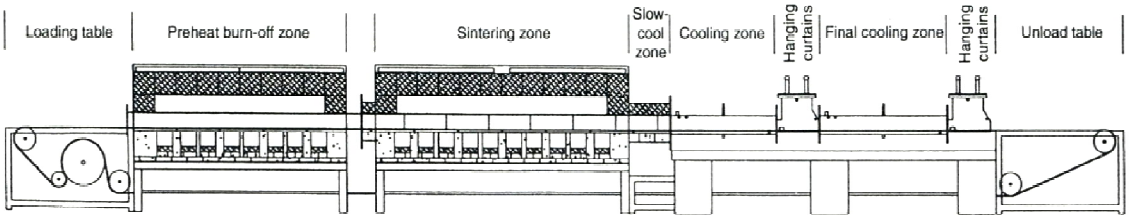

Figure 22 – Schematic of a continuous mesh belt furnace typically used in the sintering of Al PM [27].

The principal sources of contamination in these furnaces are moisture (H_2O) and oxygen requiring continuous monitoring. A parameter known as dew point is commonly monitored to detect the severity of contamination resulting from water vapour. The relationship between the water content and the dew point temperature can be approximated using the following equation [12]:

$$log_{10}(V_{H_2O}) = -0.237 + 3.36 \cdot 10^{-2} T_D - 1.74 \cdot 10^{-4} {T_D}^2 + 5.05 \cdot 10^{-7} {T_D}^3 \quad \textbf{Equation 4}$$

Where:

V_{H2O} = Percent volume of water

T_D = Dew point in ˚C

For example, a dew point of - 60˚C would yield a water v/o of approx. 0.001 v/o H_2O, while 0˚C equates to a content of ~ 0.6 v/o H_2O. Therefore, a lower dew point reduces the likelihood of vapour condensation. Industrial furnaces are usually operated in such a way as to maintain a dew point between -40 and -60˚C. Additionally, the oxygen content of the atmosphere is generally maintained at < 5 ppm by continuously flowing large volumes of high purity nitrogen counter current to the direction of belt travel. The effectiveness of sintering Al alloys in nitrogen as opposed to dissociated ammonia and under vacuum is evident in Table 2, where the mechanical properties of commercial Aluminum PM alloy 201AB are tabulated as a function of sintering atmosphere, green density, and heat treatment. Overall, powders pressed to high green densities and sintered under high purity nitrogen display superior mechanical properties relative to the other

sintering atmospheres. However, at lower green densities sintering under vacuum provides optimal mechanical properties, possibly attributed to reactions occurring between the powder and gasses of the more porous green compacts, or the trapping of N_2 gas inside the pores, inhibiting further densification.

Table 2 – Effect of sintering atmosphere and green density on the tensile properties of Alcoa 201AB Aluminum PM Alloy in the T1 and T6 tempers [27].

Sintering Atmosphere	Green Density (%)	Temper	Tensile Strength (MPa)	Yield Strength (MPa)*	Elongation (%)
Nitrogen	2.50 g/cc (90 %)	T1	167	147	3.0
		T6	265	262	1.5
	2.64 g/cc (95 %)	T1	209	177	3.0
		T6	336	322	2.0
Dissociated NH_3	2.50 g/cc (90 %)	T1	161	141	2.0
		T6	247	-	0.5
	2.64 g/cc (95 %)	T1	174	152	2.0
		T6	288	287	1.0
Vacuum	2.50 g/cc (90 %)	T1	185	143	4.0
		T6	296	287	2.0
	2.64 g/cc (95 %)	T1	184	146	4.0
		T6	312	290	2.0

*Stress at 0.2% Offset

Since die compaction is the most extensively used forming technique in Aluminum PM, sintering cycles must include a delubrication stage in order to avoid undesirable reactions between the lubricant and the powder during sintering. The dynamic nitrogen atmosphere and low dew point cause lubricants to undergo pyrolysis during the initial heating, which is essentially exhausted once the powder compacts reaches a temperature of between 400 and 450°C and before being heated again to the sintering temperature [7].

Modern continuous mesh belt furnaces also include a series of thermocouple controlled zones. These facilitate the attenuation of appropriate thermal conditions for delubrication, sintering and cooling, and allow precise control of heating and cooling rates. Figure 23 demonstrates the appearance of a temperature-time profile recorded

during a typical sintering cycle of a part as it progresses through the furnace. Despite the step like temperature gradients observed in the furnace temperature, the heat transfer between furnace and the parts displays a much more gradual increase to the true part temperature. This is unavoidable, and as such operational parameters such as belt speeds and zone temperature must be modified to attain the desired properties in the finished component.

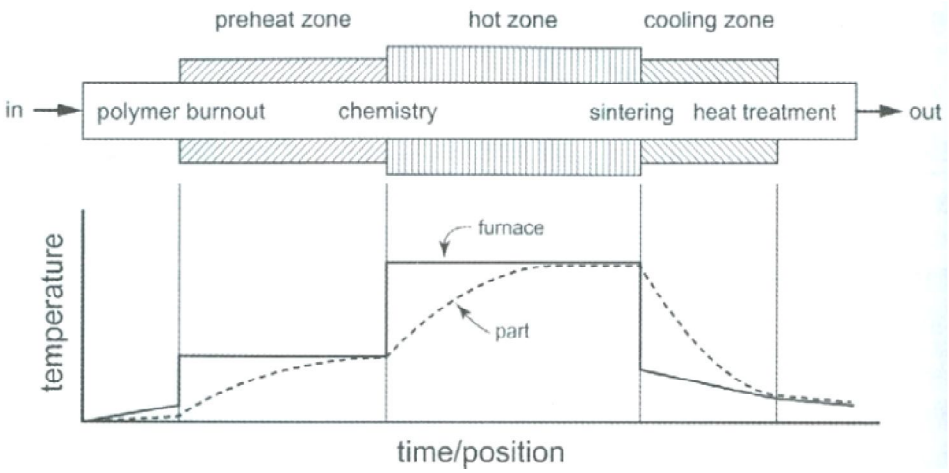

Figure 23 – Typical temperature versus time/position profile observed during delubrication and sintering of Aluminum PM alloys [5].

1.5 Secondary Operations in Aluminum PM

In the as-sintered condition most PM components require minor additional processing to attain adequate dimensional accuracy, mechanical properties, and aesthetics. Common forms of secondary processing in Aluminum PM include but are not limited to:

- Sizing
- Deburring
- Heat-treatment
- Machining

Even in alloys carefully engineered to minimize dimensional change resulting from sintering, a secondary sizing step is generally necessary to hone dimensions while providing slight improvements in mechanical properties. This step requires that as-

sintered components be in a deformable state. Hence, sizing is generally performed immediately after sintering and prior to heat treatment. Sizing is performed using large presses and tooling similar to that used during powder compaction. Deburring is typically performed to remove any small burrs that may have formed during compaction and improve the appearance of the components via polishing. This process is generally performed in a large drum with hard polishing media such as Al_2O_3. Frequently, this is completed in the presence of a mildly acid solution to enable dissolution and mechanical abrasion in a single cycle. Finally, in many circumstances machining is inevitable, even in near-net shape PM processing. For example, this can arise when exceptionally tight dimensional tolerances are warranted or when features are needed in a part that cannot be achieved through die compaction.

1.6 Commercial Al-Cu-Mg Powder Metallurgy Alloys

The adoption of PM in the manufacture of automotive components has lead to the development of several commercial "press-and-sinter" Aluminum powder blends as listed in Table 3. In addition to the Alcoa 201AB powder, which is no longer in production, most current commercial powder blends are based upon the Al-Cu-Mg-Si system of composition equivalent to wrought A2014. It is worthy to note that both Alumix® 123 and the Alcoa 201AB contain greater concentrations of Si than of Mg, and as such would be classified as Al-Cu-Si alloys. However, commercial PM alloys containing Al, Cu, and Mg as their major alloying additions are currently very uncommon, and those based on the composition of AC2014 have become the staple of commercial 2xxx series PM alloys.

Table 3 – Nominal compositions of several commercial Al-Cu-Mg PM Aluminum Alloys [27][28][29][30].

Commercial Alloy	Manufacturer	Nominal Composition (wt%)*			
		Al	Cu	Mg	Si
Alumix® 13	Ecka Granules	Balance	4.2 - 4.8	0.4 - 0.6	0.05 - 0.25
Alumix® 123	Ecka Granules	Balance	4.2 - 4.8	0.4 - 0.6	0.50 - 0.70
A2712	Ampal	Balance	3.8	1.0	0.8
201AB	Alcoa	Balance	4.4	0.5	0.8

*1.5 wt% admixed lubricant present in all powder blends.

The typical mechanical properties of these alloys are listed in Table 4, along with their specific PM processing conditions. These alloys display good strength and ductility for PM alloys despite the presence of considerable amounts of residual porosity as is evident from their as-sintered densities. Each of the alloys also clearly exhibits a good response to age hardening coincident with a typical decrease in ductility.

Table 4 – Mechanical properties for several commercial Al PM alloys when processed through various heat treatments [27][28][29][30].

Commercial PM Alloy	Pressure (MPa)	Density (%)*	Temper	Tensile Strength (MPa)	Hardness (HB)	Elongation
Alumix® 13	220	2.50 g/cc (89.5 %)	T1	160	55	4.0 %
			T4	210	90	3.0 %
			T6	240	90	2.0 %
Alumix® 123	250	2.52 g/cc (90.8 %)	T1	190	60	5.0 %
			T4	260	75	3.0 %
			T6	320	100	1.0 %
A2712	200	2.56 g/cc (93.0 %)	T1	180	50	2.0 %
			T4	-	-	-
			T6	-	-	-
201AB	180	2.58 g/cc (93.1 %)	T1	201	65	3.0 %
			T4	245	70	3.5 %
			T6	323	84	0.5 %

*** Percent theoretical as-sintered density.**

1.7 Al-Cu-Mg Powder Metallurgy Alloy PM2324

Due to the limited number of commercially available PM Aluminum alloys, research personnel at Dalhousie university and GKN Sinter Metals investigated the development of carefully engineered Al-Cu-Mg powder blends based on their processing and performance properties. Work done by Boland et al. [31][32] on the development of novel Al-Cu-Mg alloys for press-and-sinter powder metallurgy processing, lead to the creation of a new Aluminum PM alloy designated PM2324. After careful evaluation of numerous combinations of powder sources, alloy compositions, compaction pressures, and sintering parameters, the authors identified the optimal composition shown in Table 5 for its outstanding mechanical properties in comparison to current commercial AC2014. With minor exceptions, this composition is largely equivalent to wrought A2024; one of

the highest strength 2xxx series wrought Aluminum alloys. PM2324 also contained 0.2 wt% elemental tin, as it was shown to provide considerable improvements in sintering response as well as mechanical properties. As previously mentioned several other authors have also reported appreciable gains in terms of densification during sintering of Aluminum-Copper-Magnesium PM blends modified with minor concentrations of tin. This has been attributed to its ideal persistent liquid phase sintering characteristics which can lead to extensive densification.

Table 5 – Composition of AC2014 and PM2324 Al PM alloys and wrought A2024 [32][33].

Alloy	Nominal Composition (wt%)				
	Al	Cu	Mg	Si	Other
A2024	Balance	4.4	1.5	-	0.6 Mn
AC2014	Balance	4.5	0.5	0.6	-
PM2324	Balance	4.4	1.5	-	0.2 Sn

Aside from a minor decrease in ductility, the mechanical properties of PM2324 were shown to be far superior to current AC2014 PM alloys, as shown in Table 6. Gains of almost 100% where achieved in both the yield and tensile strength of PM2324 versus AC2014.

Table 6 – Mechanical properties of the Aluminum PM alloys PM2324 and AC2014 [31].

Alloy	Temper	Tensile Strength (MPa)	Yield Strength (MPa)*	Elongation (%)	Hardness (HRE)
AC2014	T1	152	117	3.0	60
PM2324	T1	296	245	1.9	99

***Stress at 0.2 % offset**

Figure 24 compares the microstructures of AC2014 and PM2324 where it is clear that the considerable gains in mechanical properties of PM2324 are most likely attributed to its high as-sintered density and refined distribution of alloying elements within the α-Al grains.

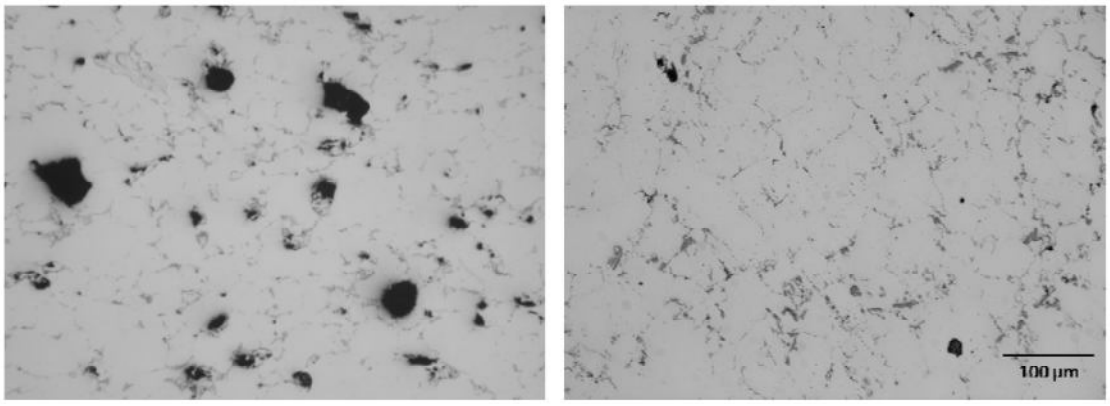

Figure 24 – Optical micrographs comparing the as-sintered (T1) microstructures of AC2014 and PM2324. Both images represent unetched microstructure, taken at the same magnification [31].

The promise of PM2324 as a high strength press-and sinter PM alloy has led to further studies. For example, the forgeability of PM2324 and its response to hot deformation when alloyed with 5 wt% SiC, were examined in work done by Mann et al. [4]. This research showed that after adequate post-sinter hot deformation via swaging, PM2324 had achieved full density (> 99.9% Theoretical) and with the exception of ductility, exhibited mechanical properties slightly superior to its wrought counterpart A2024-T6.

Chapter 2 Strengthening Mechanisms in Aluminum Alloys

In practice, the strength of most Aluminum alloys is largely attributed to a series of fundamental mechanisms. The most basic of which is solid-solution strengthening which arises from the presence of solute atoms of differing atomic radii, electro negativity and valence than that of the base material (solvent). The resultant strain fields are created from the distortion of the lattice and act to inhibit dislocation motion. The solid solutions formed in Aluminum alloys are generally those of a substitutional type wherein an atom of Aluminum is directly replaced with one of the solute species (Cu, Mg, etc.) as illustrated in Figure 25. The nature of the ensuing lattice strain fields will be different depending on the size of the dissolved species. However, these obstacles are coherent with the matrix and will be preferentially sheared by dislocations.

Figure 25 – Substitution solid solutions for small and large solute atoms [34].

Grain size strengthening and strain hardening are two other strengthening mechanisms typically observed in Aluminum alloys. The former achieves greater strengths through refinement of the mean grain size yielding a greater density of grain boundaries which effectively impede dislocation motion. The increase in yield strength is most easily observed using the Hall-Petch relationship displayed in equation 5, where the strength, σ_o is inversely proportional to the square root of grain size, D [35]. The latter derives its strength from an applied stress that promotes plastic deformation and in turn, increases

the dislocation density so as to enable and enhance dislocation pile up. This mechanism can be understood by observing the stress-strain behaviour of a material after loading within the plastic deformation regime as shown in Figure 26. Upon reloading, a material will continue deformation at the maximum stress and strain achieved during initial loading, thereby increasing the effective yield strength of the material. Both techniques are instilled upon a material as a result of processing variables, i.e. rapid solidification and cold working, respectively. Such strengthening mechanisms are however, susceptible to the effects of annealing at moderate temperatures and are therefore not suitable for applications requiring elevated temperature mechanical strength stability.

$$\boldsymbol{\sigma_o = \sigma_i + k' D^{-1/2}} \qquad \textbf{Equation 5}$$

Where:

σ_o = Yield Stress
σ_i = Frictional stress opposing motion of dislocation
k' = Constant
D = Grain diameter

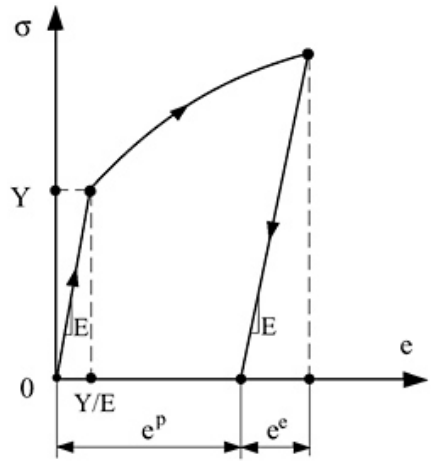

Figure 26 – Hypothetical Stress-strain curve illustrating work hardening [35].

Although all previously mentioned strengthening techniques are observed in singular phase alloy systems, the vast majority of commercial Aluminum alloys contain alloying

additions which form secondary phases upon solidification. The controlled formation of a secondary phase throughout the base material yields considerable strengthening as such phases serve as obstacles and thereby impede the motion of dislocations within the alloy. Such strengthening techniques are typically categorized as either precipitate hardening or dispersoid strengthening; the main differences being the relative size of the secondary phase, their spatial distributions, and thermal stability.

Considering precipitation hardening, many Aluminum alloy systems exhibit a significant amount of solubility for certain alloying additions. This is often higher at elevated temperatures and falls to a negligible amount at ambient. Such behaviour is ideal for precipitation strengthening as it allows one to form the requisite super-saturated solid solution at ambient that can then be decomposed in a controlled manner via a secondary stage of age hardening. During decomposition, strong, intermetallic phases are precipitated within the grains of the alloy. This can proceed very slowly at room temperature, in which case it is termed natural aging. A more practical alternative to this is controlled aging at a moderate temperature (100-200ºC), also known as artificial aging. Depending on the aging temperature employed, the net result is the formation of a highly refined distribution of an extremely small secondary phase(s), which is initially coherent/semi-coherent with the α-Al matrix and progressively more incoherent with increasing aging times and temperatures. This type of strengthening provides considerable increase in strength in comparison to other strengthening mechanisms. Indeed, precipitation strengthening is used in many Aluminum alloys. For example; the Al-Cu, Al-Mg, Al-Zn, Al-Be, Al-Li, and Al-Mg-Si systems all exhibit precipitation hardening [36]. However, similar to strain hardening and grain size strengthening, such properties are susceptible to degradation when exposed to elevated temperatures for prolonged periods of time. Here, the loss of strength results from the coalescence and coarsening of the precipitates themselves.

Dispersoid strengthening is commonly observed in Aluminum alloys alloyed with elements possessing negligible solubility in α-Al, i.e. Si, Fe, Mn, etc.. During their melting/casting the dispersoid strengthening constituents dissolve into the liquid melt

forming a homogenous mixture. However, upon solidification they quickly segregate forming a dispersion of elemental crystals or intermetallic aluminide phases throughout the α-Al grains and along grain boundaries, as illustrated in Figure 27. Such behaviour is commonly observed in Aluminum alloys intentionally alloyed with minor amounts of insoluble transition metals (Mn, Cr, Fe, etc.) as well as trace impurities such as Iron and Silicon; elements typically found in commercial grade Aluminum metal [33]. Theoretically, at very small particle radii, dispersion strengthening should yield very high levels of strengthening as a result of the inability of dislocations to cut through the incoherent secondary phases. In reality however, it is extremely difficult to obtain such an effective dispersion similar to that achieved in precipitation hardenable alloys. Such a microstructure typically warrants the use of PM processing, since the typical solidification rates achieved in conventional IM are too slow to prevent the bulk of the insoluble secondary phases from segregating to grain boundary regions, in addition to reducing the likelihood of undesirable particle coarsening.

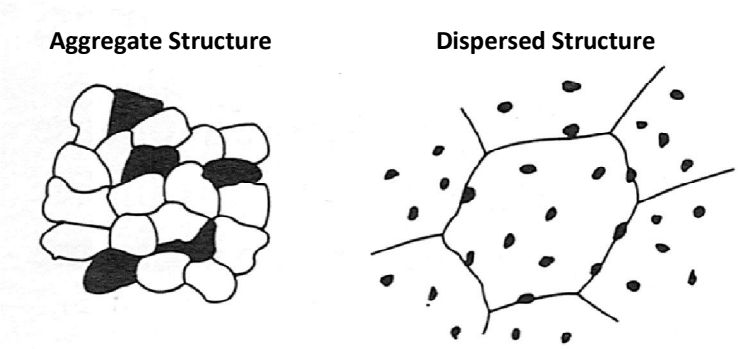

Figure 27 – Types of two phase microstructures [35].

Wrought Aluminum alloys whose primary alloying addition is Copper are classified as the 2xxx series. These alloys exhibit high strength and formability rendering them suitable for automotive and aerospace applications wherein weight reduction is of considerable importance. Copper has a maximum solid solubility of ~ 5.65 wt% in α-Al, which rapidly decreases with decreasing temperature enabling precipitation strengthening through the controlled distribution of the Al_2Cu phase. The precipitation sequence of Aluminum-Copper alloys is as follows:

$$SSSS \rightarrow GP\ Zones \rightarrow \theta''(Al_2Cu) \rightarrow \theta'(Al_2Cu) \rightarrow \theta(Al_2Cu) \qquad \textbf{Equation 6}$$

In practice, the precipitation sequence begins with the formation of a supersaturated solid solution (SSSS) through the complete dissolution of Copper at a temperature below the eutectic melting point (548˚C). The alloy is then rapidly quenched to ambient where the maximum solubility of Cu in Al is < 0.1 wt%. This creates a highly strained, metastable microstructure as a result of super saturation of Cu in α-Al. With sufficient natural aging or artificial aging the ensuing instability forces the homogenous precipitation of Al_2Cu-type phases within the α-Al grains. Initially, this creates a Copper rich phase known as Guinier Preston zones (GPZs). These zones appear as disks a few Copper atoms thick. As a result of an atomic radii mismatch of approx. 11 %, they are strained tetragonally but remain coherent with the atomic lattice and parallel to the $\{100\}_{Al}$ matrix planes [33]. As aging proceeds, the Copper concentration of the GPZs increases as does the thickness and diameter of the phase. The precipitate retains its tetragonal structure but begins to lose coherency. At this point it is now semi-coherent and has evolved into the θ" phase. The greatest volume fraction of θ" possible is typically sought as this phase generally coincides with optimum strengthening. Eventually, heterogeneous nucleation of the θ' phase occurs along defects simultaneously with the formation GPZs and θ" (GPZ 2). This is often associated with a gradual decrease in strength attributed to the complete incoherency of the θ' phase. Lacking coherency, this particular phase does not provide strengthening through coherency-based strains but rather through the interfacial energy created between it and the α-Al matrix. Therefore, the presence of a significant volume fraction of θ' generally indicates overaging and is viewed as undesirable. After extensive artificial aging, the fully incoherent equilibrium intermetallic θ is formed. This phase has an exact stoichiometry of Al_2Cu and forms from the direct transformation of θ'. Figure 28 demonstrates the effects of aging time and the corresponding phases associated with each strengthening condition, achieved during aging of several binary Aluminum-Copper alloys.

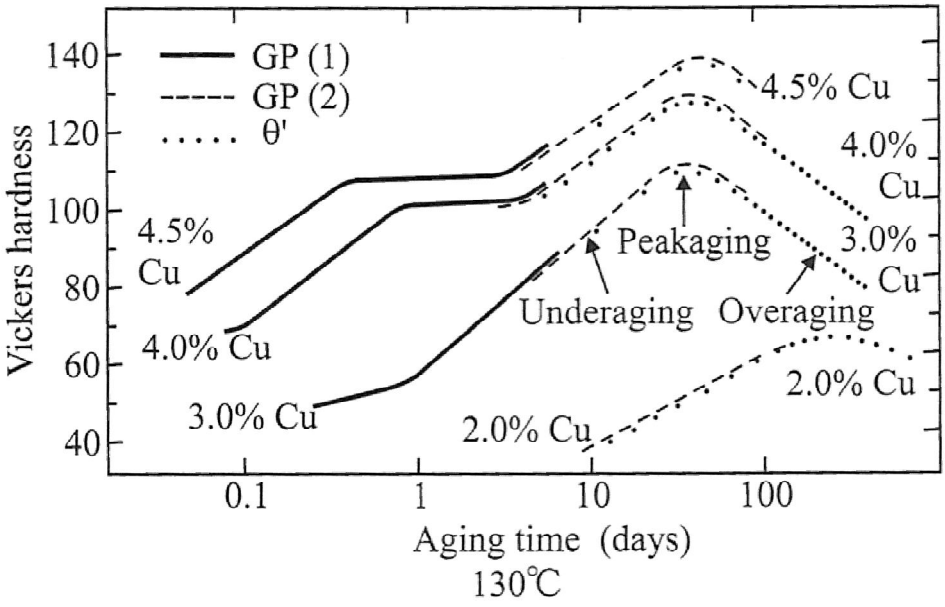

Figure 28 – Example of age hardening curves for Aluminum-Copper alloys [36].

The θ-based precipitation sequence described above can be altered appreciably in the presence of a sufficient quantity of Mg. Here, this element can prompt the formation of the S phase according to the following precipitation sequence:

$$SSSS \rightarrow GPB\ Zones \rightarrow S''(Al_2CuMg) \rightarrow S'(Al_2CuMg) \rightarrow S(Al_2CuMg) \quad \textbf{Equation 7}$$

Although this is a commonly accepted sequence, there exist some ambiguity concerning the structure of each S phase modification [37][38]. In Aluminum-Copper-Magnesium ternary systems θ and/or S precipitation sequences can be active depending on the Cu:Mg ratio. Above a Cu:Mg of ~ 2, the decomposition sequence from solid solution begins with the segregation and clustering of Copper and Magnesium atoms forming Guiner-Preston-Bagaryatsky zones (GPBZ) on the $\{100\}_{Al}$ and $\{210\}_{Al}$ [39]. These Cu and Mg rich regions subsequently transform to S″ which possesses an orthorhombic crystal structure while remaining coherent with the FCC Aluminum matrix [40]. This is followed by decomposition to semi-coherent S′ and incoherent, but stable S. This aging sequence occurs continuously as the precipitates grow and rotate with increasing lattice mismatch strains until they reach their most stable arrangement as coarse incoherent S phase

precipitates. Similar to θ″ and θ' in Aluminum-Copper alloys, a considerable concentration of S″ and S' are generally coincident with peak age hardening in Al-Cu-Mg type alloys. These precipitates are present as platelets aligned with the $<100>_{Al}$ matrix direction on the $(100)_{Al}$ and $(210)_{Al}$ planes. S type phases preferentially precipitate on dislocations, therefore the aging behaviour of such alloys are commonly enhanced through the addition of cold work prior to artificial aging [41]. Figure 29 displays a TEM image of an Al-Cu-Mg precipitation hardenable alloy after solutionizing and subsequent aging; revealing the shape and fine size of S phase precipitates in α-Al.

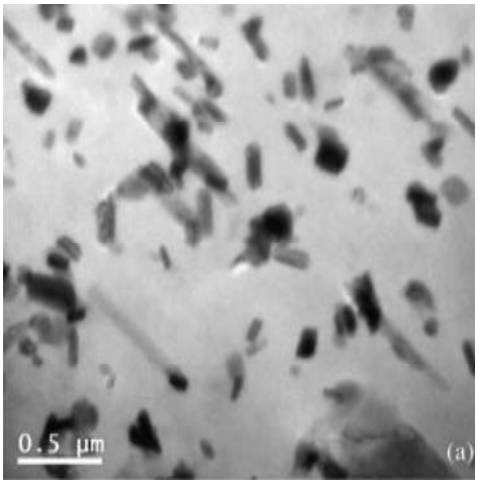

Figure 29 – TEM image of S (Al2CuMg) precipitates in a wrought A2324-T6 Al-Cu-Mg alloy [42].

Unfortunately, the precipitation strengthening mechanisms described above can degrade in the presence of prolonged thermal exposure. This causes the precipitates to coarsen and become increasingly less coherent; in effect, over aging the alloy in-situ. Therefore, when designing Aluminum alloys for elevated temperature service one must consider other strengthening mechanisms such as solid solution strengthening and/or the formation of secondary dispersoid phases as they provide far more stable mechanical gains. Most transition metals exhibit a negligible solubility in α-Al at all temperatures and tend to form a stable dispersion of incoherent aluminide species throughout the microstructure.

These secondary phases inhibit crack propagation and improve tensile strength generally at the expense of ductility. They generally possess far greater melting points than α-Al and tend to inhibit grain growth and recrystalization by pining the α-Al grains. In this sense, they are typically viewed as additions that are beneficial to elevated temperature strength. Of the transition metals, Iron, nickel, manganese, chromium, titanium, zirconium, and vanadium have been successfully used to improve elevated temperature properties. For example, AA2024, a high strength wrought Al-Cu-Mg-Mn alloy has been reported to exhibit observable improvements in elevated temperature stability resulting from the formation of dispersoids such as $Al_{12}(Mn,Fe)_3$ [43].

Accordingly, certain 2xxx series alloys have been developed with controlled additions of dispersoid forming transition metals. Table 7 lists the composition of two commercial wrought alloys specifically designed for elevated temperature service. Both A2218 and A2618 contain Fe and Ni, two relatively slow diffusing, high melting point alloying species which exhibit a negligible solubility in α-Al; key attributes that enable the formation of secondary intermetallic phases with superior elevated temperature stability. Several authors [43][44][45] believe that the Al_9FeNi phase is primarily responsible for the most significant contribution to dispersoid strengthening. However, Al_7Cu_2Fe and Al_7Cu_4Ni have also been identified as contributing species although their Copper content has been attributed to an undesirable reduction of Cu in the α-Al matrix. Figure 30 illustrates the size and distribution of the dispersoids strengthening phase present in heat treated A2618-T6 Al-Cu-Mg-Fe-Ni alloys. It has also been postulated that during solidification of A2618 type alloys, preferential formation of Al_9FeNi proceeds through the following binary equilibrium eutectic reaction; $L \rightarrow \alpha\text{-Al} + Al_9FeNi$, which occurs within the temperature range of 645ºC to 515ºC [46]. It is also believed that formation of primary Al_9FeNi dispersoids is unlikely throughout the entire compositional range of the alloy, and according to the ternary Al-Cu-Mg phase equilibrium, increasing Copper concentrations are expected to lower the solidus temperature to ~ 505ºC while proceeding with the quasi-ternary eutectic reaction; $L \rightarrow \alpha\text{-Al} + Al_9FeNi + Al_2CuMg$ (non-equilibrium).

Table 7 – Wrought 2XXX Aluminum alloys commonly employed for elevated temperature service [33].

Wrought Alloy	Nominal Composition (wt%)						
	Al	Cu	Mg	Si	Fe	Ni	Other
A2218	Bal.	3.5-4.5	1.2-1.8	0.9	1.0	1.7-2.3	-
A2618	Bal.	1.9-2.7	1.3-1.8	0.1-0.25	0.9-1.3	0.9-1.2	0.04-0.1 Ti

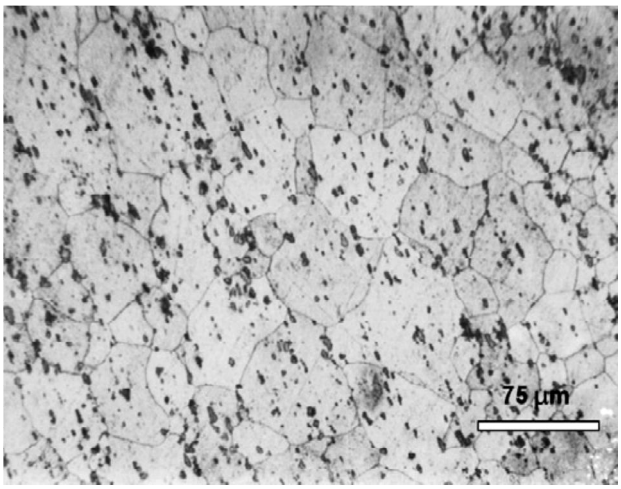

Figure 30 – Optical micrograph revealing Al-Fe-Ni dispersoids (dark) in extruded and thermally aged A2618 Aluminum alloy [44].

The benefits of such alloys are perhaps best illustrated by considering the rate at which engineering-critical properties such as yield degrade as a result of thermal exposure (Figure 31). Compared to a high strength alloy such as A7075 that does not include transition metal additions, it is evident that an alloy such as A2618 exhibits a much more gradual decline in strength as the time and temperature of exposure are increased. Work done by W. Feng et al. [47] on the microstructural characterization of A2618 via x-ray diffraction, determined that the phases containing Fe and Ni remained in microstructure even when treated to a 520˚C homogenization treatment for 16 hours. Conversely, the S phase precipitate was fully dissolved into the matrix thereby completely negating any strengthening effect from it.

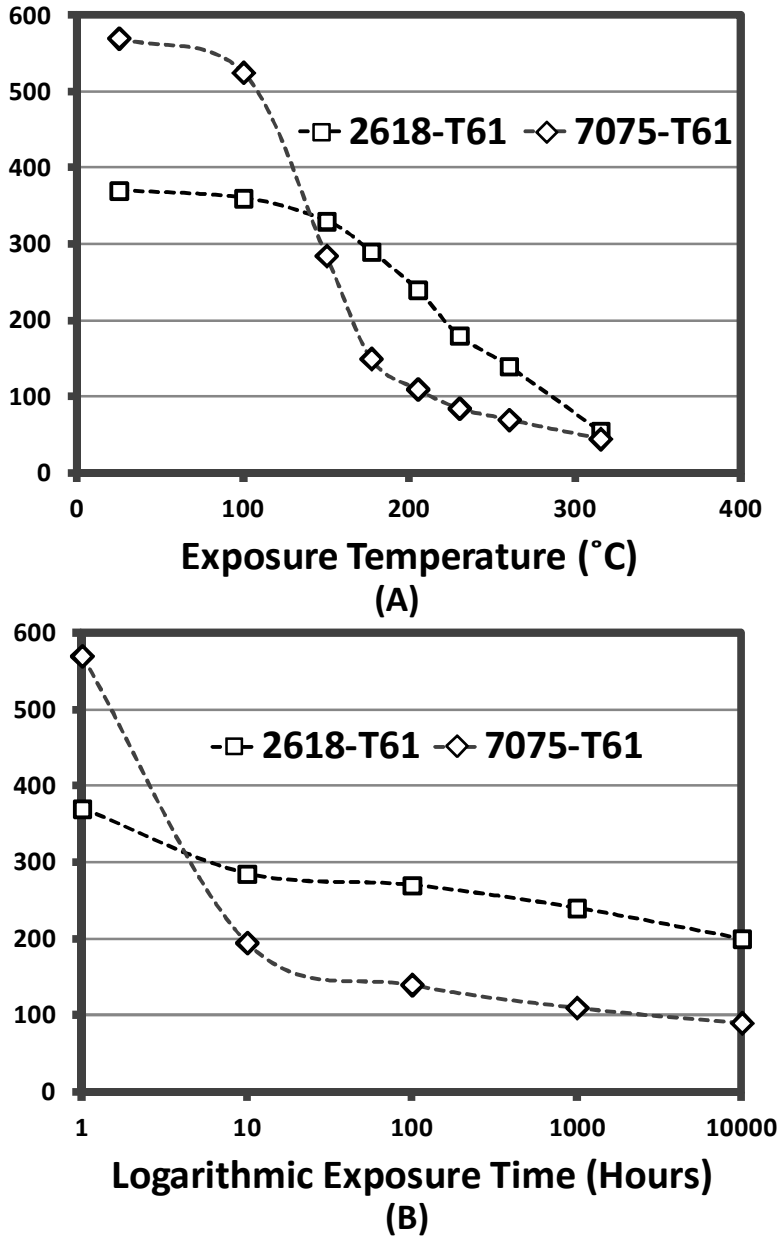

Figure 31 – Effects of the (A) temperature and (B) time of thermal exposure on the yield strength of wrought A2618-T6 and 7075-T6. Samples in (a) were exposed for a constant time of 1000h. Those in (b) were exposed at 205˚C. All tensile specimens were tested at room temperature [48].

Aside from wrought processing, Aluminum PM is also known to be a highly suitable processing technique in the development of elevated temperature Aluminum alloys. Typically, this occurs as a result of finely dispersed intermetallic phases formed in the raw powder during atomization. Similarly, oxides, carbides and other highly stable compounds can also be entrained in the powder when techniques such as mechanical alloying are employed. Early sintered Aluminum alloys were intentionally created with a considerable fraction of Al_2O_3 in order to obtain an oxide dispersion strengthening phase which, unlike precipitates, was stable. This allowed the alloy to maintain strength at elevated temperature while providing enhanced creep resistance. More recently, Aluminum powders have been pre-alloyed with stable intermetallic forming additives (Mn, Cr, Fe, Ni, etc.) in an effort to form beneficial phases such as Al_9FeNi. Although no elevated temperature Aluminum PM alloys are currently utilized in high volume scenarios, several have been developed for this purpose (Table 8). The contribution of precipitation hardening and solid solution strengthening in these alloys is generally absent as most of the alloying additions are deliberately chosen because of their negligible solubility in Aluminum as this assists with the formation of a stable distribution of dispersoids. In particular, Iron, Cerium, Vanadium and Zirconium have received a considerable amount of interest.

Table 8 – Various experimental Aluminum powder metallurgy alloys designed for elevated temperature service [49][50][51][52][53][54].

Manufacturer	Designation	Al	Cr	Zr	Si	Fe	Mo	Ce	V
Alcan	-	Bal.	5.0	2.0	-	-	-	-	-
Alcoa	CZ42	Bal.	-	-	-	7.0	-	6.0	-
Allied - Signal	FVS-1212	Bal.	-	-	2.4	11.7	-	-	1.2
Pratt & Whitney	-	Bal.	-	-	-	8.0	2.0	-	-

Although these PM alloys exhibit exceptional elevated temperature stability they are saddled with certain drawbacks. For instance, the presence of a large fraction of heavy transition metals acts to increase their density. In automotive and aerospace applications this is particularly problematic as the primary purpose for adopting Aluminum alloys is their low density. Beyond this, the associated costs of the expensive alloying elements and the need for advanced processing equipment have also impeded widespread use.

Figure 32 represents the temperature limitations of current IM and PM Aluminum alloys and the effectiveness of dispersion strengthening at elevated temperatures. Also evident from this figure is the absence of Copper as well as the considerable utilization of insoluble dispersoid forming transition metals (Ni, Fe, V) and mechanically alloyed carbide/oxides at higher temperatures.

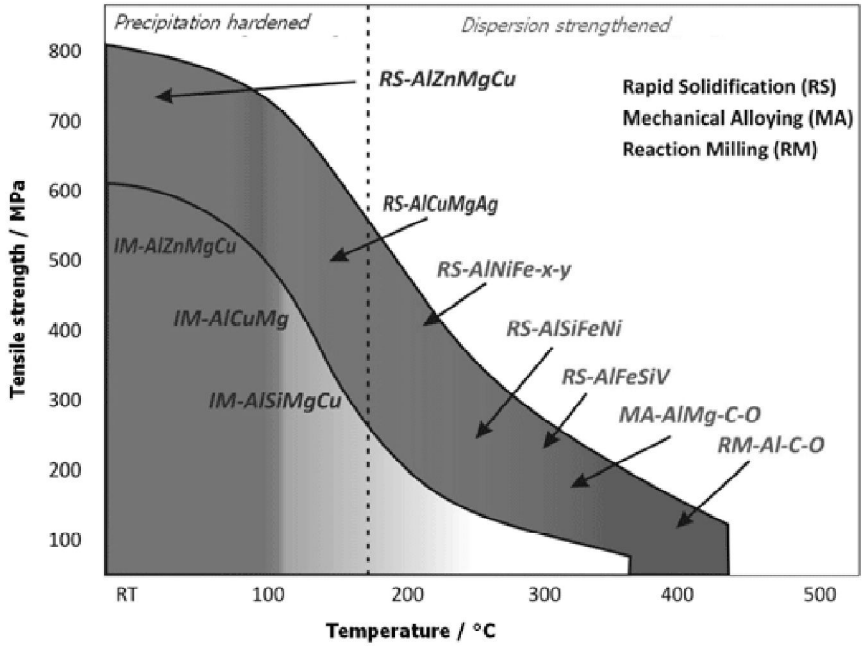

Figure 32 – Tensile strength versus temperature of Aluminum alloys produced via ingot metallurgy (IM), rapid solidification (RS), mechanical alloying (MA) and reaction milling (RM) [55].

Other areas of research have focussed on the effects of Fe and Ni additions to 2xxx series Aluminum PM alloys in the interest of improving elevated temperature stability. The effects of varying Ni and Cu concentrations on the sintering response and elevated temperature mechanical properties of an Al-1Mg PM alloy were examined by Dunnett et al. [56]. The authors noted that significant improvements in thermal stability could be achieved over AC2014 with a composition of Al-15Ni-5Cu-1Mg. Work was done by Xiang [57] and Duan [58] on alloying AC2024 Aluminum alloys with Fe and Ni. Here, the exotic processing techniques of hot extrusion and liquid dynamic compaction

accompanied by hot rolling were utilized. Both approaches resulted in successful incorporation of relatively high concentrations (> 2 wt %) of Fe and Ni yet neither author investigated the actual mechanical performance of their experimental alloys under or after elevated temperature exposure. Despite this, the former managed to preserve the age hardenability of A2024 by incorporating 2 wt% Ni along with 3 wt% Fe. This particular ratio promoted the formation of Al_9FeNi rather than Al_7Cu_2Fe and Al_7Cu_4Ni which helped to minimize Cu depletion in the Aluminum grains. More recently, work conducted by Cooke et al. [59] on evaluating the feasibility of incorporating Fe and Ni to a low Cu:Mg Al-Cu-Mg alloy as a means of improving high temperature stability, revealed that pre-alloying the base Al powder with Fe either Ni (as opposed to via elemental additions) yielded considerable strengthening; and with negligible effects on the overall sintering response. Although the behavior of the alloys after elevated temperature exposure was not examined in this work; the author did achieved high sintered densities and performance through implementation of conventional press-and-sinter processing.

Chapter 3 Research Objectives

Aluminum powder metallurgy alloys have seen increased utilization in the manufacture of automotive engine components. In an attempt to catalyze this growth, many researchers have focussed their efforts on the development of new alloys with properties superior to those of conventional AC2014. One such development is an Aluminum PM alloy that possesses a composition similar to that of wrought A2024 [31][32]. This particular alloy, known as PM2324, has shown great potential for commercial use given its excellent response to PM processing and the high strength measured in the sintered product. Despite such promise, a potential issue concerning the implementation of this (and any) new Aluminum alloy is the possibility of thermal degradation.

In an attempt to address this concern, the incorporation of high melting point transition metal additions is the subject of this study. Fe and Ni were chosen for this purpose in light of their known beneficial effects in wrought alloys as well as their relatively low cost. Such elements will be sourced as elemental and pre-alloyed additions. Their ensuing effects on PM processing response will be examined in laboratory and industrial settings, prior to the completion of trials designed to evaluate their effectiveness at mitigating thermal degradation.

Chapter 4 Experimental Procedures

An array of experimental procedures was employed in this research. These were largely centered in the areas of powder characterization, PM processing, and metallurgical assessment of the finished products. Details on the specific techniques employed are given in the sections below.

4.1 Powder Characterization

The morphology and size distribution of the powders utilized were characterized through scanning electron microscopy (SEM) and laser particle size analysis, respectively. SEM analysis of raw powders required coating of pin stub mounts with a light layer of carbon paste quickly followed by a gentle sprinkling of the powder of interest onto the surface. The paste was then cured for 24h and any loose powder blown off prior to examination. Images were then acquired under an acceleration voltage of 10-20 kV and a beam current of 15 μA. Laser particle size analysis required the preparation of a powder/water slurry using an agitator and ultrasonic bath that was pumped through the analyser operating with beam and focal lengths of 2.0 and 100-300 mm, respectively

A Carney flow meter was used to measure the flow rate of the loose powder blends in accordance with ASTM standard B964 [60]. The Carney flow meter consisted of a metallic funnel into which 25 g of the powder of interest was loaded while the bottom orifice was kept closed. The orifice was then opened and the time required to evacuate all of the powder was measured. The initial mass of powder was then simply divided by the total time of flow so as to yield a flow rate in expressed in grams/second (g/s).

Apparent density (AD) measurements were made using an Arnold meter in accordance with ASTM standard B703 [61].The Arnold meter consists of a smooth metallic plate containing a cylindrical cavity with a machined volume (V) of ~19.8 cm^3. A hollow brass cylinder with a diameter larger than that of the cavity rests on the surface of the plate and is filled with the powder under investigation. Measurements are made by simultaneously gliding and rotating the brass cylinder across the cavity so as to simulate the filling of a die with a feed shoe. The mass of powder retained in the cavity (M) is

then measured. Knowing M and V, the apparent density (ρ_A) can be easily calculated using Equation 8.

$$\boldsymbol{\rho_A = \frac{M}{V} = \frac{M}{19.784\ cm^3}} \qquad \textbf{Equation 8}$$

4.2 Powder Metallurgy Processing

Initially, all powder blends were processed in the laboratory to assess which alloy system exhibited the greatest potential in terms of sintering response, mechanical properties and expected elevated temperature benefits from the Fe and Ni additions. Laboratory PM processing consisted of blending, compacting, sintering, and heat-treatment.

Various specimens of the most promising alloy were then blended and compacted in the laboratory (Dalhousie) and shipped to GKN (Conover) to be sintered industrially via a continuous mesh belt furnace under flowing nitrogen gas. This was performed as a means of assessing the feasibility of producing components in industrial-scale operations.

4.2.1 Blending

A variety of blends were required in this research. Unless otherwise noted, all chemistries are expressed in weight % (wt %) terms. The base (unmodified) PM2324 powder blend was created by initially weighing out the appropriate amounts of base Aluminum powder and the Al-Cu master alloy which were then blended together for 10 min in a nalgene bottle using a Turbula Model T2M mixer (Figure 33). After which, the remaining alloying additions (Mg, Sn) and ethylenebisstearamide lubricant were weighed out, combined with the Al + Al-50Cu pre-blend and then blended for an additional 35 min. Blends that contained elemental additions of Fe and/or Ni were created by the simple addition of a calculated amount (1%) of these additives to the unmodified PM2324 powder blend. These additions were weighed out and added to the Al + Al-50Cu pre-blend at the same time as the Mg, Sn and Licowax. Finally, pre-alloyed additions of Fe and Ni were made by simply replacing the pure Al powder employed in the baseline

(unmodified) version of PM2324 with one of the three pre-alloyed Al powders secured; namely, Al-1Fe, Al-1 Ni, and the ternary system Al-1Fe-1Ni. These powder blends were prepared under the same conditions and sequence as utilized in the preparation of unmodified PM2324.

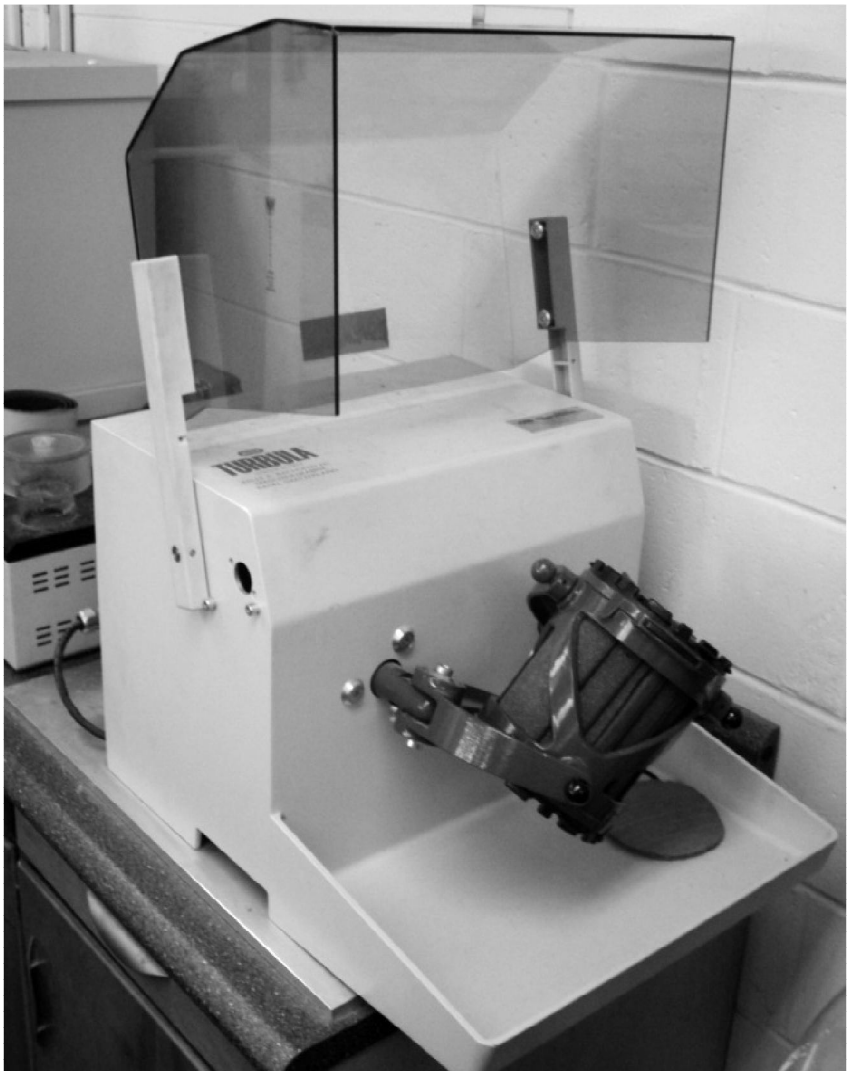

Figure 33 – Turbula T2M used to prepare powder blends.

4.2.2 Compaction

Powder compaction was performed using a Satec® Systems load frame (Figure 34) and three self-contained rigid floating die assemblies; one for producing transverse rupture stress (TRS) bars, a second for dog bone-style tensile bars, and a third for Charpy bars destined to be machined into threaded-end tensile bars. These tools and products are shown in Figure 35. Each type of bar required weighing out 10, 7, or 33 grams of the powder blend per bar, respectively. Procedurally, the powder was manually poured into the die and levelled using an adjustable ruler. The upper punch was then placed in the die assembly and the tooling then loaded at a rate of 2kN/s until the set pressure was achieved. This pressure was held for 5 seconds and released. The optimal compaction pressure for unmodified PM2324 was observed to be 400MPa in prior studies [31]. Therefore, all specimens (including Fe and Ni modified PM2324) were compacted at 400MPa, unless otherwise noted.

Figure 34 – Satec System model 5594-200HVL load frame.

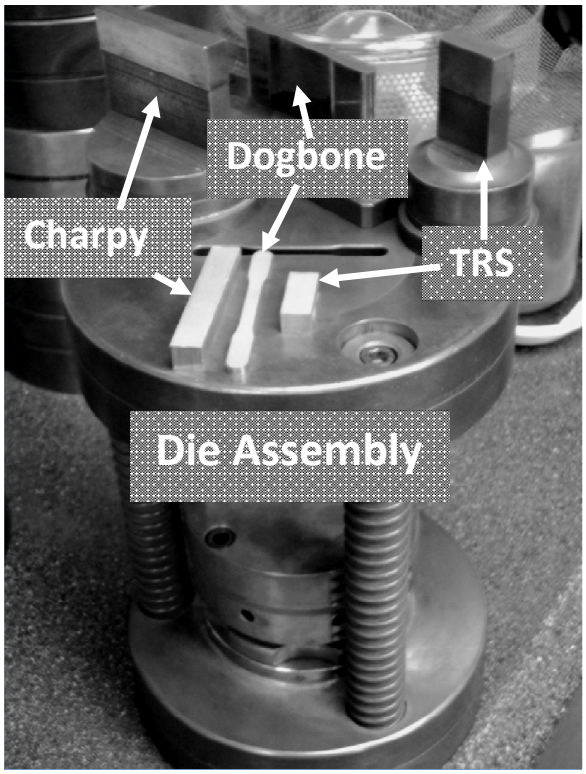

Figure 35 – Examples of the self-contained floating die assembly employed and the Charpy, dog bone, and TRS types of specimens fabricated.

4.2.3 Sintering

Sintering in the laboratory was performed under continuously flowing high purity (99.999%; 20 cc/min) nitrogen gas within a Lindberg/Blue tube furnace equipped with three UP150 controller modules (Figure 36). Each sintering cycle was performed in accordance with the thermal profile previously optimized for PM2324 (Figure 37). This profile first began with an increase in temperature which settled at approx. 400°C for 40 minutes to facilitate de-lubrication. The temperature was then increased to 604°C at which point the samples were sintered for ~20 minutes. After sintering, the samples were pushed into the water jacketed region of the tube furnace where they were quickly cooled to <100°C and removed from the furnace. During sintering, temperature was recorded using an OMEGA H506R thermocouple reader equipped with type a "K" thermocouple. Specimens sintered industrially at GKN were processed in a continuous mesh-belt furnace according to a thermal profile similar to that implemented in the laboratory.

Figure 36 – Lindberg/Blue 3-zone tube furnace used for laboratory sintering trials.

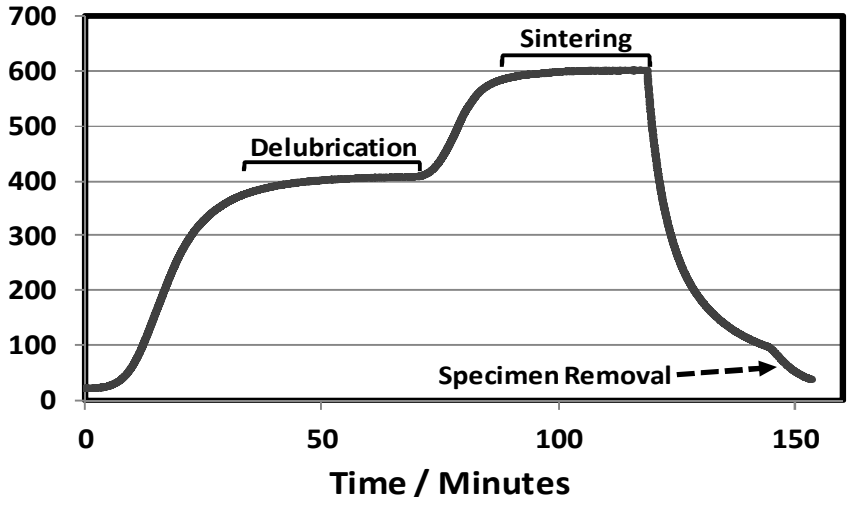

Figure 37 – Thermal profile followed when sintering specimens in a laboratory environment.

4.2.4 Heat-Treatment

T6 heat treatments were conducted by first solutionizing specimens at 495 ± 1.0˚ C in air for 2 hours using the muffle furnace shown in Figure 38. The bars were then removed from the furnace, quenched in water and then immediately placed in a fisher scientific mechanical convection oven for 10 hours of artificial aging at 190 ± 1.5˚C.

(a) (b)

Figure 38 – Images of the furnaces utilized for (a) solutionizing and (b) artificial age hardening.

4.3 Metallurgical Assessment Techniques

Specimens created during laboratory experiments were assessed in the green, as-sintered (T1), and heat treated (T6) conditions. Characterization of the former included evaluations of green density, green strength, and green microstructure. Characteristics pertinent to specimens in the T1 and T6 conditions emphasized sintered density, dimensional change, hardness, tensile properties, microscopy, and chemical analyses.

4.3.1 Green Strength and Density

The mechanical strength of as-compacted PM2324 TRS specimens was evaluated in accordance with ASTM standard B528 [62] using the fixture shown in (Figure 39). Before testing, several OAL (overall length), width (W), and length (L) measurements were recorded in millimetres (mm) and averaged for each bar. During testing, a

displacement rate of 0.05mm/s was applied until fracture so as to yield a value for the peak force (F) expressed in Newtons (N). The transverse rupture strength of the powder compacts, or green strength, was then calculated in MPa using the following equation:

$$\mathbf{G.S.} = \frac{(\mathbf{3}\times\mathbf{F}\times\mathbf{L})}{(\mathbf{2}\times(\mathbf{OAL})\times\mathbf{W})} \qquad \textbf{Equation 9}$$

The density of compacted powder specimens was determined using the Archimedes principal in accordance with MPIF standard 42 [63]. Initially, the mass of each TRS bar was measured in air (M_{air}) and then a second time but when submerged in water (M_{H2O}) using the scale shown in Figure 40. Green density calculations were then completed by calculating the density of the water (ρ_{H2O}) using equation 10 (where T is the temperature of the water) and then substituting this value into equation 11 along with values for M_{air} and M_{H2O}:

$$\boldsymbol{\rho_{H2O}} = \mathbf{7}\times\mathbf{10^{-8}T^3} - \mathbf{1}\times\mathbf{10^{-5}T^2} + \mathbf{1}\times\mathbf{10^{-4}T} + \mathbf{0.9996} \qquad \textbf{Equation 10}$$

$$\boldsymbol{\rho_G} = \frac{\mathbf{M_{air}}\times\boldsymbol{\rho_{H2O}}}{\mathbf{M_{air}} - \mathbf{M_{H2O}}} \qquad \textbf{Equation 11}$$

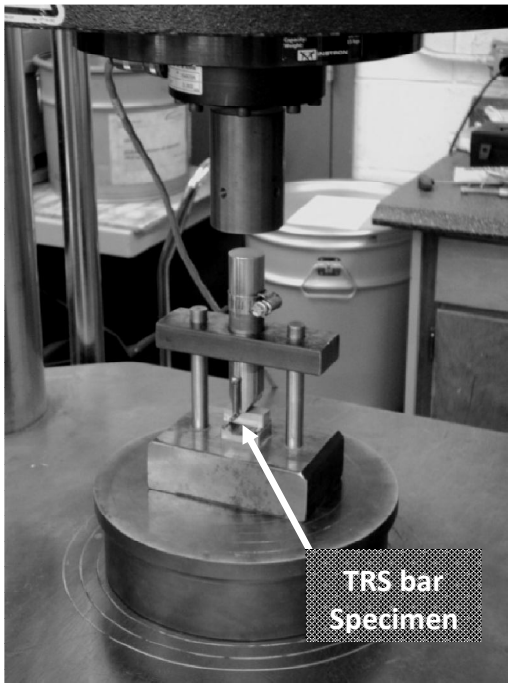

Figure 39 – 3- point bend test apparatus used to measure green strength.

Figure 40 – Digital scale used to measure the mass of TRS bars submerged in water.

4.3.2 Sintering Response

The general sintering response of all PM alloys was assessed by the extent of dimensional change and densification that occurred in TRS bars. The former was measured by taking several measurements of a given specimens OAL (overall length), length, and width before and after sintering. The dimensional change was then calculated as a percentage for each feature using equation 10 where the subscripts "i" and "f" denote initial (green) and final (sintered) values respectively. Using this approach negative values indicate shrinkage whereas positive values were synonymous with swelling.

$$\%\ \textbf{Dimensional Change} = \frac{\mathbf{D_f - D_i}}{\mathbf{D_i}} \times \mathbf{100} \qquad \textbf{Equation 12}$$

Sintered density measurements were made in accordance with MPIF standard 42 [63]. Here, the sintered TRS samples were first weighed in air (M_{air}). Each sample was then submerged in a beaker of ESSO-NUTO H46 hydraulic oil, that was placed under vacuum

atmosphere derived from a mechanical pump. Specimens were infiltrated with oil for 30 minutes, removed from the beaker and then lightly wiped to remove any excess surface oil before being weighed again in air ($M_{airw/oil}$). Finally, each impregnated sample was weighed again but when suspended in water ($M_{H2Ow/oil}$). Bulk specimen density was then calculated by again determining the water density (equation 10) and then using equation 13.

$$\rho_S = \frac{M_{air} \times \rho_{H2O}}{M_{airw/oil} - M_{H2Ow/Oil}} \qquad \textbf{Equation 13}$$

4.3.3 Mechanical Property Evaluation

The mechanical properties of all experimental PM2324 alloys were evaluated using apparent hardness and tensile testing techniques. Rockwell hardness measurements were made using a LECO R600 Rockwell-hardness testing machine within the B (HRB) scale (100 kgf, 1/16" ball indenter). Mean HRB hardness measurements were obtained from four indentations made on the top and bottom surfaces of a sintered TRS bar previously sanded to ensure a smooth flat surface, for a total of 8 measurements. All such tests were conducted in accordance with MPIF standard 43 [64].

Prior to tensile testing dog bone samples were lightly sanded to remove any burrs. This step consisted of sanding on a belt sander (120 grit SiC) followed by hand sanding using progressively finer grades of SiC paper (240, 400, and 600 grit). Three pairs of OAL and width measurements were then made along the gauge length of each bar; one at each end and one at in the middle to provide a more accurate sense of the initial cross sectional area. Conversely, machined tensile bars only required measuring the diameter along the gauge length once given the uniformity of such specimens. Tensile testing was then conducted with the same press used to compact the powders, but when equipped with a 50 kN load cell, in accordance with MPIF standard 10 [65]. Engineering stress/strain results were compiled and evaluated to determine the modulus of elasticity, yield strength, ultimate tensile strength, and maximum elongation of each sample tested. Modulus values were determined by measuring the slope in the elastic region of the stress

strain curve while yield strength values were determined by superimposing a line possessing the same slope as the modulus at an offset of 0.2% elongation. The ultimate tensile strength (UTS) and maximum elongation were easily determined by measuring the maximum stress and elongation to fracture, respectively.

Elevated temperature exposure of the unmodified and modified PM2324 alloys was achieved by placing the machined T6 tensile bars in a convection oven for a specific period of time and temperature. Specimens were then removed from the oven, cooled to ambient and then tested at a load rate of ~ 8.3 kN/s. Exposure periods of 0, 1, 10, 100, and 1000 hours were investigated at 120°C and 280°C, in addition to several 100 hour tests at intermediate temperatures of 160°C, 200°C, and 240°C. Four bars were tested per condition/alloy.

4.3.4 Thermal Analysis

A NETZSCH high temperature model 404 F3 Pegasus® differential scanning calorimeter (DSC) was used to monitor any possible residual dissolution/precipitation reactions of industrially sintered machined tensile specimens as a result of thermal exposure. DSC specimens were prepared from the fractured tensile bars first by machining to a diameter of 4 mm followed by grinding of the bars length using 240 to 600 grit emery paper to a height of approx. 1 mm. The objective was to obtain a specimen capable of fitting inside the ~ 6 mm diameter alumina crucible insert while ensuring the mass of the specimens was close to the recommended value of 22mg. Temperature and sensitivity calibration were achieved through repeated cyclic (heating-cooling) melting of a series of standards (Au, Bi, Al, etc.) in order to obtain mean melting point and enthalpy values. For each specific heating/cooling program used, the heat evolved between two empty Pt crucibles (with alumina inserts) positioned in the reference and specimen holder was recorded prior to the actual specimen analysis. During the tests themselves, DSC samples were first carefully placed in the alumina inserts within platinum crucibles. The apparatus was then purged using a mechanical pump and high purity argon gas, until a suitable vacuum was obtained (~4.0 $(10)^{-2}$ Mbar). After initialization, the temperature was increased at a rate

of 20°C/min from room temperature (25°C) to 550°C followed by slow cooling (furnace off) to approximately 115°C at which point the flow of argon gas was automatically stopped and the specimen allowed to cool to room temperature. High purity annealed Al was also examined and the data subtracted from all other tests to further highlight the endothermic and exothermic peaks attributable to precipitation-based reactions.

4.3.5 Metallographic Preparation

Samples subjected to microstructural inspection required transverse sectioning of TRS bars followed by cold mounting in epoxy resin under vacuum. Once fully cured, mounted samples were ground using 240 grit SiC paper until plane. Polishing involved a sequence of 9μm and 3μm diamond suspensions followed by colloidal silica. All grinding and polishing processes were performed using a Vector® Power Head auto-polisher.

4.3.6 SEM Microscopy EDS Chemical Analyses

Electron microscopy studies were completed using a Hitachi S-4700 field emission (FE) SEM equipped with an Oxford® X-Sight 7200 Energy Dispersive Spectroscopy (EDS) system. Such trials were completed under an acceleration voltage of 15-20 kV and a beam current of 15 μA. Polished mounts were rendered conductive using the same silver paint and examined in the unetched condition. Aside from general SEM imaging, average values for the composition of the base α-Al grains were also obtained. Here, 10 point scan energy dispersive spectroscopy (EDS) analyses were completed on grains randomly selected within the specimen and averaged.

4.3.7 X-ray Diffraction Analyses

X-ray diffraction (XRD) was used to obtain qualitative analyses of the phases present in raw powder blends as well sintered specimens in the T1 and T6 tempers. Sample preparation of all sintered specimens consisted of filing down TRS bars using a bastard file then screening through a 325 Mesh screen to obtain enough of the fine (-325 Mesh) fillings to adequately fill the XRD specimen holders. Raw powders were simply poured into the holders then levelled. The samples were then loaded into the Bruker AXS D8 Advance XRD system shown in Figure 41. This unit was operated with a Copper K_α x-ray source using a tube voltage of 40 kV and tube current of 40 mA. After scanning, the acquired spectrums were analyzed using EVA™ analytical software which was used for background and K_α x-ray peak removal, and phase identification.

Figure 41 – Bruker AXS D8 Advance XRD apparatus.

Chapter 5 Materials

Unmodified PM2324 Aluminum powder blends were created from a total of four different powders, blended together in specific weight fractions to yield a final powder blend possessing a nominal composition of 4.4 wt % Cu, 1.5 wt % Mg and 0.2 wt % Sn (Al remainder). This required the use of air atomized Aluminum powder, a milled Al-50Cu master alloy, gas atomized Mg, and air atomized Sn. Five additional powders were used to incorporate Fe and Ni into PM2324, the first two being elemental Fe and Ni powders and the other three pre-alloyed Aluminum powders containing 1 wt% Fe, 1 wt% Ni, and 1 wt% Fe + 1 wt% Ni. The elemental carbonyl nickel and atomized Fe powders were procured from Vale INCO [66] and Hoganas Corporation [67] respectively. While all three pre-alloyed powders were manufactured at Ecka granules, Germany via air atomization. Additionally, an ad-mixed ethylenebisstearamide lubricant (Licowax™ C) was also added at a concentration of 1.5 wt% during blending to facilitate compaction. Using these powders, seven different blends were prepared throughout the course of the experiments in this report. These were the unmodified baseline PM2324 alloy (Al-4.4Cu-1.5Mg-0.2Sn) plus six variants of this system with each containing elemental or pre-alloyed additions of 1Fe, 1Ni, or 1Fe + 1Ni on a weight % (wt%) basis.

Figure 42 and Figure 43 display the particle size distribution measurements obtained for all powders of interest by laser particle size analysis. Similarly, SEM images taken of base Al powders and alloying additions are shown in Figure 44 and Figure 45.

The chemical assays of each powder employed are listed below in Table 9 and Table 10.

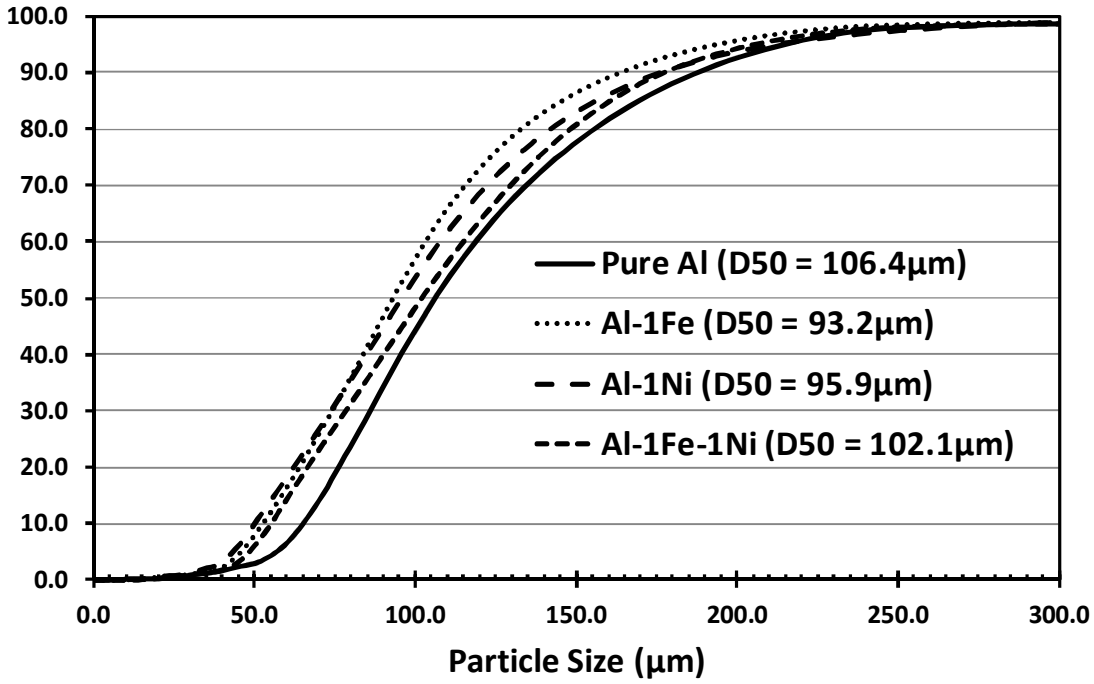

Figure 42 – Particle size distribution data of pure and pre-alloyed base Al powders.

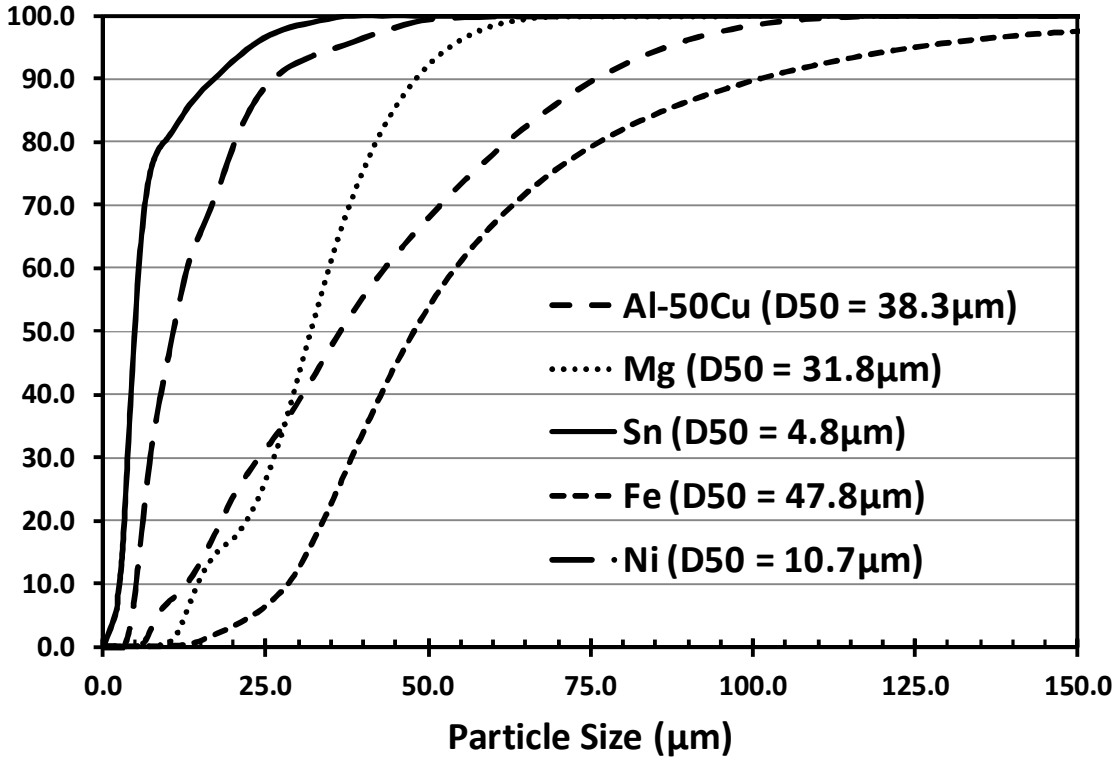

Figure 43 – Particle size distribution data of all powder alloying additions.

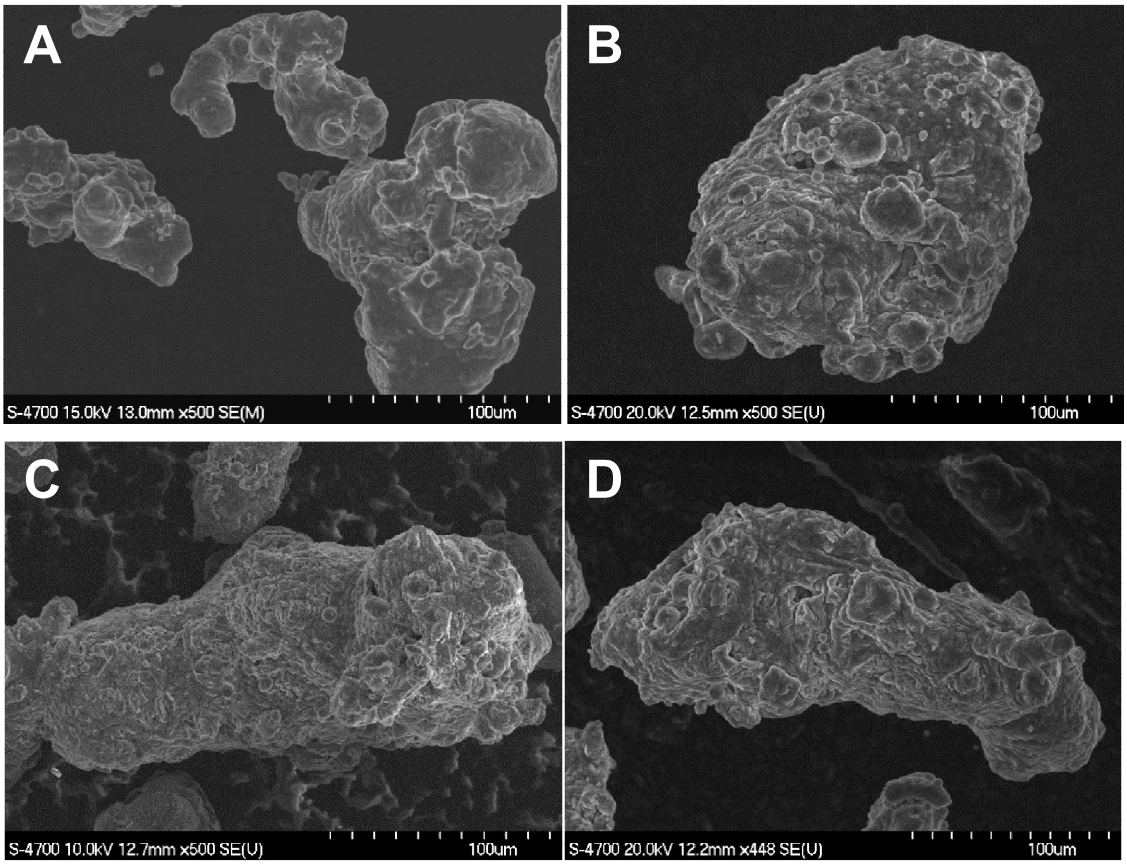

Figure 44 – SEM images of air atomized pure and pre-alloyed base Al powders. (A) Pure Al, (B) Al-1 wt% Fe, (C) Al-1 wt% Ni, and (D) Al-1 wt% Fe-1 wt% Ni.

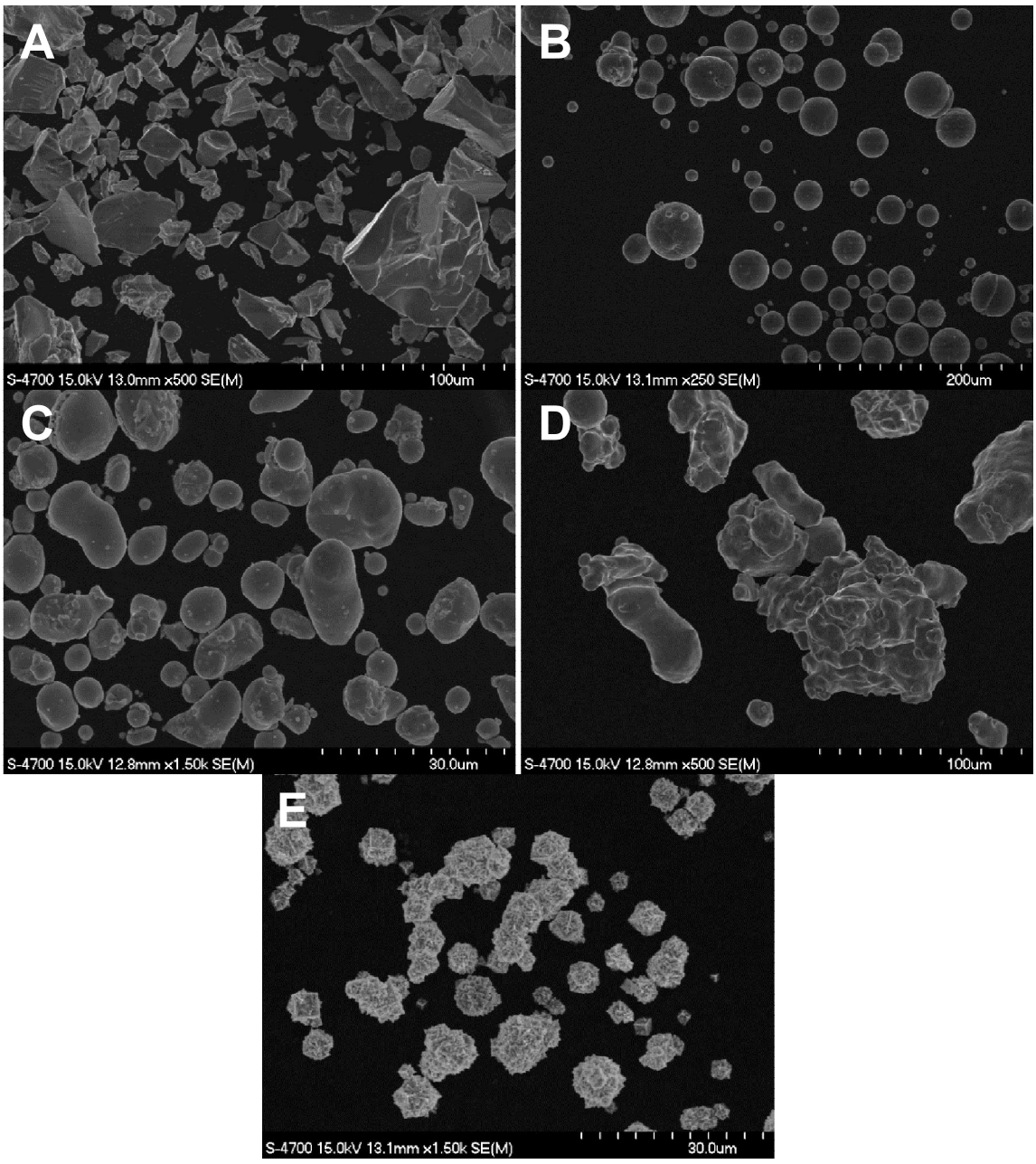

Figure 45 – SEM images of powder alloying additions. (A) Milled Al-50Cu master alloy, (B) Gas atomized Mg, (C) air atomized Sn, (D) water atomized Fe, and (E) carbonyl Ni.

Table 9 – Chemical composition of base Aluminum powders [59].

Powder	Composition (wt%)						
	Al	Cu	Mg	Sn	Fe	Ni	Other
Pure Al	Bal.	0.011	<0.001	<0.001	0.136	0.004	0.016
Al + 1 Fe	Bal.	0.009	<0.001	<0.001	1.081	0.002	0.021
Al + 1 Ni	Bal.	0.013	<0.001	<0.001	0.088	1.033	0.022
Al + 1 Fe + 1 Ni	Bal.	0.011	<0.001	<0.001	1.022	0.946	0.024

Table 10 – Chemical Composition of powders reported by manufacturers.

Powder	Composition (wt%)						
	Al	Cu	Mg	Sn	Fe	Ni	Other
Al-50Cu	49.6	Bal.	-	-	-	-	0.3
Mg	0.01	-	Bal.	-	-	-	0.12
Sn	-	-	-	Bal.	-	<0.185	0.11
Fe*	-	<0.10	-	-	Bal.	<0.080	0.14
Ni**	< 0.005	-	-	-	-	Bal.	0.20

*** See references for complete manufacturer information sheet [67]**

*** * See references for complete manufacturer information sheet [66]**

Chapter 6 Compaction Behaviour of PM2324 Alloys

The bulk characteristics of powders either loose or compressed as a green compact are crucial in understanding the processing behaviour of a particular blend and the resultant properties of final products. Simple measurements such as flow rate, apparent density (AD) and green density can reveal a variety of intrinsic characteristics of the material. In industry, the ability to consistently reproduce high quality products possessing consistent mechanical properties can be attributed to upstream powder manufacturing conditions which can yield small variations in the particle attributes. For example, if complications were observed with sintered density an abnormal flow rate could indicate less irregular particles (more spherical) which could then be related to variations in powder atomization parameters such as gas flow rate, melt temperature, nozzle size, etc.. Accordingly, these basic tests can provide valuable precursory information that can help avoid larger problems.

Flow and AD measurements obtained from all PM2324 powder blends are listed in Table 11. These data indicated that the Fe and Ni additions had little to no effect on these attributes. All powder blends were free flowing with comparable densities in the loose powder state. Data on the green density and green strength measured in compacts pressed at 400MPa are shown in Table 12. These data highlight the exceptional compressibility generally observed in Aluminum PM, as shown by the gain in density upon compaction from the loose powder to a coherent green compact. In general, green density was not influenced by the transition metal additions whereas they were found to improve green strength. Once added, the green strength remained relatively consistent for the alloys assessed regardless of the nature or concentration of Fe and Ni employed. This behaviour was slightly unexpected as pre-alloyed powders are typically much harder than pure, elemental counterparts. Accordingly, they are more resistant towards deformation which generally makes them more difficult to compact. It is speculated that this behaviour may be attributed to a slightly finer size distribution of pre-alloyed powder particles relative to the pure Aluminum (Figure 42).

Table 11 – Effects of elemental and pre-alloyed Fe and Ni additions on the flow rate and AD of PM2324 powder blends.

Alloy	Nature of Transition Metal Addition	Flow Rate (g/s)	AD (%)
PM2324	**N/A**	**2.86** ±0.07	**45.1** ±0.1
PM2324 + 1Fe	**Elemental**	**2.84** ±0.04	**46.7** ±0.2
	Pre-Alloyed	**2.70** ±0.10	**45.5** ±0.1
PM2324 + 1Ni	**Elemental**	**2.92** ±0.13	**46.8** ±0.2
	Pre-Alloyed	**2.67** ±0.18	**47.1** ±0.1
PM2324 + 1Fe + 1Ni	**Elemental**	**2.84** ±0.05	**45.9** ±0.1
	Pre-Alloyed	**3.05** ±0.11	**45.7** ±0.1

Table 12 – Effects of elemental and pre-alloyed Fe and Ni additions on the compaction response of PM2324 powder blends.

Alloy	Nature of Transition Metal Addition	Green Density		Green Strength (MPa)
		g/cc	%	
PM2324	***N/A***	***2.64 ±0.003***	***98.0 ±0.10***	***9.7 ±0.16***
PM2324 + 1Fe	Elemental	**2.66** ±0.001	**97.9** ±0.02	**9.7** ±0.08
	Pre-Alloyed	**2.65** ±0.001	**97.8** ±0.04	**11.9** ±0.15
PM2324 + 1Ni	Elemental	**2.66** ±0.001	**98.1** ±0.04	**12.2** ±0.81
	Pre-Alloyed	**2.66** ±0.001	**97.9** ±0.04	**12.1** ±0.22
PM2324 + 1Fe + 1Ni	Elemental	**2.68** ±0.001	**97.9** ±0.02	**11.5** ±0.24
	Pre-Alloyed	**2.65** ±0.001	**97.1** ±0.05	**12.1** ±0.04

SEM analyses were performed on green compacts prepared from each blend as a means of observing the microstructural attributes prior to sintering, for example the deformation of the base Aluminum powders and the distribution and morphology of the Fe and Ni

additions. Figure 46 reveals the unetched green microstructure of all elemental (left) and pre-alloyed (right) powder compacts formed at 200 MPa. A dendritic microstructure can clearly be seen within the pre-alloyed powder particles while this was not observed in those of elemental Al. It is believed that the lighter color dendritic features were Al-(Fe, Ni, Fe + Ni) rich phases that had segregated to the inter-dendritic regions upon solidification. Unfortunately, their small size precluded accurate chemical analyses using the EDS system on the SEM. Also evident from these images is the considerable level of deformation exhibited by the comparatively softer pure Al versus the harder, pre-alloyed powders. Furthermore, the green microstructure of PM2324 + 1Fe + 1Ni powder compacts provides good comparison between the relatively fine size of the carbonyl Ni versus that of atomized Fe, as well as the resistance of the pre-alloyed Al-1Fe-1Ni powders to plastic deformation. In all instances it was apparent that the Al-50Cu master alloy particles were the hardest species present as even the hardened pre-alloyed particles had deformed around them. Due to their small size and limited concentrations Mg and Sn proved difficult to locate.

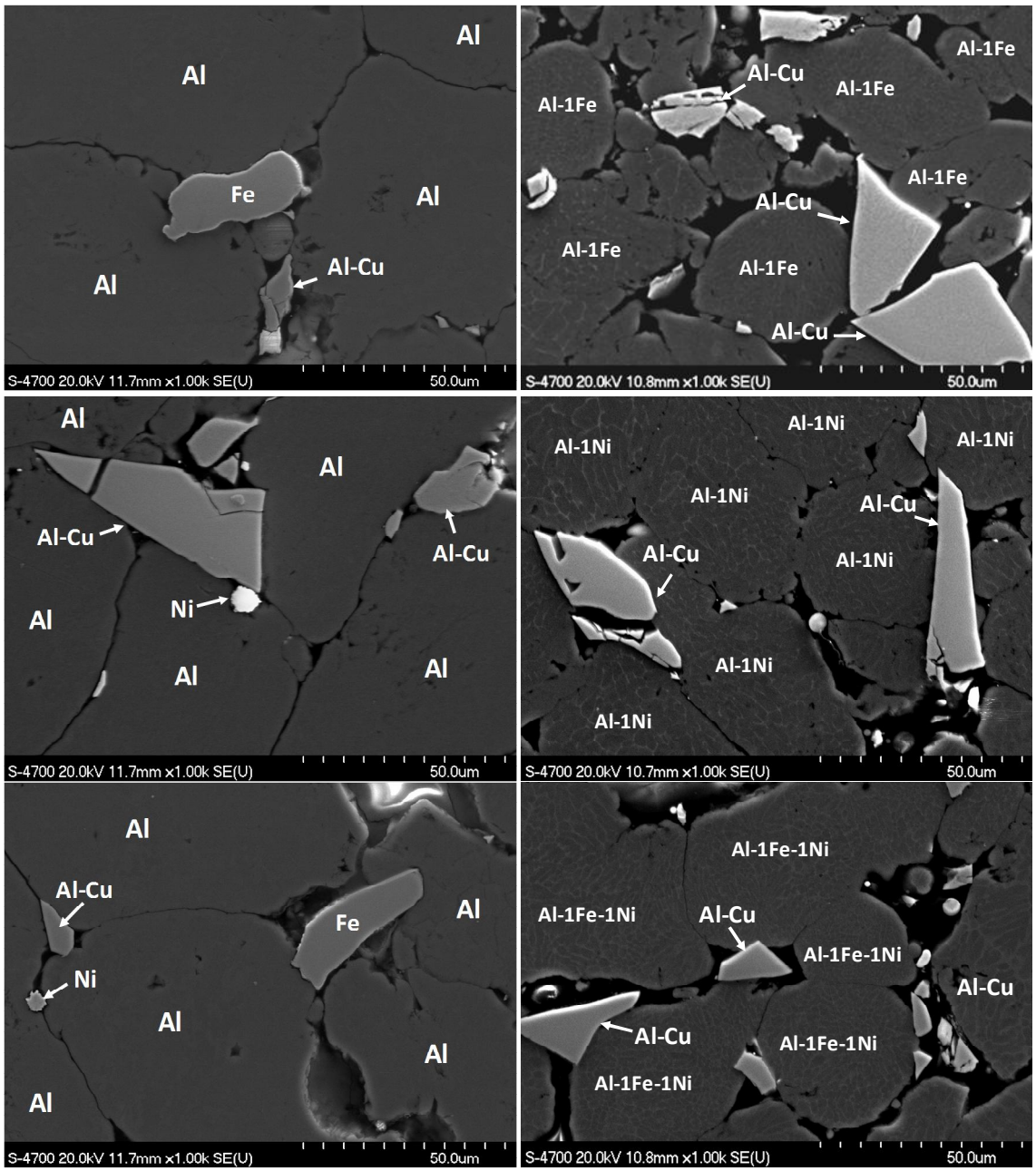

Figure 46 – SEM images taken of the green microstructures of elemental (left side) and pre-alloyed (right side) PM2324 + 1 wt% Fe (top), PM2324 + 1 wt% Ni (middle) and PM2324 + 1 wt% Fe + 1 wt% Ni (bottom). All specimens compacted at 200 MPa.

Chapter 7 Development of an Al-Cu-Mg-(Fe)-(Ni) Powder Metallurgy Alloy – Part 1: Processing and Properties

***Eric D. Moreau (Eric.Moreau@dal.ca)**
****I.W. Donaldson (Ian.donaldson@gknsintermetals.com)**
*****R.L. Hexemer Jr., (Rich.Hexemer@gknsintermetals.com)**
***D.P. Paul Bishop (Paul.Bishop@dal.ca)**

*Materials Engineering, Department of Process Engineering and Applied Sciences, Dalhousie University, 1360 Barrington St., Halifax, Nova Scotia, Canada
** GKN Sinter Metals, 3300 University Drive, Auburns Hills, Michigan, USA, 48326
*** GKN Sinter Metals, 407 Thornburg Drive, Conover, North Carolina, USA 28613

Status: **Submitted to Canadian Metallurgical Quarterly**

Keywords: **Powder Metallurgy, Aluminum-Copper-Magnesium Alloys, Compaction, Sintering, Iron, Nickel, Thermal Exposure**

The following experimental procedures, analysis and discussions were completed by E.D. Moreau, with reviewer and editorial roles played by the other authors.

Abstract

The effects of Fe and Ni additions to an Al-Cu-Mg powder metallurgy alloy were studied. The transition elements were incorporated through two different approaches – admixed elemental powders and pre-alloying of the base Al powder. Pre-alloying proved to be the superior alloying technique as it did not invoke any negative effects on the general sintering behaviour of the baseline alloy. The microstructures of pre-alloyed materials also exhibited a refined distribution of the aluminide phases formed. These included Al_7Cu_2Fe, Al_7Cu_4Ni, and Al_9FeNi as identified through a combination of SEM/EDS and XRD. The most promising alloy was identified as Al-4.4Cu-1.5Mg-1Fe-1Ni as it exhibited tensile properties that exceeded those of the baseline material. This advantage was also found to persevere after thermal exposure.

7.1 Introduction

High performance Aluminum (Al) powder metallurgy (PM) alloys have seen increased utilization in the manufacture of automotive engine components such as gears and bearing caps in an effort to realize weight and/or cost savings. In such applications, a universal issue concerning the use of Aluminum alloys produced by any means is the gradual degradation of their mechanical properties during prolonged thermal exposure. In comparison to steels, where service temperatures between 150-300˚C have a negligible effect on strength, Al alloys (especially those that are heat treated) can experience considerable losses in mechanical performance. In an attempt to mitigate this issue, a common tactic has been the deliberate incorporation of transition metal additions such as Fe and Ni. In contrast to the elements associated with precipitation hardening (i.e. Cu, Mg, Zn, etc.), Fe and Ni have negligible solid solubility in Al. As such, these elements tend to form a stable dispersion of hard intermetallic phases such as Al_9FeNi that have a high melting point and thereby act to enhance elevated temperature properties of the alloy [44].

When considering Al PM alloys, Fe and Ni additions can be made through a number of techniques. For example, they can be added as discrete elemental powder particles that react in-situ during sintering to form intermetallic dispersoids. This approach represents an economical means of incorporation but is apt to yield a coarsened distribution of Al-Fe-Ni based intermetallics in the sintered product given sluggish diffusion rates, relatively coarse particle sizes, and low solid solubilities in Al [56]. In another scenario Fe and Ni can also be pre-alloyed into the base Al powder during atomization. This process causes the Fe and Ni to be retained in the Al powder in a highly refined and uniformly dispersed condition [59]. While this does not carry a direct cost burden, the potential disadvantage of this approach is that it generally increases the hardness of powder particles, potentially making them more difficult to compact. Work done by Xiang [57] and Duan [58] on a fully pre-alloyed version of 2024 with Fe and Ni using both hot extrusion and liquid dynamic compaction accompanied by hot rolling,

respectively, resulted in successful incorporation of relatively high concentrations (> 2 wt%) of the elements. However, both authors implemented PM processing equipment unsuitable for high-throughput "press and sinter" production that is required when producing components for the automotive industry.

To date, there has been little research completed on the effects of Fe and/or Ni additions on commercial press-and-sinter Al PM alloys. The authors now seek to address this issue using an emerging Al PM alloy [31] as the baseline system of interest. Denoted as PM2324 (Al-4.4Cu-1.5Mg-0.2Sn), this alloy has shown promise for commercial exploitation given the intense densification that transpires during sintering and concomitantly, its high strength relative to traditional PM alloys such as AC2014 [32]. As such, the specific objectives of the present study are to assess the influence of Fe and Ni additions on the PM processing response of PM2324 so as to determine if the inclusion of these elements is technologically feasible and if this then invokes any gains in thermal stability for the alloy.

7.2 Materials

In creating the baseline PM2324 blend, elemental Al powder (air atomized; Ecka Granules, Feurth, Germany) was blended with an Al-50Cu master alloy, and elemental sources of Mg and Sn in the weight fractions needed to produce a final powder blend with a nominal composition of 4.4 wt % Cu, 1.5 wt % Mg and 0.2 wt % Sn (Al remainder). An admixed ethylenebisstearamide lubricant (Licowax™ C) was also added at a concentration of 1.5 wt% during blending to facilitate die compaction. In one sequence of experiments Fe and/or Ni were incorporated as admixed elemental powders into this baseline alloy. The Fe powder was produced via water atomization at Hoeganes Corporation (Cinaminson, NJ, USA; Ancorsteel 1000C). The elemental Ni powder was produced through carbonyl vapour metallurgy (INCO-Vale; Type 123 powder). In another series of trials, Fe and Ni additions were achieved by producing customized Al powders pre-alloyed with the required transition metal(s). These powders, like the elemental Al employed, were also produced by air atomization at Ecka Granules.

Chemical assays for all powders are shown in Table 13 whereas data on particle sizes are provided in Table 14. Using these powders, seven different blends were prepared throughout the course of the experiments in this report. These were the unmodified baseline PM2324 alloy (Al-4.4Cu-1.5Mg-0.2Sn) plus six variants of this system with each containing elemental or pre-alloyed additions of 1Fe, 1Ni, or 1Fe + 1Ni on a weight % (wt%) basis.

Table 13 - Chemical assays of the powders employed as measured by ICP-OES. All measurements are in weight % (wt%).

Powder	Composition (wt%)						
	Al	Cu	Mg	Sn	Fe	Ni	Other
Pure Al	Bal.	0.011	<0.001	<0.001	0.136	0.004	0.016
Al + 1 Fe	Bal.	0.009	<0.001	<0.001	1.081	0.002	0.021
Al + 1 Ni	Bal.	0.013	<0.001	<0.001	0.088	1.033	0.022
Al + 1 Fe + 1 Ni	Bal.	0.011	<0.001	<0.001	1.022	0.946	0.024
Al-50Cu	49.6	50.1	-	-	-	-	0.3
Magnesium	0.01	-	Bal.	-	-	-	0.12
Tin	-	-	-	Bal.	-	<0.18	0.11
Iron	-	<0.10	-	-	Bal.	<0.08	0.14
Nickel	< 0.005	-	-	-	-	Bal.	0.20

Table 14 - Particle size data on the powders employed. All measurements are in microns and were achieved through laser light scattering (Malvern model 2600c).

Powder	D_{10}	D_{50}	D_{90}
Pure Al	65	106	188
Al + 1 wt% Fe	54	93	164
Al + 1 wt% Ni	50	96	176
Al + 1 wt% Fe + 1 wt% Ni	55	102	178
Al-50Cu	14	38	78
Magnesium	14	32	48
Tin	2	5	17
Iron	28	48	101
Nickel	5	11	26

7.3 Experimental Procedures

Raw blends of the required alloys were prepared by blending the appropriate combinations of powders with a Turbula mixer for 30 minutes. Powder compaction was then performed using a Satec® Systems load frame and three self-contained rigid floating die assemblies - one for producing transverse rupture stress (TRS) bars, a second for dog bone tensile bars, and a third for Charpy bars. In all instances, load was applied at a rate of 2kN/s until the target pressure was achieved. The optimal compaction pressure for unmodified PM2324 was found to be 400MPa in prior studies [31]. Hence, all specimens (including those that were modified with Fe and/or Ni additions) were compacted at this pressure. Sintering was performed under continuously flowing high purity (99.999%) nitrogen gas within a Lindberg 3-Zone tube furnace. Each sintering cycle was performed in accordance with the thermal profile previously optimized for PM2324 [32]. Sintered density measurements were made in accordance with MPIF standard 42 [63]. Here, sintered TRS bars were subjected to a standard Archimedes style of test using oil infiltration to seal the pores and prevent water ingression. The net dimensional change that transpired in a given powder compact as a result of sintering was measured by taking several thickness (overall length; OAL), width, and length measurements of the TRS samples in the green and sintered condition and calculating the percentile change.

The heat treatment (T6 process) of specimens began by solutionization at 495 ± 2.0˚ C in air for 2 hours. The bars were then quenched in water and artificially aged to peak strength at 190 ± 2˚C for 10 hours. Rockwell hardness measurements were made on the T6 bars per MPIF Standard 43 [64] using a Leco R600 Rockwell-hardness testing machine operated in the B (HRB) scale. Mean hardness measurements were calculated from a total of 8 indentations split evenly between the top and bottom surfaces of sintered TRS bars. Tensile properties were assessed on specimens in the T6 temper using dog bones and machined Charpy bars. Dog bones were employed when measuring the general properties at room temperature of the various alloys assessed. Machined Charpy

bars (round threaded end specimens; gauge length = 25mm; gauge diameter = 6mm) were utilized when assessing the effects of thermal exposure (isothermal hold at 160°C for 100h prior to testing). All tensile testing was conducted at ambient in conformance with MPIF Standard 10 [65] with the same press used to compact the powders, but when equipped with a 50 kN load cell and an axial extensometer that remained attached to the specimen through to fracture.

Microstructural analyses were accomplished through a combination of scanning electron microscopy (SEM) and x-ray diffraction (XRD). For the former, a TRS bar was cut and cold mounted in epoxy resin under vacuum. Mounted samples were then ground using 240 grit SiC paper and rough polished with 9μm and 3μm diamond suspensions. Final polishing was completed with colloidal silica. All grinding and polishing processes were performed using a Buehler Vector® Power Head auto-polisher. Finished samples were examined with a Hitachi S-4700 SEM equipped with an Oxford® X-Sight 7200 Energy Dispersive Spectroscopy (EDS) system. SEM studies were completed under a 20 kV acceleration voltage and a beam current of 15 μA. To determine the nominal compositions of the α-Al grains, 10 point scans were taken of random grains and averaged. Data on the phases present in a given alloy were acquired through x-ray diffraction (XRD). Here, filings were removed from a bulk specimen, screened to remove the particles >45μm and then examined with a Bruker D8 Advance (Cu K Radiation; tube current 40mA; tube voltage 40kV) equipped with a high speed LynxEye™ Silicon strip detector.

7.4 Results and Discussions

Results have been organized on the basis of the different additions considered. Namely, Fe additions, Ni additions, and combined Fe + Ni additions. In all instances, data on the measured properties of the unmodified PM2324 alloy are also included as a means of gauging if the modifications were beneficial or detrimental.

7.4.1 *Fe Additions to PM2324*

Table 15 provides data on the density and dimensional change obtained from TRS bars sintered with and without Fe additions. Relative to green compacts, the sintered density of unmodified PM2324 had increased as a result of sintering. A similar, although less acute, trend had occurred in the alloy prepared with pre-alloyed Fe. Conversely, the opposite behaviour was noted in the blend prepared with elemental Fe. Here, an appreciable loss in density transpired during sintering. These results were consistent with dimensional change data. In this sense, the unmodified PM2324 and that prepared with pre-alloyed Fe experienced appreciable shrinkage in all three dimensions. Accordingly, relatively high sintered densities were measured for these alloys. Conversely, elemental Fe additions caused considerable swelling consistent with the loss of density relative to green compacts.

Table 15 - Nominal sintering response of PM2324 modified with 1 wt% Fe.

	Density (%)		Dimensional Change (%)		
	Green	Sintered	OAL	Width	Length
Unmodified	***98.0*** *±0.1*	***98.7*** *±0.4*	***-2.07*** *±0.7*	***-1.67*** *±0.1*	***-1.24*** *±0.1*
Elemental Fe	**97.9** ±0.1	**93.8** ±0.5	**+1.30** ±0.2	**+0.29** ±0.1	**-0.42** ±0.1
Pre-Alloyed Fe	**97.8** ±0.1	**98.0** ±0.2	**-1.50** ±0.1	**-1.67** ±0.1	**-1.49** ±0.1

Corresponding data on the hardness and tensile properties of the alloys are shown in Table 16. Again, the unmodified alloy and that prepared with pre-alloyed Fe bore similar results. The only exception was tensile ductility wherein it appeared that pre-alloying had imparted a modest reduction in this attribute. The properties were severely degraded by the presence of elemental Fe. Relative to the unmodified alloy, hardness was reduced by 18 points, yield strength and UTS by over 100MPa and ductility was lowered by a factor of >2. Such observations were consistent with the relatively low sintered density (Table 15).

Table 16 - Mechanical properties of PM2324-T6 modified with 1 wt% Fe.

	Hardness (HRB)	**E** (GPa)	**Yield Strength** (MPa)	**UTS** (MPa)	**Elongation** (%)
Unmodified	***72*** *±2*	***69*** *±6*	*277 ±12*	***295*** *±25*	***1.1*** *±0.5*
Elemental Fe	**54** ±4	**56** ±6	**171** ±2	**171** ±2	**0.5** ±0.1
Pre-Alloyed Fe	**72** ±1	**70** ±3	**312** ±10	**315** ±10	**0.7** ±0.1

In an attempt to understand the factors responsible for the relatively benign effects of pre-alloyed Fe versus the dramatic losses noted with elemental additions, the microstructures of the alloys were examined through SEM techniques. That of unmodified PM2324 (Figure 47) revealed the presence of multiple phases. One was the α-Al grains (dark grey). This feature had an average composition that was comparable to the bulk alloy chemistry (Table 17). The second was a network of bright features, indicating that it had a relatively high average atomic number. It was also sparsely distributed throughout the microstructure and consistently located along the α-Al grain boundaries. Furthermore, EDS analyses indicated that it was enriched in Al, Mg and Cu. Prior studies on this alloy have confirmed that this network represents the solidified remnants of the persistent liquid phase that was present during sintering and that it is primarily comprised of the θ ($CuAl_2$) phase [4][59]. Only low levels of residual porosity (black) were apparent in microstructure which was in agreement with the high fractional density measured (Table 15). Overall, the unmodified alloy was typical of a well sintered material.

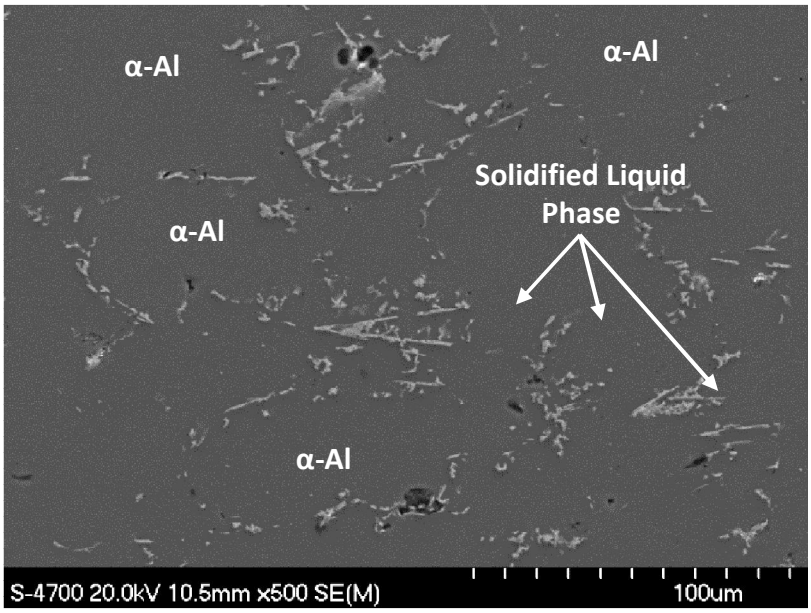

Figure 47 - SEM image of the polished (unetched) microstructure of unmodified PM2324-T6. Examples of the principal features are noted. Residual porosity is black.

SEM images of the alloys modified with Fe are shown in Figure 48. Beginning with the specimen that was modified with elemental Fe powder, this alloy again contained grains of α-Al. However, they were now more dilute in Cu on average than those present in the unmodified alloy (Table 17). A large secondary feature was also present in the alloy. EDS analyses implied the presence of the Al_7Cu_2Fe intermetallic within this feature. A significant reduction in the amount of solidified liquid was also noted. Residual porosity was clearly obvious in the material but was now present in a greater concentration and as much larger pores. XRD analyses confirmed that the dominant phases were α-Al and Al_7Cu_2Fe (Figure 49). The phase associated with the solidified liquid (θ) was not detected. Per Figure 48(a), it would appear that minor fractions of other phases were indeed present within the alloy. Evidently, the concentrations of these species were below the detection limits of XRD. The counterpart system prepared with pre-alloyed Fe (Figure 48(b)) exhibited a significantly different microstructure. In this alloy the intermetallics were much smaller in size and more uniformly distributed. Most of these exhibited a needle-like morphology that was <1μm thick, preventing accurate EDS analyses. Furthermore, a much lower concentration of residual porosity was present.

Aside from these differences, the one consistent feature was the near absence of features that appeared to be the remnants of the solidified liquid phase. These observations were supported by XRD (Figure 49) as again, only α-Al and Al_7Cu_2Fe were detected.

Although both sources of Fe additions reacted to ultimately form the same phase (Al_7Cu_2Fe) the paths followed in reaching this reaction product differed and as such, impacted the overall sintering response in different ways. For elemental Fe, these powder particles would have been in direct contact with the Cu-rich liquid formed when the Al-50Cu master alloy particles first melted. This scenario would have allowed Al_7Cu_2Fe to form early in the sintering cycle. As a result, the system would have been rapidly deprived of the liquid needed to engage liquid phase sintering and its associated mechanisms of densification. In a pre-alloyed form, the Fe was uniformly dispersed within the Al particles prior to sintering. Hence, the Al_7Cu_2Fe phase could only be formed after Cu diffused into the solid Al powder particles. Under these circumstances, the Al-50Cu master alloy would have melted and then had sufficient time to spread throughout the compact via a combination of wetting and capillary action. This would have invoked appreciable densification through the mechanism of particle rearrangement - a phenomenon that transpires within the first few minutes of sintering and is known to account for the majority of densification in similar Al PM alloys [56][59]. Eventually, the majority of Cu would have diffused from the liquid and into the Al particles. This would have formed Al_7Cu_2Fe and depleted the system of liquid once again, but only after densification of the alloy occurred. Collectively, these results confirmed that the pre-alloying method provided an effective means of incorporating Fe into PM2324 without a significant reduction in sintering response or mechanical properties.

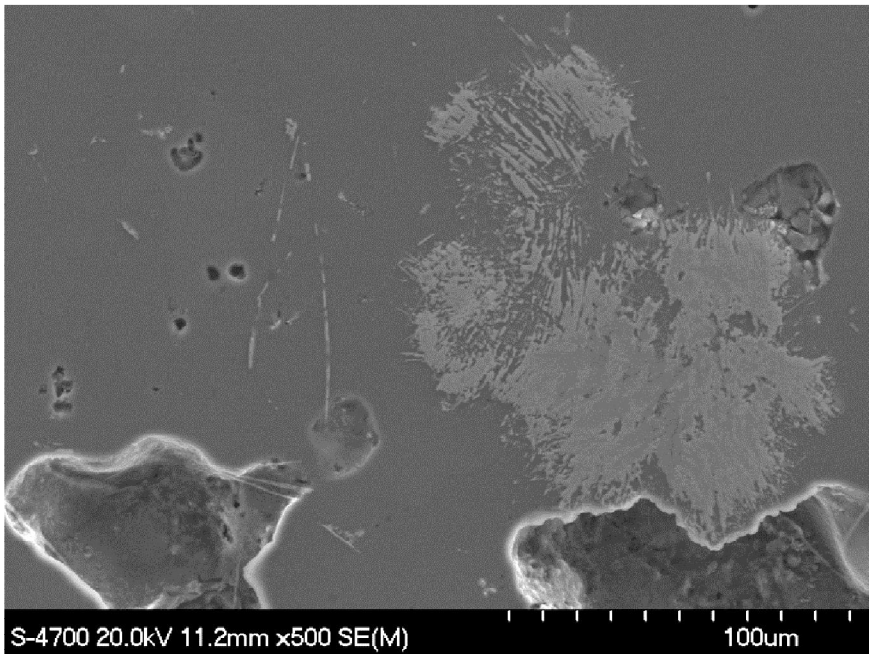

(a)

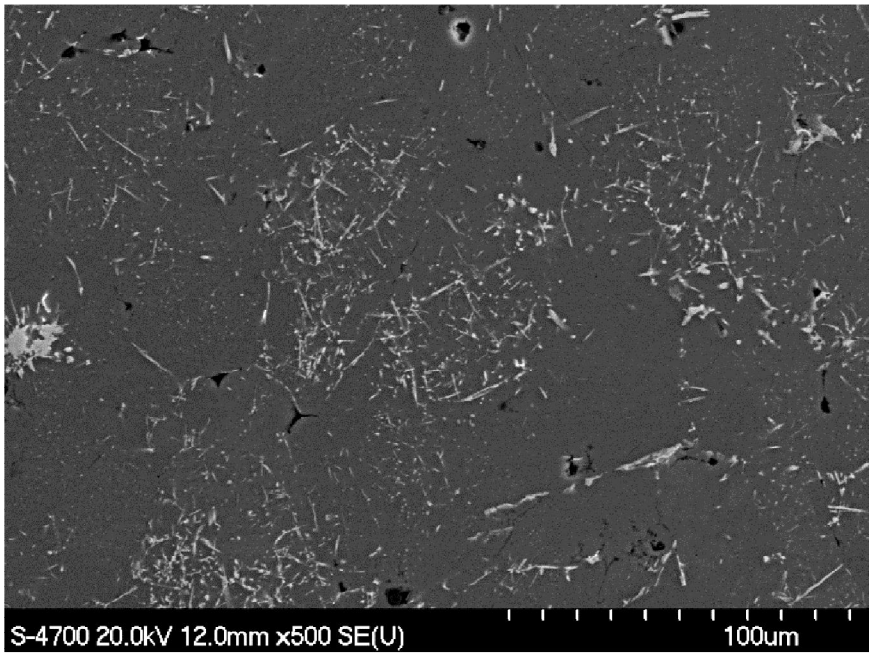

(b)

Figure 48 - SEM images taken of the polished (unetched) microstructure of PM2324-T6 modified with 1 wt% Fe as an (a) elemental and (b) pre-alloyed addition.

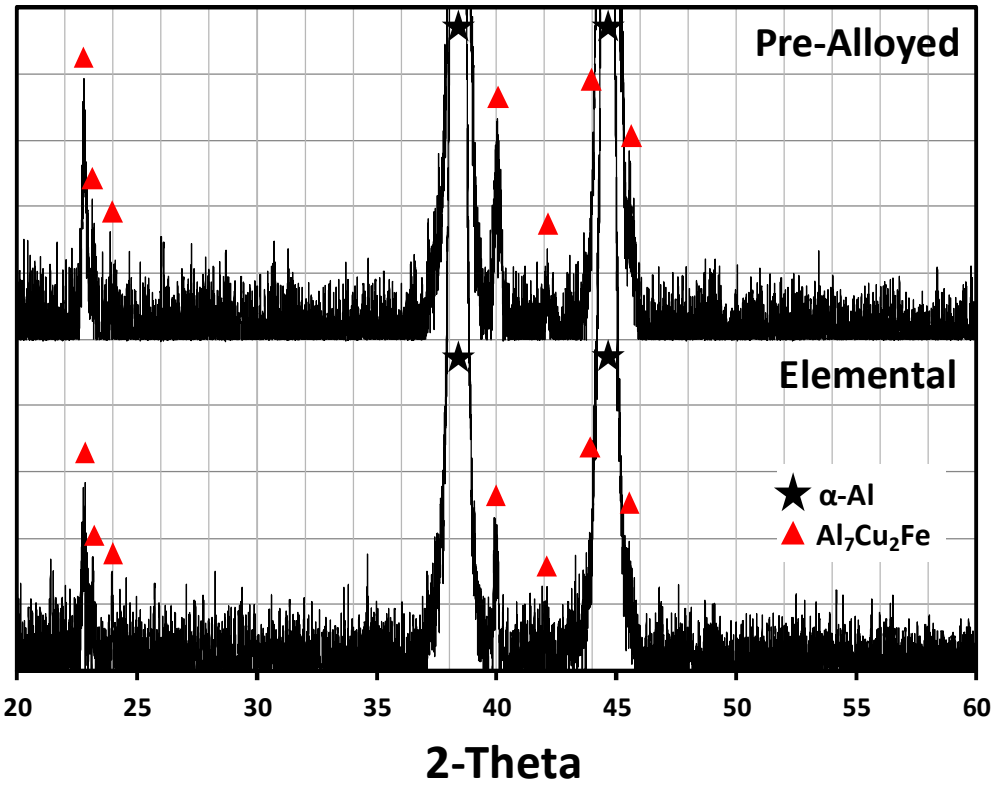

Figure 49 – XRD patterns recorded from samples of PM2324-T6 modified with 1 wt% Fe added as an elemental and pre-alloyed addition.

Table 17 - Mean chemistries of the α-Al grains in PM2324-T6 modified with 1 wt% Fe.

	Mean α-Al Composition (wt%)		
	Al	Cu	Mg
Unmodified	***94.2 ± 0.3***	***4.6 ± 0.2***	***1.2 ± 0.1***
Elemental Fe	94.6 ± 0.2	4.2 ± 0.1	1.2 ± 0.1
Pre-Alloyed Fe	94.0 ± 0.6	4.2 ± 0.3	1.8 ± 0.5

7.4.2 *Ni Additions to PM2324*

Ni additions were found to have only a modest impact on the general sintering attributes of PM2324 regardless of the manner in which they were added (Table 18). In this regard, sintered densities for systems that included elemental or pre-alloyed Ni additions were only slightly lower (~1.0%) than those obtained for unmodified PM2324. The corresponding dimensional changes were also consistent with the degree of densification observed. Trends in general sintering data were also consistent with mechanical properties (Table 19), the material with pre-alloyed Ni exhibited very similar properties to the base alloy whereas elemental additions only invoked slight reductions in hardness, yield strength, and UTS. As such, pre-alloyed additions of Ni could be incorporated without any overtly adverse effects on sintering response or tensile behaviour. The same observation was also largely true with elemental Ni additions. Interestingly, the same dramatic reductions encountered when using elemental Fe additions were not observed. The reasoning for this effect is believed to be related to differences in the starting particle sizes of the Ni and Fe powders which prompted concomitant differences in the sintered microstructures. This concept is discussed in greater detail in the following paragraphs.

Table 18 - Nominal sintering response of PM2324 modified with 1 wt% Ni

	Density (%)		**Dimensional Change (%)**		
	Green	Sintered	OAL	Width	Length
Unmodified	***98.0*** *±0.1*	***98.7*** *±0.4*	***-2.07*** *±0.7*	***-1.67*** *±0.1*	***-1.24*** *±0.1*
Elemental Ni	**98.1** ±0.1	**97.9** ±0.1	**-1.50** ±1.0	**-1.30** ±0.2	**-1.04** ±0.1
Pre-Alloyed Ni	**97.9** ±0.1	**98.3** ±0.2	**-1.51** ±0.3	**-2.10** ±0.1	**-1.50** ±0.1

Table 19 - Mechanical properties of PM2324-T6 modified with 1 wt% Ni.

	Hardness (HRB)	E (GPa)	Yield Strength (MPa)	UTS (MPa)	Elongation (%)
Unmodified	***72*** *±2*	***69*** *±6*	***277*** *±12*	***295*** *±25*	***1.1*** *±0.5*
Elemental Ni	**70** ±2	**72** ±7	**264** ±26	**277** ±32	**0.8** ±0.1
Pre-Alloyed Ni	**74** ±1	**71** ±11	**285** ±20	**289** ±23	**0.7** ±0.2

SEM micrographs of the Ni-modified samples are displayed in Figure 50. Upon inspection of the specimens alloyed elementally it was clear that α-Al grains and a small fraction of residual porosity were present. The former were found to have a Cu content appreciably lower than that measured in the unmodified alloy (Table 20). A relatively coarse secondary feature was also observed. EDS analyses indicated that it was consistently enriched in Ni, Al, and Cu. Although a variety of bulk chemistries were measured, most were akin to that of Al_7Cu_4Ni. This particular phase has a wide range of permissible chemistries with Cu and Ni concentrations varying between 38.7-50.7 and 11.8-22.2 wt% respectively [68]. Accordingly, several stoichiometric compositions have been assigned to this phase including Al_6Cu_3Ni, Al_7Cu_4Ni, Al_3Cu_2Ni, Al_9Cu_3Ni and $Al_3(Cu,Ni)_2$. The only one of these phases that was confirmed via XRD was Al_7Cu_4Ni (Figure 51). As this phase has a higher Cu concentration than the aluminide phase noted in Fe-modified samples (Al_7Cu_2Fe) the reduced Cu content in α-Al grains seemed logical.

The microstructure of the pre-alloyed specimen (Figure 50(b)) was similar to the elemental counterpart and again Al_7Cu_4Ni was confirmed as the dominant intermetallic via XRD (Figure 51). Consistent with spectra gathered from Fe-modified samples (Figure 49), the θ phase was once again not detected via XRD. The one notable exception was a higher concentration of secondary phases within grains that were not directly adjacent to coarsened particles of Al_7Cu_4Ni. These were sub-micron particles with a cubic shape. While area scan EDS analyses confirmed the presence of Al, Cu, and Ni the specific analysis of individual particles was not possible due to their small size.

Given their location, reasonably homogenous distribution and the confirmed presence of Ni, these phases were most likely Ni-bearing intermetallics; presumably, Al_7Cu_4Ni. They resided in high concentrations within the grains simply as a result of pre-alloying coupled with the inward diffusion of Cu during sintering.

Overall, Ni additions were successfully incorporated by both means with minor impact on the PM processing response. Given the confirmed presence of Al_7Cu_4Ni in both samples, the formation of this phase would have acted to eventually lessen the amount of liquid phase present during sintering as noted in the prior discussion on Fe additions and the concomitant formation of Al_7Cu_2Fe. However, unlike elemental Fe additions, those of Ni did not invoke a significant loss in densification or mechanical properties. While it is postulated that similar mechanisms were operative, it is believed that the finer particle size of the Ni powder (D_{50} = 11μm) as compared to that of the Fe powder (D_{50} = 48μm) played a critical role. Here, the finer size of the Ni would have distributed the locations of direct contact between Ni and the Al-Cu-based liquid in a more homogenous manner. This would have then fostered a more homogenous distribution of the liquid phase that was able to persevere thereby allowing the system to then sinter in a reasonably homogenous manner as well.

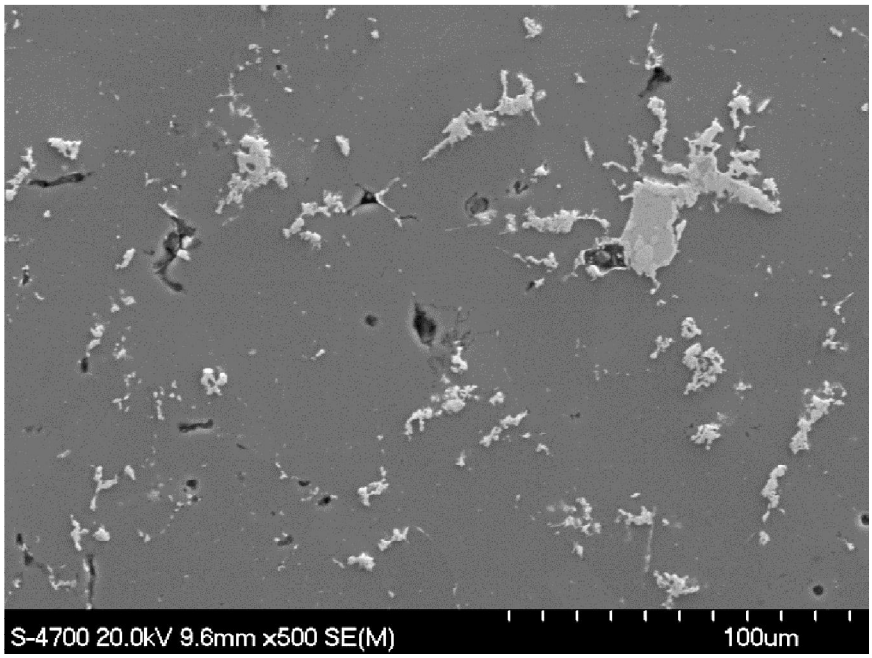

(a)

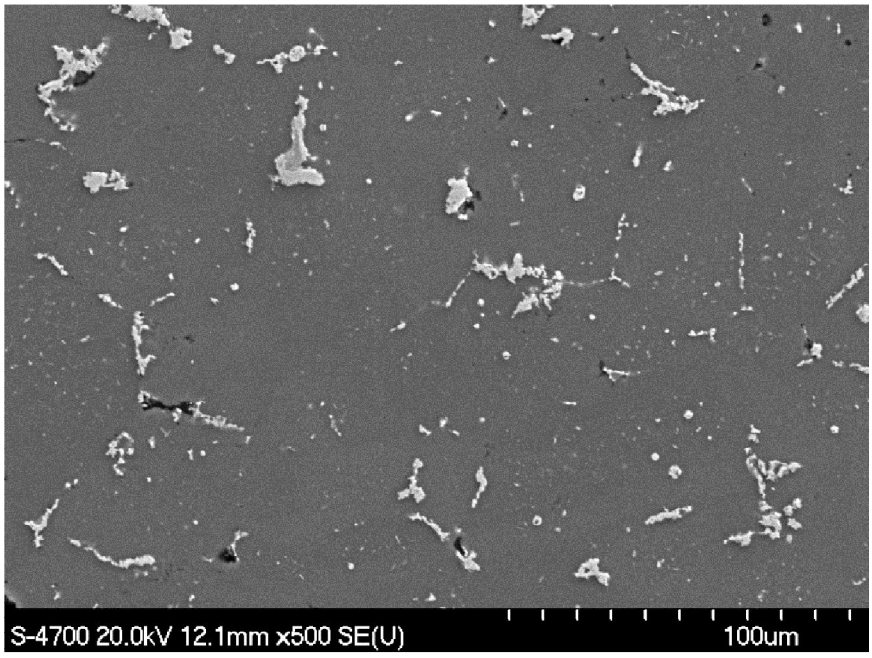

(b)

Figure 50 - SEM images taken of the polished (unetched) microstructure of PM2324-T6 modified with 1 wt% Ni as an (a) elemental and (b) pre-alloyed addition.

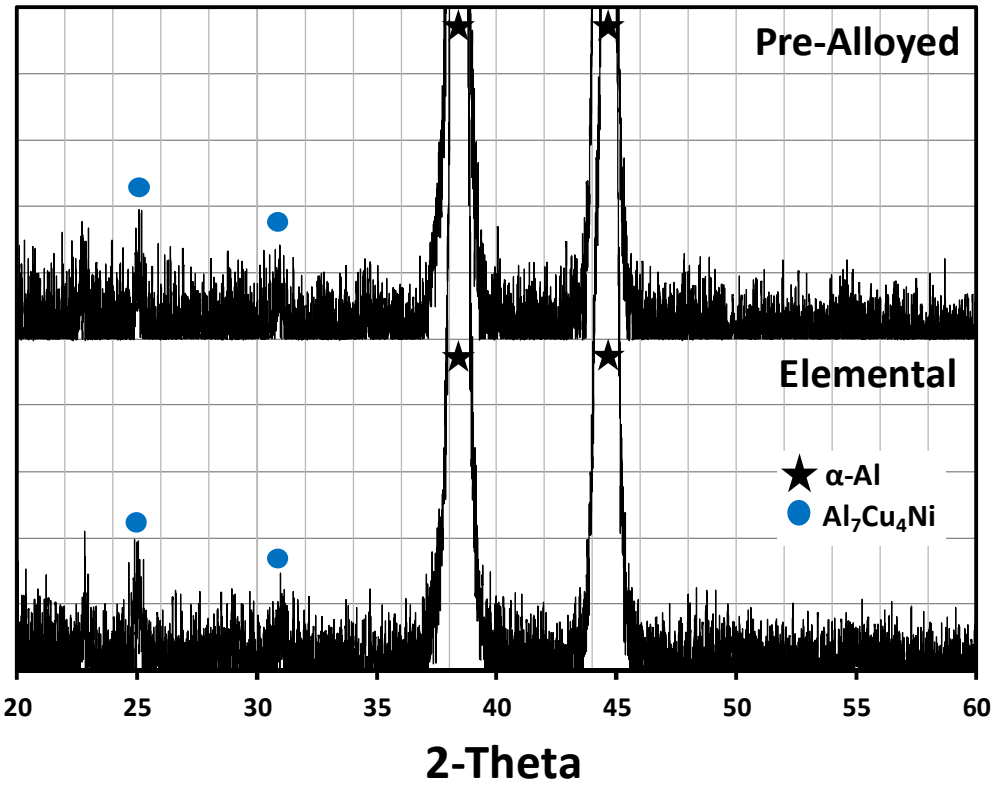

Figure 51 - XRD patterns recorded from PM2324-T6 modified with 1 wt% Ni as an elemental and pre-alloyed addition.

Table 20 - Mean chemistries of the α-Al grains in PM2324-T6 modified with 1 wt% Ni.

	Mean α-Al Composition (wt%)		
	Al	Cu	Mg
Unmodified	***94.2 ± 0.3***	***4.6 ± 0.2***	***1.2 ± 0.1***
Elemental Ni	95.7 ± 0.2	3.6 ± 0.1	0.7 ± 0.1
Pre-Alloyed Ni	94.4 ± 0.6	4.1 ± 0.3	1.5 ± 0.3

7.4.3 *Fe + Ni Additions to PM2324*

In the final phase of PM processing research the effects of simultaneously adding Fe and Ni were assessed. As shown in Table 21, the utilization of a pre-alloying approach to achieve these additions yielded specimens with the highest density of all combinations tested and was the first system to exceed the performance of the unmodified base alloy. These specimens also exhibited higher levels of shrinkage and tensile properties that slightly exceed those of the baseline system (Table 22). The specimens premised on elemental additions also yielded interesting results as the atomized Fe and carbonyl Ni appeared to have interacted in some way so to reduce the detrimental effects of the elemental Fe additions. In this sense, each physical and mechanical property of this alloy was intermediate between those created with singular Fe and Ni additions.

Microstructures of the specimens made with the combined additions are shown in Figure 52. A large fraction of secondary phases were observed within the α-Al matrices of both materials. These features were coarse and segregated when elemental additions were employed. A more uniform distribution existed in the pre-alloyed material. In this sample an abundance of small secondary phases existed within the grains along with localized coarsening. Interestingly, grains adjacent to the coarsest particles were generally depleted of the finer sized phase(s). This suggested that the small particles had locally coalesced during sintering as inspection of the internal microstructure of the raw powder did not reveal any signs of pre-existing chemical heterogeneities. XRD spectra (Figure 53) revealed that both alloys contained α-Al, Al_7Cu_2Fe, Al_7Cu_4Ni consistent with prior findings on singular additions of Fe (Figure 49) and Ni (Figure 51). However, in the pre-alloyed specimen the presence of the ternary phase Al_9FeNi was also confirmed. There were indications that this phase likely existed in the material made with elemental additions as well but the match was not as decisive. The existence of this feature is preferred in wrought Aluminum alloys designed for high temperature applications such as 2618 [44]. Key benefits of this particular phase include a high melting point and limited solubility for Cu; the latter allowing for the precipitation of a greater

concentration of Cu-bearing strengthening phases such as S and θ and the metastable variants thereof. In the case of PM processing, the low solubility of Cu would also impart a reduced tendency for liquid phase elimination and thereby offer benefits to sintering behavior as well. It appeared that this concept was indeed realized in the pre-alloyed specimens given that the data in Table 21 and Table 22 confirmed that it exhibited the most desirable sintering response of all the different formulations assessed. Accordingly, its formation was viewed as a favorable outcome.

It was also evident that the elemental sources had prompted the retention of a higher concentration of residual porosity albeit less severe than that observed in samples modified with elemental Fe alone (Figure 48(a)). This would indicate that the presence of Ni had in some way diminished the negative effects of elemental Fe, possibly as a result of forming the Al_9FeNi phase. EDS analyses (Table 23) implied that neither alloying method had imparted a significant difference in the average chemistries of the α-Al grains. In both scenarios a general reduction in the amount of Cu was observed.

Table 21 - Nominal sintering response of PM2324 modified with 1 wt% Fe + 1 wt% Ni.

	Density (%)		Dimensional Change (%)		
	Green	Sintered	OAL	Width	Length
Unmodified	***98.0*** *±0.1*	***98.7*** *±0.4*	***-2.07*** *±0.7*	***-1.67*** *±0.1*	***-1.24*** *±0.1*
Elemental Fe + Ni	**98.0** ±0.1	**97.3** ±0.1	**-0.68** ±0.2	**-1.27** ±0.1	**-0.98** ±0.1
Pre-Alloyed Fe + Ni	**97.1** ±0.1	**98.9** ±0.1	**-2.28** ±0.5	**-2.66** ±0.1	**-1.74** ±0.1

Table 22 - Mechanical properties PM2324 modified with 1 wt% Fe + 1 wt% Ni.

	Hardness (HRB)	E (GPa)	Yield Strength (MPa)	UTS (MPa)	Elongation (%)
Unmodified	***72*** *±2*	***69*** *±6*	***277*** *±12*	***295*** *±25*	***1.1*** *±0.5*
Elemental Fe + Ni	**69** ±2	**72** ±2	**231** ±4	**231** ±4	**0.4** ±0.1
Pre-Alloyed Fe + Ni	**71** ±1	**72** ±6	**292** ±3	**304** ±14	**0.8** ±0.2

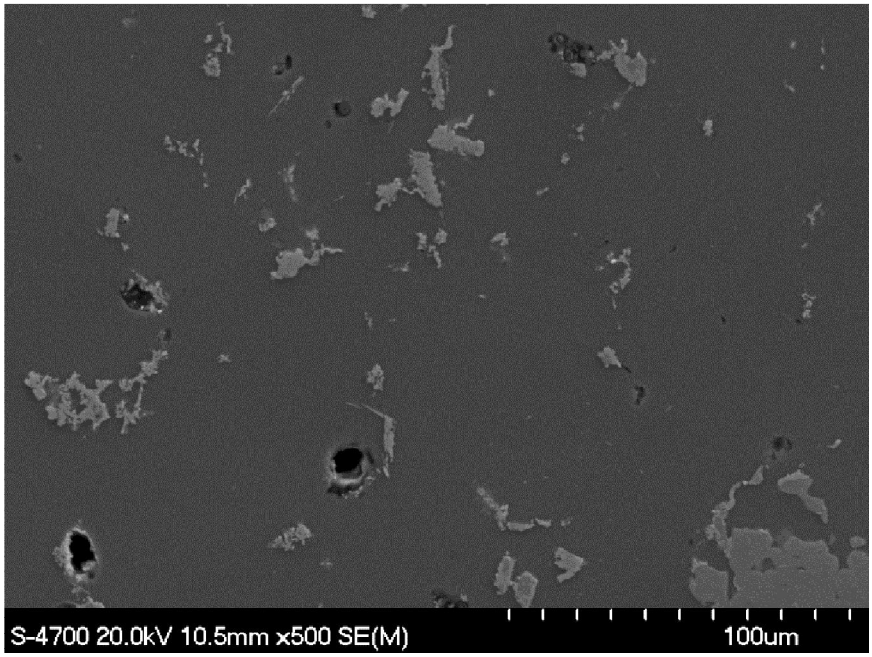

(a)

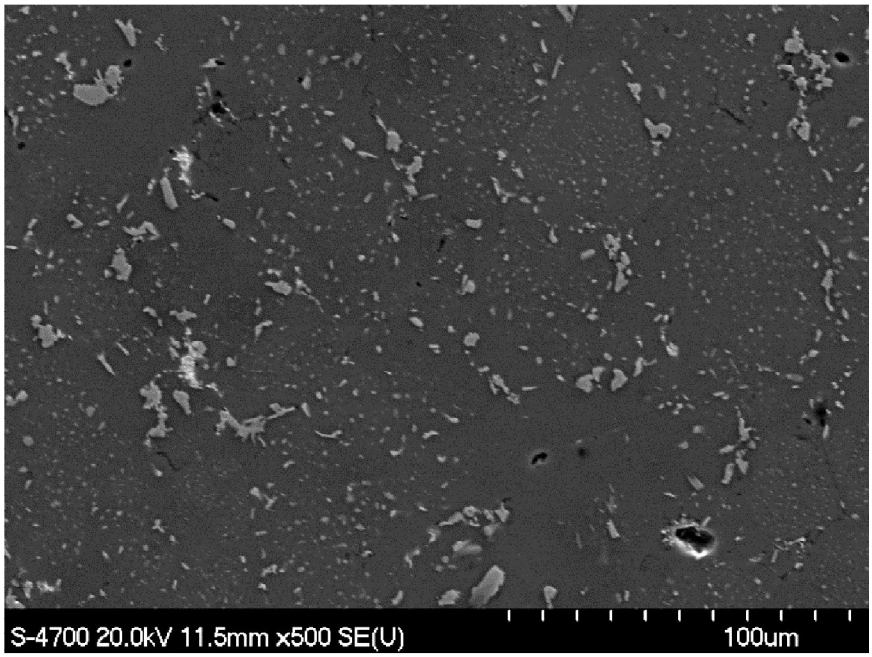

(b)

Figure 52 - SEM images taken of the polished (unetched) microstructure of PM2324-T6 modified with 1 wt% Fe + 1 wt% Ni as (a) elemental and (b) pre-alloyed additions.

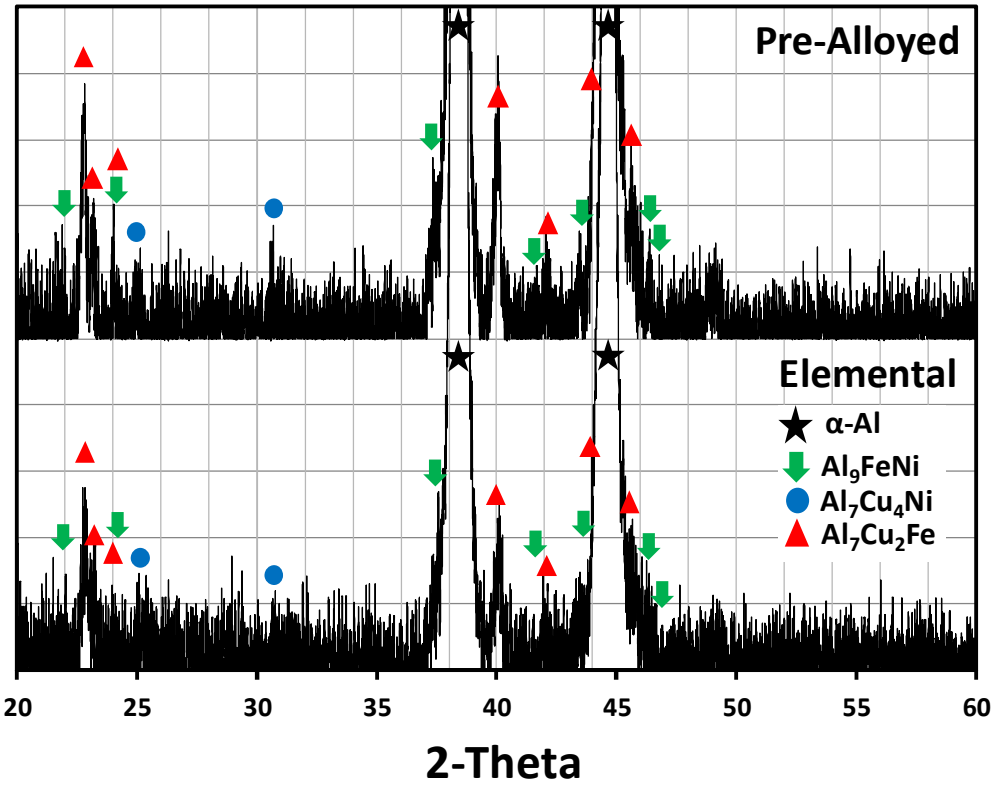

Figure 53 - XRD patterns recorded from samples of PM2324-T6 modified with 1 wt% Fe + 1 wt% Ni added as elemental and pre-alloyed additions.

Table 23 - Mean chemistries of the α-Al grains in PM2324-T6 modified with 1 wt% Fe + 1 wt% Ni

	Mean α-Al Composition (wt%)		
	Al	Cu	Mg
Unmodified	***94.2 ± 0.3***	***4.6 ± 0.2***	***1.2 ± 0.1***
Elemental Fe + Ni	94.8 ± 0.6	3.9 ± 0.2	1.3 ± 0.6
Pre-Alloyed Fe + Ni	94.4 ± 0.6	3.8 ± 0.4	1.7 ± 0.2

Of all the alloying combinations and methodologies assessed, the variant prepared with 1 wt% Fe + 1 wt% Ni through a pre-alloying approach exhibited the most promising response to PM processing. To gain a preliminary sense of the thermal stability of this alloy, machined tensile bars of it and the unmodified base alloy were subjected to an

isothermal hold at 160°C for 100h and tested. Data (Figure 54) revealed that the unmodified alloy experienced appreciable losses (~10%) in yield strength as a result of thermal exposure. A very different trend emerged for the modified alloy. Here, the yield strength was actually improved after thermal exposure. The former was rather surprising but was highly consistent with the behavior observed in wrought alloys such as 2618-T6 of comparable bulk chemistry [48]. These preliminary findings bode well for the modified alloy and suggested that meaningful advantages may exist. A detailed assessment of thermal exposure effects is currently the subject of a secondary study.

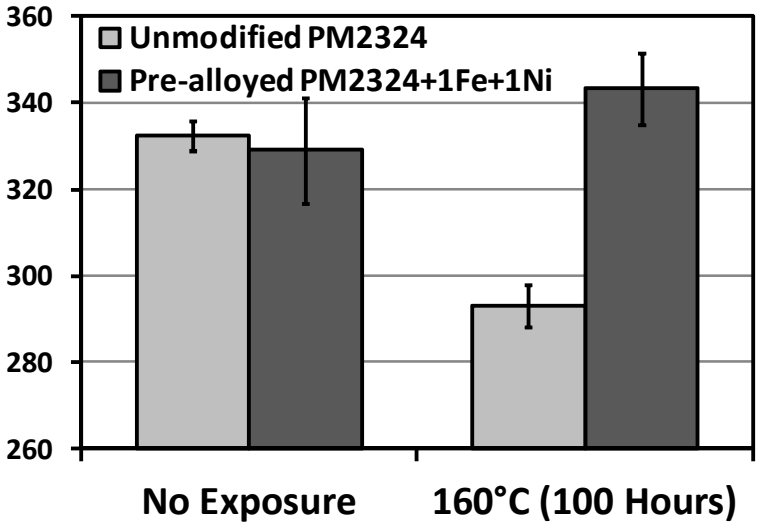

Figure 54 - Influence of 100h of thermal exposure at 160°C on the yield strength of unmodified PM2324-T6 versus that containing pre-alloyed additions of 1 wt% Fe + 1 wt% Ni.

7.5 Conclusions

1. Elemental Fe additions were significantly detrimental to the sintering response of PM2324, while pre-alloyed Fe additions resulted in a slight decrease in strength and a minor increase in ductility in the T6 condition. Once heat treated, PM2324 pre-alloyed with Fe exhibited overall good performance.
2. Elemental Ni additions appeared to have a negligible effect on the physical properties of PM2324 in the as-sintered conditions; however tensile testing revealed that it was slightly detrimental to the mechanical properties.
3. The combination of elemental Fe and Ni yielded properties intermediate between those achieved with individual additions.
4. In the as-sintered condition, all pre-alloyed additions resulted in a finely dispersed secondary phase within the α-Al grains, in addition to an observable amount of segregation of the Fe and Ni into the liquid phase. A slightly greater degree of porosity was also observed in pre-alloyed samples, relative to the unmodified PM2324.
5. Overall, pre-alloying increased the stiffness of PM2324; increasing the modulus while decreasing ductility. This is likely a result of the superior hardness of the dispersoid phases contributing to the overall elastic modulus of the alloy.
6. The absence of θ peaks in XRD spectra of all modified PM2324 alloys is most likely a result of the Al-Cu-(Fe,Ni) aluminides consuming the available Cu from the liquid phase (Al-Cu) and any θ formed within the α-Al grains.
7. Specimens of PM2324 pre-alloyed with Fe and Ni exhibited greater thermal stability under the limited conditions tested. This is a promising outcome that will be explored in greater detail in a secondary study.

Chapter 8 Development of an Al-Cu-Mg-(Fe)-(Ni) Powder Metallurgy Alloy – Part 2: Effects of Elevated Temperature Exposure

***Eric D. Moreau (Eric.Moreau@dal.ca)**
****I.W. Donaldson (Ian.donaldson@gknsintermetals.com)**
*****R.L. Hexemer Jr., (Rich.Hexemer@gknsintermetals.com)**
***D.P. Paul Bishop (Paul.Bishop@dal.ca)**

*Materials Engineering, Department of Process Engineering and Applied Sciences, Dalhousie University, 1360 Barrington St., Halifax, Nova Scotia, Canada
** GKN Sinter Metals, 3300 University Drive, Auburns Hills, Michigan, USA, 48326
*** GKN Sinter Metals, 407 Thornburg Drive, Conover, North Carolina, USA 28613

Status: **Submitted to the Canadian Metallurgical Quarterly**

Keywords: **Powder Metallurgy, Aluminum-Copper-Magnesium Alloys, DSC, SEM, XRD, Fe and Ni, Thermal Exposure**

The following experimental procedures, analysis and discussions were completed by E.D. Moreau, with reviewer and editorial roles played by the other authors.

Abstract

In a recent study, an appreciable increase in thermal stability was observed as a result of pre-alloying Fe and Ni with an emerging Al-Cu-Mg PM alloy. As such the present work consists of further, more thorough elevated temperature exposure characterization of the alloy, with and without Fe/Ni modifications. All powder compacts were sintered industrially where they displayed similar sintering response thereby confirming their commercial viability. Subsequently, tensile specimens machined from sintered charpy bars, followed by T6 heat treatment and thermal exposure were tested at room temperature. Each fractured specimen was examined via DSC, XRD and SEM, which confirmed that pre-alloying appeared to have slowed the aging/precipitation of the Al_2CuMg phase responsible for peak strengthening. The results indicated that pre-alloying yielded enhanced thermal stability over the unmodified alloy at lower temperatures (<160°C). At higher temperatures (>200°C) the presence of stable Fe/Ni dispersoids appear to be less effective, likely a consequence of the reduced dissolved Cu available for solid solution and precipitation strengthening.

8.1 Introduction

In recent years, the commercial use of Aluminum (Al) powder metallurgy (PM) technology within the automotive sector has risen significantly. Such growth has come as a result of several factors. These include desirable product economics, high efficiency of material usage, a minimized number of machining operations, and the widespread desire to utilize light-weight materials in vehicles [69]. The primary components fabricated with this technology are cam shaft bearing caps [70][71] while the commercial PM alloy known as AC2014 (Al-4.4Cu-0.6Mg-0.8Si) is the alloy most commonly utilized to fabricate these parts. Although this blend has proven adequate for this particular application, expansion of Al PM technology into more demanding scenarios requires the development of new blends that can provide gains in targeted areas of mechanical performance. Among these, alloys with improved stability during prolonged elevated temperature exposure represent a strategic area for research. In this regard, AC2014 is primarily strengthened by the precipitation of θ-type phases [72]. Such precipitates are known to be sensitive to elevated temperature exposure and coarsen at temperatures >100°C [27]. This effect causes a gradual decay in mechanical properties [56] that can present certain challenges when attempting to predict the long-term performance in a thermally active environment.

Thermally-induced strength reductions are common to many precipitation hardened Aluminum alloys regardless of their manner of processing (PM, wrought, cast, etc.). To combat this effect one common tactic is to add alloying elements that invoke a secondary strengthening mechanism that is less susceptible to thermal decay. Typically, this is achieved through some manner of dispersoid strengthening wherein a hard secondary phase is distributed within the material. For example, in wrought Al alloys such as 2618, an equal combination of Fe and Ni are added so as to form a stable dispersion of intermetallic phases (i.e. Al_9FeNi) that have a high melting point and thereby act to enhance elevated temperature properties of the alloy [44][48][57][58]. Given the success of this approach with wrought materials, it is presumed that similar gains could be realized using the same tactics in the development of new Al PM alloys. This concept

has been the focus of prior studies by the authors wherein the fundamental PM processing response of Al-Cu-Mg-(Fe-Ni) alloys has been assessed [59][73]. These works were largely centered on the development of a feasible means to incorporate the requisite transition metals into industrially feasible Al-Cu-Mg alloys [74][31] without compromising the compaction or sintering behaviour of the raw powder blend. It was determined that pre-alloying the Fe and Ni additions into the base Al powder was the most effective means of incorporation. Blends produced in this manner remained highly responsive to uni-axial die compaction, sintered to near full theoretical density and provided a refined distribution of Fe/Ni aluminide dispersoids in the sintered microstructure. With all questions on PM processing addressed, the objective of this paper was to study the influence of pre-alloyed Fe/Ni additions on the thermal stability of the sintered products. Here, test bars of an Al-4.4Cu-1.5Mg alloy (denoted as PM 2324) were prepared with and without pre-alloyed additions, subjected to differing combinations of thermal exposure times and temperatures and then assessed through a combination of tensile testing, XRD, DSC, and SEM analyses.

8.2 Materials

Two blends were processed in this study. One was a baseline PM2324 blend (hereafter referred to as "unmodified"). Here, elemental Al powder (air atomized; Ecka Granules) was blended with an Al-50%Cu master alloy, and elemental sources of Mg and Sn in the weight fractions needed to produce a final powder blend with a nominal composition of 4.4 wt % Cu, 1.5 wt % Mg and 0.2 wt % Sn (Al remainder). The second blend had the same nominal contents of Cu, Mg, and Sn sourced from the same raw powders utilized in the unmodified alloy. However, this particular formulation also contained Fe and Ni additions and was denoted as the "pre-alloyed" system. To achieve these additions, an Al powder that was pre-alloyed with 1wt% Fe + 1wt% Ni was used as the base powder in lieu of pure Al. This pre-alloyed powder was also produced by air atomization at Ecka Granules (Feurth, Germany). Accordingly, the bulk composition of the second alloy was Al-4.4Cu-1.5Mg-0.2Sn-1Fe-1Ni. Data on the particle sizes and chemical assays for all powders employed can be found in prior works [73]. An admixed ethylenebisstearamide

lubricant (Licowax™ C) was also added at a concentration of 1.5 wt% to both blends to facilitate die compaction.

8.3 Experimental Procedures

A PM processing sequence of powder blending, uni-axial die compaction, controlled atmosphere sintering, and T6 heat treatment was employed in the fabrication of test bars. Initially, raw blends of the unmodified and pre-alloyed alloys were prepared by blending the appropriate combinations of powders with a Turbula T2M mixer for 30 minutes. Powder compaction was then performed using a Satec® Systems model 200HVL load frame equipped with rigid floating die tooling assemblies for producing Charpy and transverse rupture strength (TRS) bars. In all instances load was applied at a rate of 2kN/s until the target pressure was achieved. The optimal compaction pressure for the unmodified alloy was found to be 400MPa in prior studies [31]. Hence, all specimens were compacted at this pressure. Sintering was performed under continuously flowing high purity (99.999%) nitrogen gas within an industrial continuous mesh-belt furnace. Targeted cycle parameters included 20 minute holds at 400°C for delubrication and at 600°C for sintering in accordance with the industrial thermal profile previously optimized for the unmodified alloy [32] All sintered products were heat treated to the T6 temper prior to testing. This process began by solutionization at 495 ± 2˚ C in air for 2 hours. Bars were then quenched in water and artificially aged to peak strength at 190 ± 2˚C for 10 hours. Preliminary characterization of the sintered specimens included the measurement of sintered density and apparent hardness. Sintered density measurements were made in accordance with MPIF standard 42 [63]. Here, bars were subjected to an Archimedes style of test using oil infiltration to seal the pores and prevent water ingression. Rockwell hardness measurements were made on the T6 bars per MPIF Standard 43 [64] using a Leco R600 Rockwell-hardness testing machine operated in the B (HRB) scale. Mean hardness measurements were calculated from a total of 8 indentations split evenly between the top and bottom surfaces of sintered TRS bars.

To assess the effects of thermal exposure, test bars were heated in air isothermally and isochronally. In the former, bars were held at temperatures of 120 and 280°C for times of 1, 10, 100, and 1000h. For the latter, specimens were held for a fixed period of 100h at temperatures of 120, 160, 200, 240, and 280°C. Thermally exposed specimens were then cooled to room temperature and subjected to a combination of tensile testing and microstructural assessments via differential scanning calorimetry (DSC), scanning electron microscopy (SEM), and x-ray diffraction (XRD). Tensile properties were assessed from machined Charpy bars (round threaded end specimens; gauge length = 25mm; gauge diameter = 6mm) in accordance with MPIF Standard 10 [65] using an Instron 200HVL frame equipped with a 50 kN load cell and an axial extensometer that remained attached to the specimen through to fracture. For DSC studies, a NETZSCH high temperature model 404 F3 Pegasus® DSC was used. Here, 22 mg (±1mg) disk-shaped specimens were machined from thermally treated TRS bars. Temperature and sensitivity calibration were achieved through repeated cyclic (heating-cooling) melting of a series of standards (Au, Bi, Al, etc.) in order to obtain mean melting point and enthalpy values. For each specific heating/cooling program used, the heat evolved between two empty Pt crucibles (with alumina inserts) positioned in the reference and specimen holder was recorded prior to the actual specimen analysis. During the tests themselves, samples were first placed in the alumina inserts within platinum crucibles. The apparatus was then purged using a mechanical pump until a suitable vacuum was obtained. The chamber was then backfilled with high purity argon gas. The purge/evacuate cycle was then repeated a second time after which a static flow of Ar was maintained (50ml/min). The temperature was then increased at a rate of 20K/min from ambient to 550°C followed by slow cooling to room temperature. Samples of high purity annealed Al (99.9999%) of the same shape were also prepared and tested in the DSC. The mass-normalized data from these runs were then subtracted from those acquired from the alloy specimen of interest to highlight the endothermic and exothermic peaks attributable to precipitation-based reactions. In SEM studies, specimens were cold mounted in epoxy resin under vacuum. Mounted samples were then ground using 240 grit SiC paper and rough polished with 9μm and 3μm diamond suspensions. Final polishing was completed with colloidal silica. All grinding and polishing processes were performed using a Buehler Vector® Power

Head auto-polisher. Finished samples were examined in the unetched condition using a Hitachi S-4700 field emission SEM operated with a 10 or 20 kV acceleration voltage and a beam current of 15μA. Finally, XRD was used to obtain qualitative analyses of the phases present. Sample preparation consisted of filing down fractured tensile bars using a bastard file then screening through a 325 mesh (45μm) screen. The samples were then loaded into a Bruker AXS D8 Advance XRD system equipped with a Copper K_α x-ray source operated at a tube voltage of 40 kV and tube current of 40 mA.

8.4 Results and Discussions

The results obtained though the course of this work were centered on the industrial processing response of the alloys in question coupled with elevated temperature exposure tests under isothermal and isochronal conditions. Data on each area of research are presented in the following sections.

8.4.1 *Industrial Processing Response*

All test bars employed in this work were sintered in an industrial setting. To ensure that these products were representative of the sinter quality that can be achieved in a laboratory environment [31][73] the sintered density, apparent hardness, and microstructures were assessed and compared. Sintered density and hardness measurements are given in Table 24. These data indicated that a highly comparable sintering response was observed at the two locations of interest. Both alloys achieved a high level of densification during sintering with finalized values that approached full theoretical limits. The sintered microstructures of the alloys are shown in Figure 55. Both images confirmed the high density achieved given the limited presence of residual porosity (black). The unmodified alloy contained grains of α-Al (dark grey) together with an intergranular distribution of bright secondary feature. Prior studies on this alloy have confirmed that the bright feature represents the solidified remnants of the persistent

liquid phase that was present during sintering and that it is primarily comprised of the θ ($CuAl_2$) phase [4][31][73]. The α-Al grains were dark grey and did not contain any secondary phases that were observable under the SEM imaging conditions employed. The most striking difference in the pre-alloyed material was the clear presence of a significantly higher concentration of secondary phases. Some of these features were located in intergranular regions consistent with the unmodified alloy. However, the majority were located within the α-Al grains themselves. These phases are known to be Al_9FeNi, Al_7Cu_2Fe and Al_7Cu_4Ni and stem directly from the use of the pre-alloyed Al powder [73]. These findings confirmed that a refined distribution of dispersoid strengthening features was achieved in the industrially sintered product consistent with lab data.

Table 24 - Comparison of the sintered density and apparent hardness of specimens sintered in an industrial furnace and in a laboratory setting.

Alloy	Sintering Location	Sintered Density (%)	Apparent Hardness (HRB)
Unmodified	Laboratory [73]	98.7 ± 0.35	72 ± 2.4
	Industry	99.0 ± 0.02	72 ± 3.8
Pre-Alloyed	Laboratory [73]	98.9 ± 0.06	71 ± 1.1
	Industry	98.9 ± 0.06	69 ± 1.6

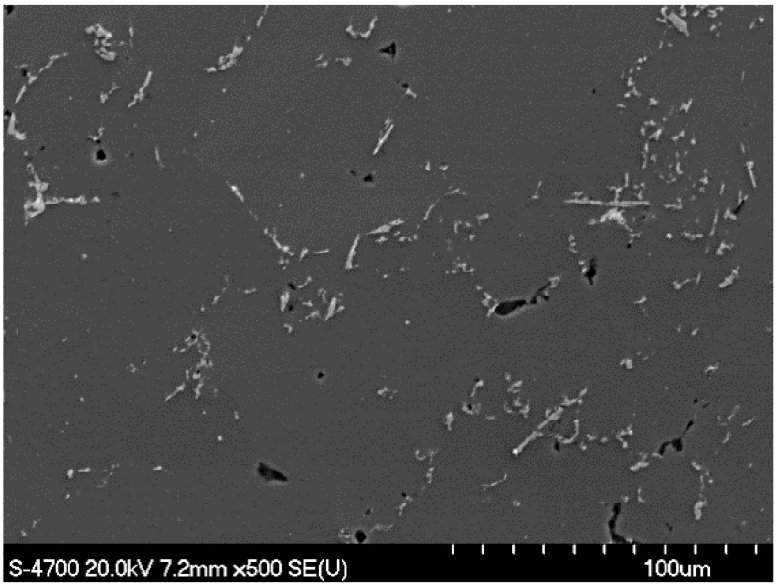

(a)

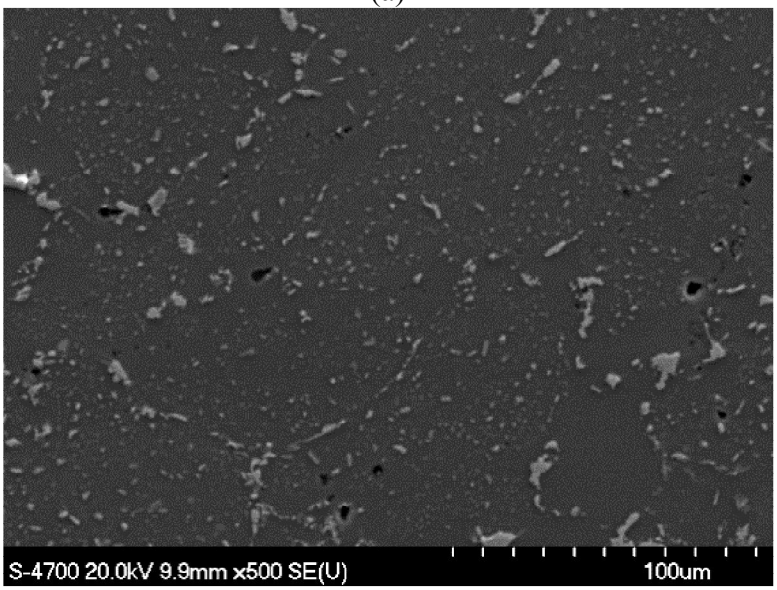

(b)

Figure 55 - Microstructures observed in the (a) unmodified and (b) pre-alloyed materials sintered in an industrial setting.

In the next stage of research, DSC analyses were completed on the industrially sintered alloys following heat treatment to the T6 condition. DSC is a technique that is frequently employed to assess the type and nature of any precipitate phases present in heat treated Aluminum alloys [75]. Furthermore, as the alloys in question contain Cu and Mg for precipitation hardening in a 3:1 ratio, peaks in the heat flow traces are most likely associated with transitions in metastable variants of the S (Al_2CuMg) and/or θ ($CuAl_2$)

precipitates [76]. The Fe/Ni bearing dispersoid phases are not expected to directly contribute any discrete endothermic/exothermic peaks given their known stability over the temperature range of interest and the lack of any metastable precursory phases [57]. It is therefore necessary to understand the nature of S phase precipitation, as it provides a basis for the observed results. Within this field of study considerable disagreement exists. Indeed, several different models have been proposed to explain the general precipitation sequence of the S phase in Al-Cu-Mg alloys. However, due to the lack of evidence for the existence of GPB zones (precursor to GPBII/S″) and increasing acceptance that S′ and S possess identical lattice structures with the exception of minor variations in their lattice parameters [77][78][79], the following sequence (equation 12) proposed by Perlitz and Westgren seems to have become that most widely accepted in Al-Cu-Mg alloys that are not cold worked prior to heat treatment [80]:

$$SSSS \rightarrow Cu/Mg\ co\text{-}clusters \rightarrow GPBII/S'' \rightarrow S\ (Al_2CuMg) \qquad \textbf{Equation 12}$$

According to this model, the precipitation sequence begins with a super saturated solid solution (SSS) decomposing as Cu and Mg segregate in coherent clusters with no discernible structure. Upon further aging the growing Cu/Mg clusters eventually arrange themselves into an orthorhombic structure denoted as GPBII zones or S″ while maintaining their coherency with the FCC α-Al matrix. Further aging then follows with the precipitation of incoherent equilibrium phase S.

DSC measurements obtained from the alloys studied in the T6 condition are shown in Figure 56. From these data four major effects were identified in the unmodified alloy and are labelled as A, B, C, and D. Counterpart heat flows labeled with a prime (i.e. A′) denote artefacts observed in the pre-alloyed specimen. The first peak observed (A/A′) was one of an endothermic character and occurred between 205-290°C. This peak was believed to be due to the dissolution of Cu-Mg co-clusters and potentially some S″ [20-22] which was expected as all specimens were evaluated in the T6 condition (peak strengthened) and therefore likely contained a high concentration of both phases [79]. The next peak (B/B′) was exothermic in nature and has been reported by several authors

as the precipitation of the incoherent equilibrium S phase [77][78][79][81][82]. This exothermic effect most likely corresponded to the formation of this same phase. It is noted that a discrete peak associated with S′ formation was not observed. This was in agreement with literature data as this event is known to occur at lower temperatures in samples that are cold worked prior to aging [78][79]. The broad peak labelled C/C′ is typically referred to as the "dissolution trough". Accordingly, it was associated with the dissolution of the S precipitates into solid solution within the α-Al grains. The final heat effect was a sharp peak that occurred at a temperature of 518°C (labeled as peak D). Given that this peak was of an endothermic character and that it occurred at temperatures well beyond that range associated with S-based precipitation reactions, it was speculated that a melting event was responsible for its occurrence. This notion was supported by DSC work completed by Wang et al [77] on wrought 2024 and 2324 (Al-4.4Cu-1.5Mg-0.6Mn) both of which possess chemistries very similar to that of the unmodified alloy of this report. In their work, a similar endothermic peak occurred between 505-515°C under a slower heating rate of 10 K/min and was ascribed to incipient melting of a Al_2Cu (θ) based eutectic. This effect is also in agreement with the ternary Al-Cu-Mg phase diagrams whereby the formation of liquid appears to begin at ~ 500°C [83]. Interestingly, this peak was consistently absent in all traces acquired from pre-alloyed specimens. This was believed to be a result of the essential elimination of θ-based eutectic within the pre-alloyed material as detailed in prior works [73]. Comparing the DSC results of both alloys (Figure 56) it is clear that peaks A′ and B′ have shifted toward higher temperatures as a result of pre-alloying, which could be indicative of enhanced thermal stability. Consequently the dissolution peak (C) appears to have also broadened to encompass a range of 300 to 465°C in comparison to C′ which occurs from 355 to 465°C.

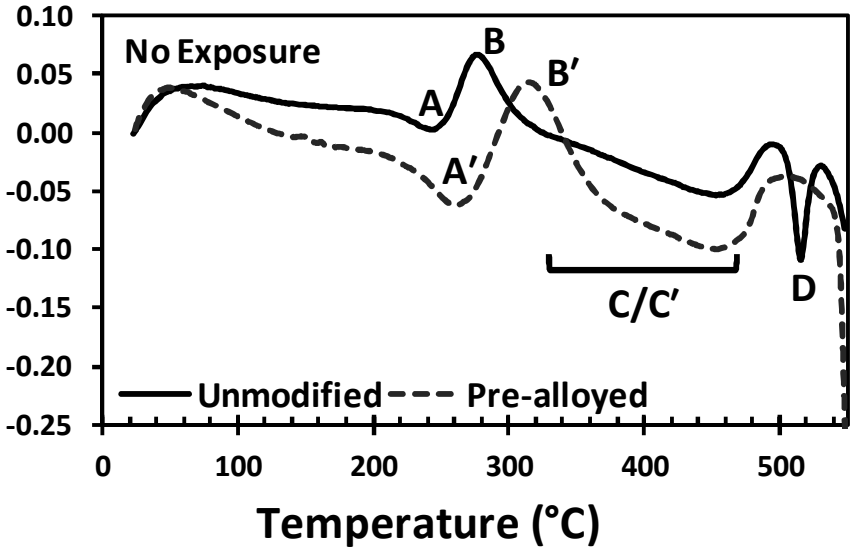

Figure 56 - DSC traces acquired from specimens in the T6 condition. All specimens scanned at a rate of 20K/min.

XRD spectra acquired from the same alloys examined via DSC are shown in Figure 57. From these traces it was clear that the unmodified alloy primarily contained α-Al, equilibrium θ, and likely some equilibrium S phase as well. Comparatively, pre-alloyed alloys contained α-Al, Al_7Cu_2Fe, Al_7Cu_4Ni, and to some extent Al_9FeNi phases. All of the three intermetallic species have been observed in similar 2024-type alloys when combined with Fe and Ni [57][58]. Furthermore, equilibrium variants of θ or S phases were not detected in the pre-alloyed material. This observation was in agreement with DSC data in that the θ-based eutectic melting event (peak D) was observed in the unmodified alloy but not in the pre-alloyed specimen. Although DSC data (Figure 56) implied that Cu-Mg co-clusters and/or some GPBII/S″ were present in alloys these were not detected via discrete peaks within the XRD spectra. The inability to detect these phases was a result of their full coherency within the FCC α-Al lattice [81][82]. Such coherency would not provide a suitable ddiffraction interface and thereby prevent the development of discrete peaks associated with any of these non-equilibrium phases from the S-based precipitation sequence.

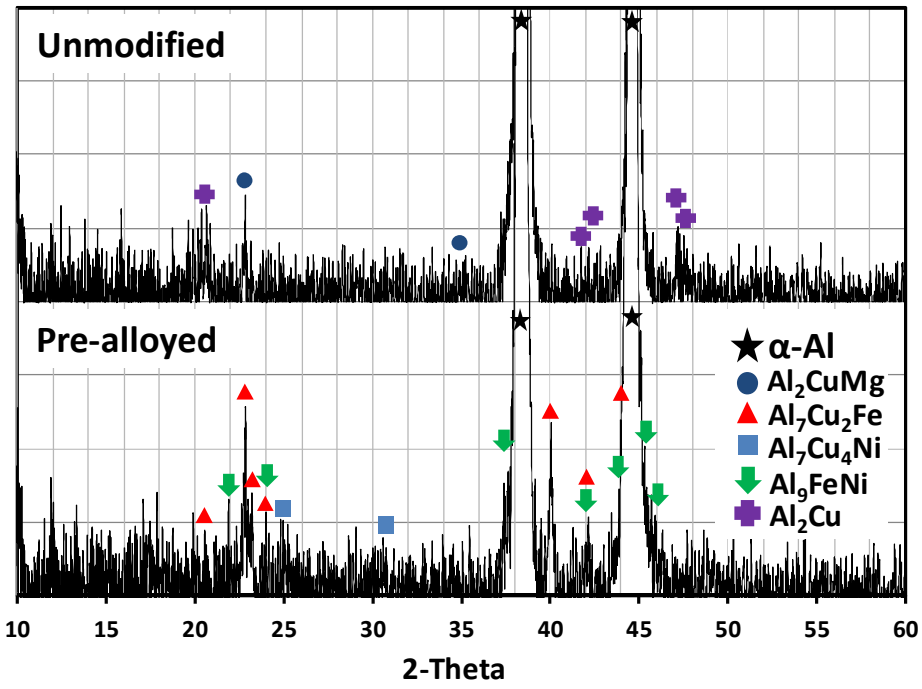

Figure 57 - XRD spectra acquired from samples of the unmodified and pre-alloyed alloys in the T6 condition.

8.4.2 *Isothermal Exposure Tests*

With the industrial sintering process validated, research then shifted to thermal exposure trials. Tensile results for the alloys subjected to isothermal exposure at 120ºC and 280ºC are shown in Figure 58 and Figure 59, respectively. At the lower temperature of 120°C the effects were largely negligible. Both alloys maintained comparable performance for all of the exposure times assessed and showed no signs of significant degradation in yield strength, UTS, or ductility. Pre-alloyed specimens however, repeatedly displayed overall lower ductility in comparison to the unmodified variant.

In samples exposed at 280ºC (Figure 59) it was clear that the yield strength and UTS of both alloys declined appreciably with increasing exposure time. These trends were offset by progressive increases in ductility as would be expected. Based on these results it was concluded that pre-alloying was ineffective at preventing a loss in tensile properties at this high temperature.

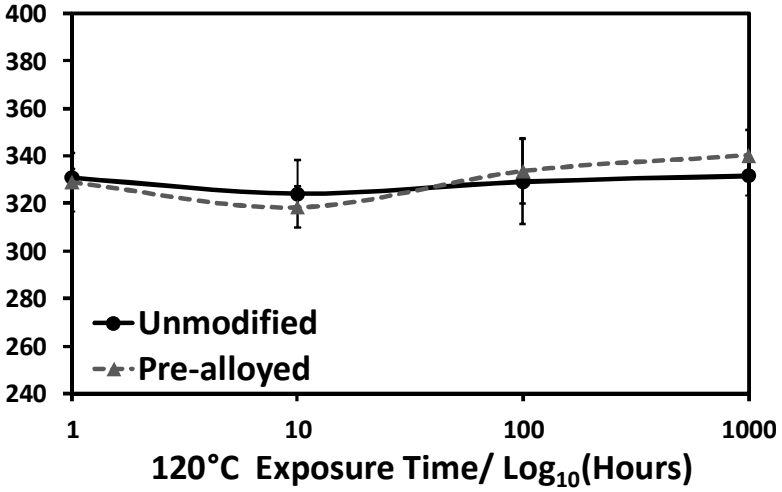

(a)

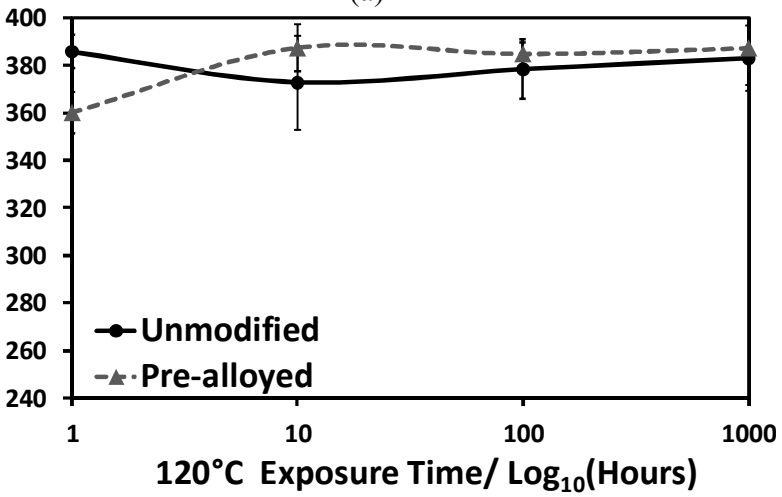

(b)

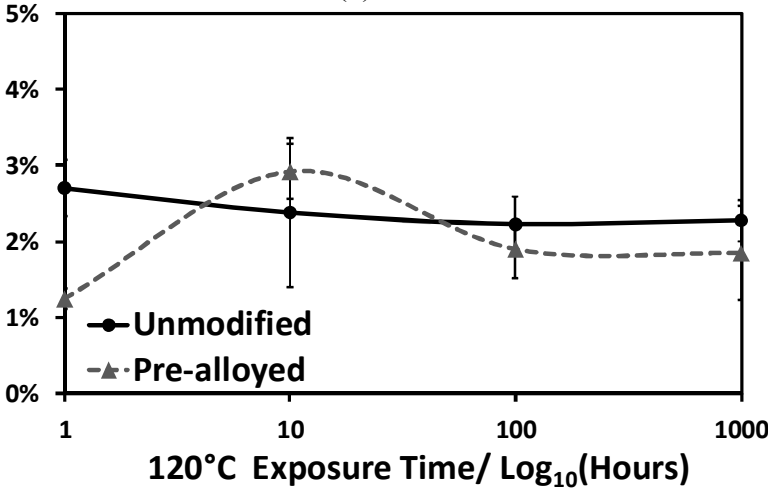

(c)

Figure 58 - Variations in the tensile properties as a result of isothermal exposure at 120°C. Data shown for transitions in (a) yield strength, (b) UTS, and (c) ductility. All specimens tested at room temperature.

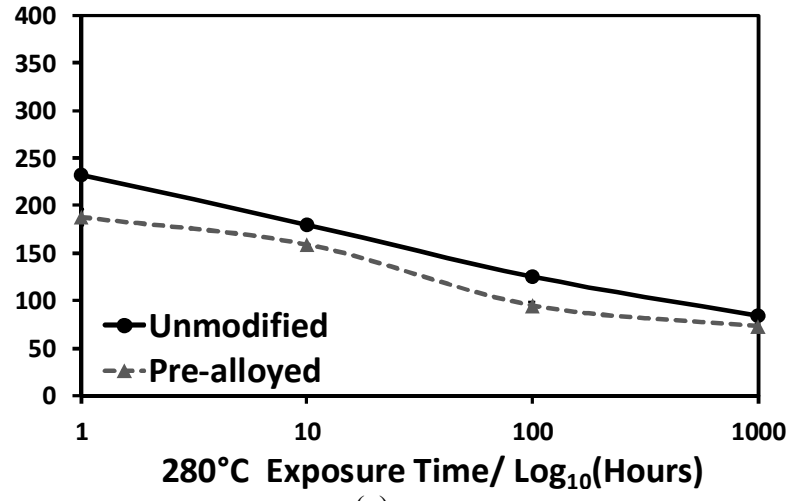

(a)

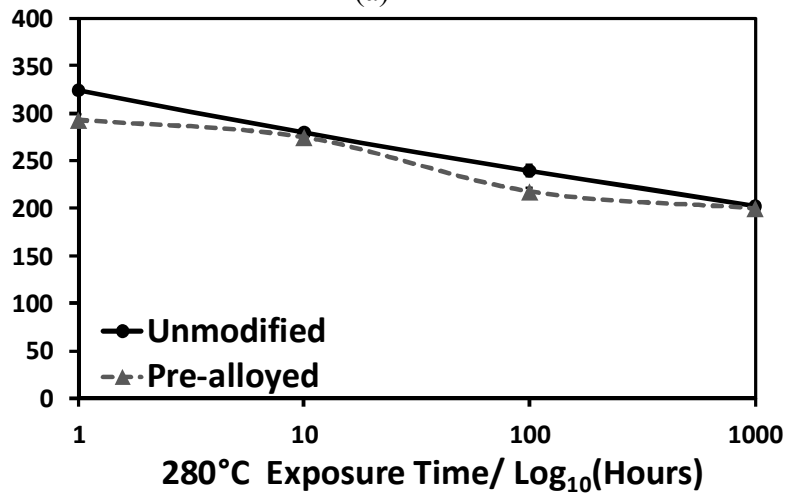

(b)

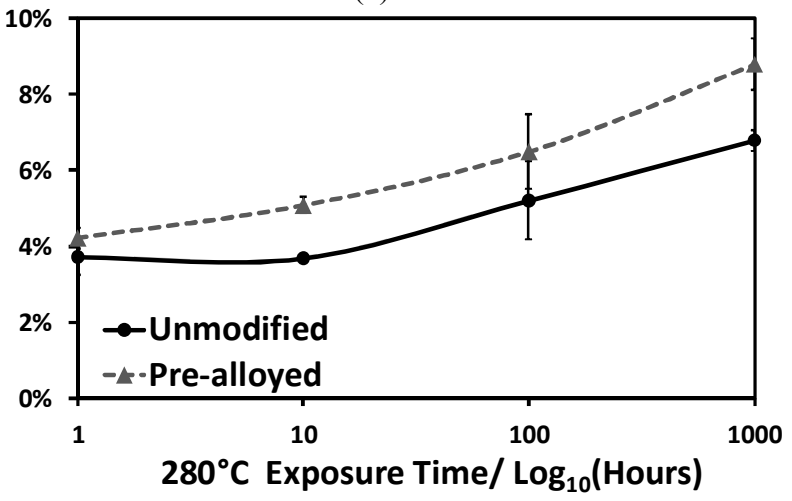

(c)

Figure 59 - Variations in the tensile properties as a result of isothermal exposure at 280°C. Data shown for transitions in (a) yield strength, (b) UTS, and (c) ductility. All specimens tested at room temperature.

A comparison of the DSC traces acquired from the alloys treated for 1000 hours at 120°C is shown in Figure 60, while those subject to the higher temperature of 280°C are displayed in Figure 63. At lower exposure temperature (120°C) the peaks for co-cluster/S″ dissolution (A) and the subsequent precipitation of S (B) were notably smaller in the trace for the unmodified alloy as compared to those observed in the same alloy prior to thermal exposure (Figure 56). Conversely, the same peaks in the pre-alloyed material (A′/B′) were largely unaffected by the 120°C exposure having maintained a comparable size to those recorded from the starting material (Figure 56). The relative size of a DSC peak is directly related to the amount of precipitates that are transforming during the particular event in question. Accordingly, this allows one to infer that the precipitates in the unmodified alloy had over-aged during the 120°C exposure with some having matured into the equilibrium variant of the S phase prior to testing in the DSC. Those present in the pre-alloyed material were more resilient towards this effect. At higher exposure temperatures (280°C) both alloys showed no evidence co-cluster/S″ dissolution (A/A′) or S precipitation (B/B′). This implied that both alloys were heavily over aged. Peak D was consistently observed in the unmodified samples alone and did not appear to vary appreciably in magnitude or temperature as a result of any of the thermal exposure conditions assessed. This indicated that the eutectic θ-based phase was unaffected by thermal exposure. It also confirmed that this phase was not developed within the pre-alloyed material despite the extensive level of over aging that had transpired.

XRD spectra from unmodified and pre-alloyed specimens subjected to 1000h of exposure at 120°C and 280°C are shown in Figure 62 and Figure 63, respectively. Relative to the starting materials (Figure 57), it was again noted that the Fe/Ni aluminides were only present in the pre-alloyed material while θ existed exclusively in the unmodified alloy. Despite these consistencies, differences were noted in the ability to detect the equilibrium variant of the S phase. In this sense, this phase was readily detected in both alloys when thermally exposed at 280°C for 1000h. However, it was only detected (albeit to a lesser extent) in the unmodified alloy when the samples that were treated for the same length of time at 120°C were assessed. These observations were consistent with DSC findings. In

this sense, the DSC data of Figure 61 confirmed that the precipitates within both alloys had fully over aged to the point of forming the equilibrium variant of the S phase after the 280°C exposure. However, traces from the 120°C exposed specimens indicated that partial over aging had only transpired in the unmodified alloy while precipitates within the pre-alloyed sample were largely unaffected. Under these conditions, a fraction of precipitates within the unmodified alloy alone would have matured into the equilibrium state thereby enabling their detection via XRD.

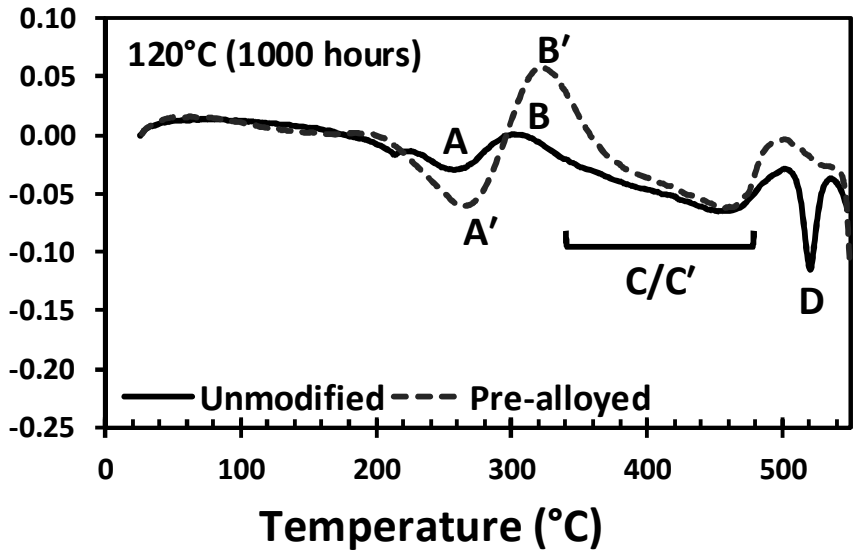

Figure 60 - DSC traces acquired from specimens subjected to 1000h of thermal exposure at 120°C. All specimens scanned at a rate of 20°C/min.

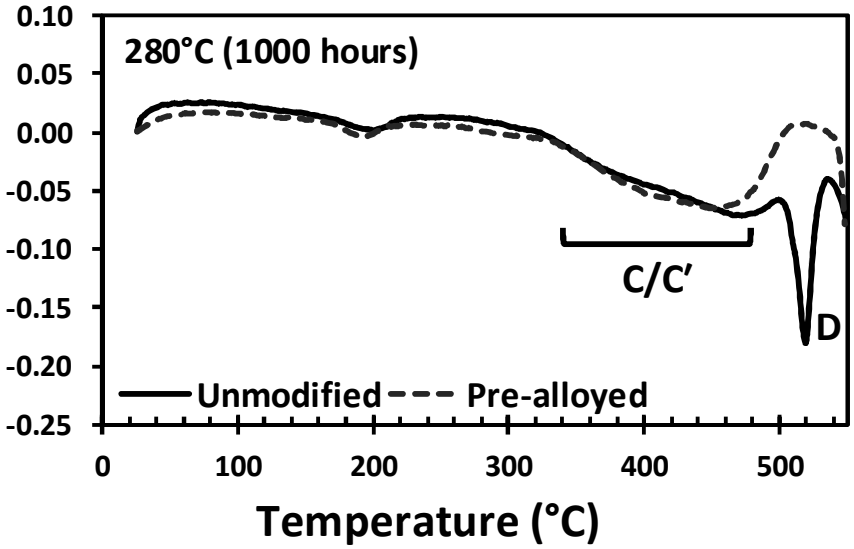

Figure 61 - DSC traces acquired from specimens subjected to 1000h of thermal exposure at 280°C. All specimens scanned at a rate of 20°C/min.

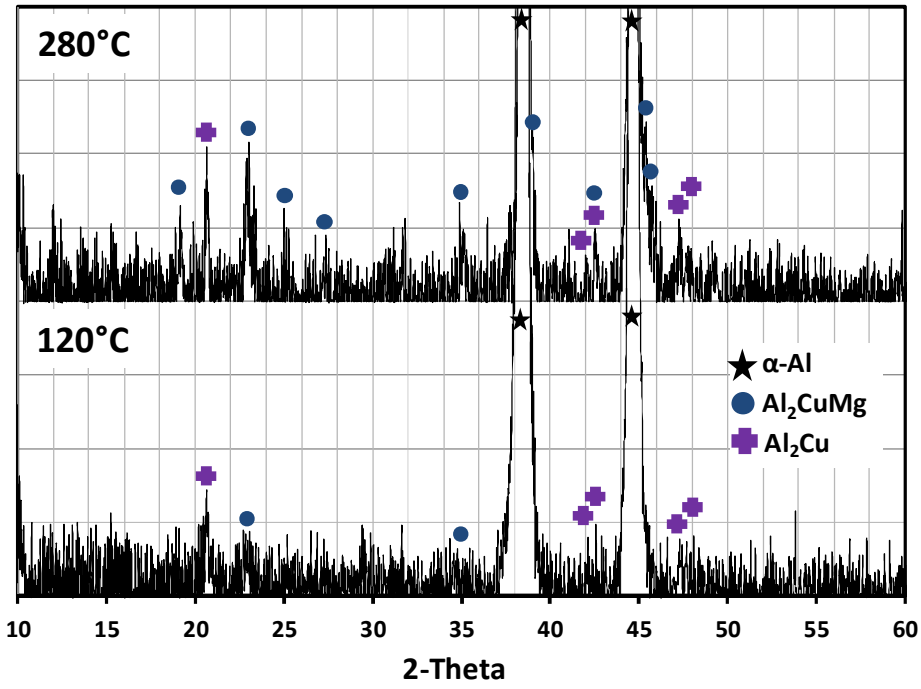

Figure 62 - XRD spectra acquired from samples of the unmodified alloy following 1000 hours of thermal exposure at to 120°C and 280°C.

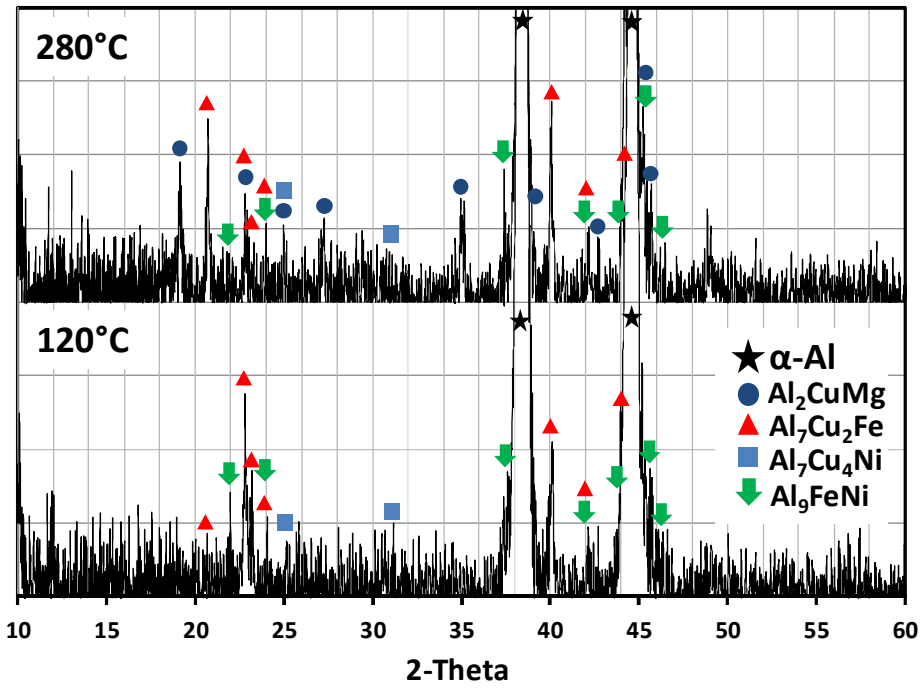

Figure 63 - XRD spectra acquired from pre-alloyed samples following 1000 hours of thermal exposure at to 120°C and 280°C.

SEM images taken of the 4 samples assessed via DSC and XRD (120ºC and 280ºC for 1000 h) are shown in Figure 64 and Figure 65, respectively. The SEM-observed microstructures for the 120ºC specimens were similar to those of the starting materials prior to thermal exposure (Figure 55). Most notably, the α-Al grains still appeared to be largely featureless and there were no obvious signs of precipitate formation as detectable via SEM imaging. This differed substantially from the images of the 280ºC specimens. Here, regular arrays of what appeared to be lathe-like precipitates were now clearly present in the grains of both alloys. Due to the size and shape of the precipitates it was impossible to acquire any meaningful EDS chemical assays of the precipitates. However, the apparent habitual crystallographic arrangement of the lathes would be typical of S precipitates as observed by others via the preferred technique of transmission electron microscopy [80].

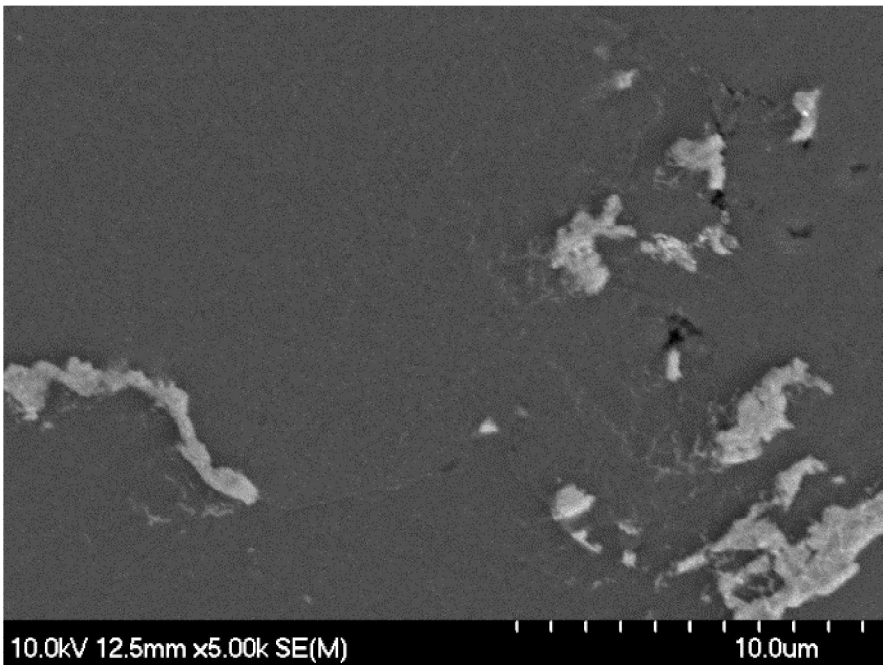

(a)

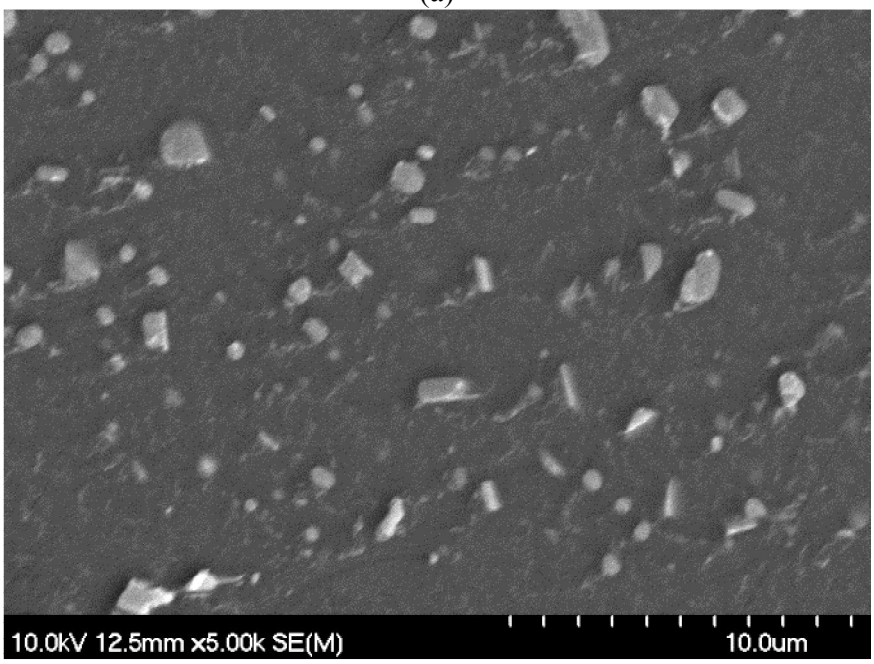

(b)

Figure 64 - SEM images of the microstructures observed in samples thermally exposed at 120°C for 1000h. (a) Unmodified alloy and (b) Pre-alloyed alloy.

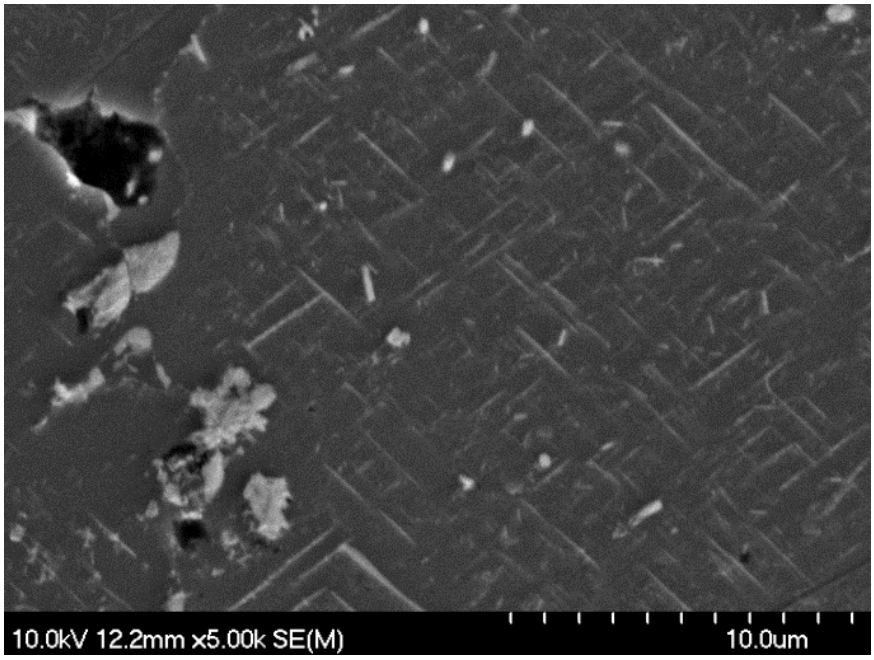

(a)

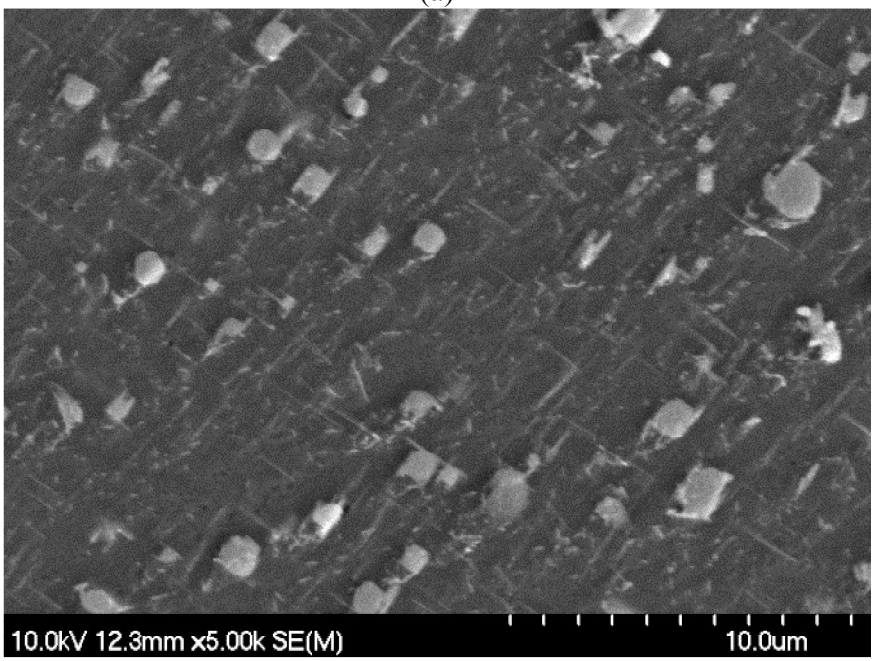

(b)

Figure 65 - SEM images of the microstructures observed in samples thermally exposed at 280°C for 1000h. (a) Unmodified alloy and (b) Pre-alloyed alloy.

8.4.3 *Isochronal Exposure Tests*

In the next phase of research, isochronal (100 hour) elevated temperature exposure tests were performed as a means to further understand the behaviour of the PM alloys when subjected to thermal exposure. Tensile results for the isochronal tests are displayed in Figure 66. As previously noted in 120ºC isothermal tests the mechanical performance of both alloys was essentially identical and remained unchanged at temperatures ≤120ºC. After exposure to temperatures ≥160ºC, the yield strength and UTS of the unmodified alloy fell into a steady downward trend with the progressive loss in strength increasing with rising exposure temperature. This differed from the trend noted in the pre-alloyed samples. Here, the region of relatively static mechanical performance was extended out to include 160°C wherein a subtle improvement in yield strength was actually observed before the downward trend then commenced. This was consistent with the trend in tensile ductility in that the value of this property fell slightly at 160°C. These observations suggested that some form of secondary age hardening had occurred in the pre-alloyed material. Interestingly, the same phenomenon is also observed in Fe/Ni dispersion strengthened wrought alloys such as 2618 [48].

In an effort to understand the metallurgical transitions that may have been responsible for the observed trends in tensile properties, DSC tests were completed on specimens extracted from the threaded end segments of fractured tensile bars. The resultant heat flow curves acquired from the specimens isochronally treated at 120ºC are shown in Figure 67. These traces were very similar to those acquired from the alloys prior to thermal exposure (Figure 56). In this sense, strong signals for all of the initially noted peaks (A-D; A′-C′) remained present and those derived from the pre-alloyed material were again shifted to higher temperatures. These results implied that the precipitates were largely unaffected by the 100h exposure at 120ºC consistent with tensile data (Figure 66). DSC data from the alloys treated at 160ºC (Figure 68) revealed several key differences. First was the fact that peaks A/B from the unmodified alloy were now indiscernible in the heat flow trace. This implied that appreciable over aging had transpired and that precipitates had largely advanced into a condition of the equilibrium variant of the S phase. This correlated well with tensile data (Figure 66) as the

downward loss of strength had commenced under this isochronal exposure condition. Interestingly, peaks A′/B′ were still observed in DSC data for the pre-alloyed material. This implied that many precipitates within this alloy were still in the form of Cu-Mg co-clusters and S″ and that complete evolution into the equilibrium S phase had not transpired in this material. It is these types of precipitates that invoke the greatest strengthening effect. Hence, their preservation throughout the 160ºC exposure would justify the observed ability of this alloy to maintain its yield strength under these more demanding conditions. After the next incrementally higher exposure temperature (200ºC) peaks A/B and A′/B′ were no longer present in either of the DSC traces (Figure 69). This implied that significant over aging had occurred in both materials with precipitates having universally evolved into the equilibrium S phase. The DSC traces recorded from samples isochronally exposed at 240 and 280ºC were essentially identical to those shown in Figure 69. This was as expected given that no further crystallographic transitions in the precipitates would have transpired. Hence, it is inferred that the steady loss in strength that occurred in both materials over the temperature range of 200-280ºC was largely attributable to progressively greater extents of S phase coarsening.

The improved thermal stability of the precipitates within the pre-alloyed material was also apparent when transitions in the peak temperatures associated with events A/A′ and B/B′ were compared. These findings are summarized in Table 25. In the unmodified alloy, both peaks shifted to higher temperatures as the exposure temperature was raised and eventually disappeared at exposure temperatures ≥160ºC. This implied that these precipitates were prone to gradual crystallographic evolution over all of the conditions considered and that they exhibited minimal resistance to this effect. Conversely, the counterpart peaks from the pre-alloyed material occurred at temperatures that were typically 10-20ºC higher. Their temperatures of occurrence were also effectively static and did not shift to any appreciable extent during exposure at 120 or 160ºC. These findings further confirmed that a greater heat input was needed to cause precipitates in the pre-alloyed material to advance into the equilibrium S phase condition.

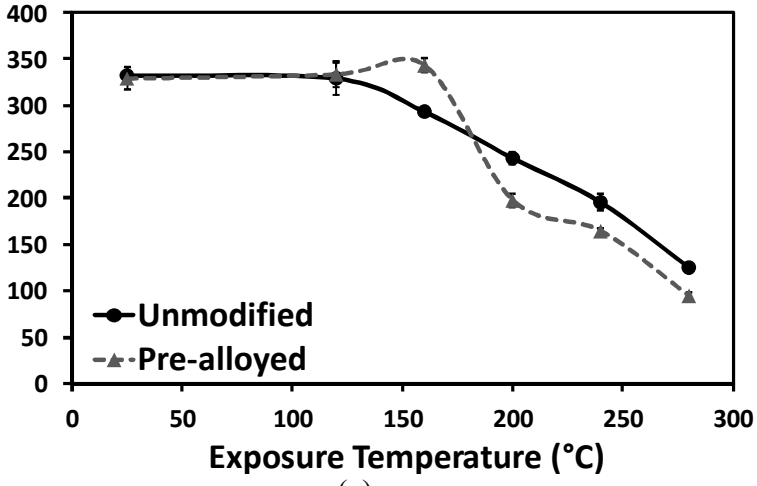

(a)

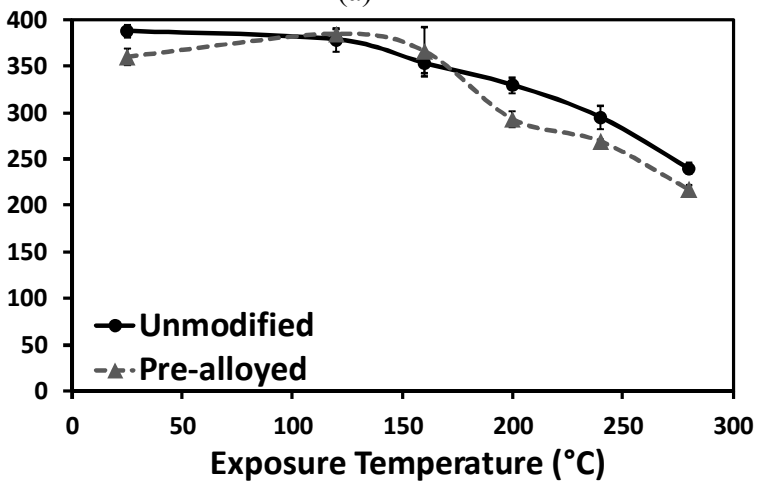

(b)

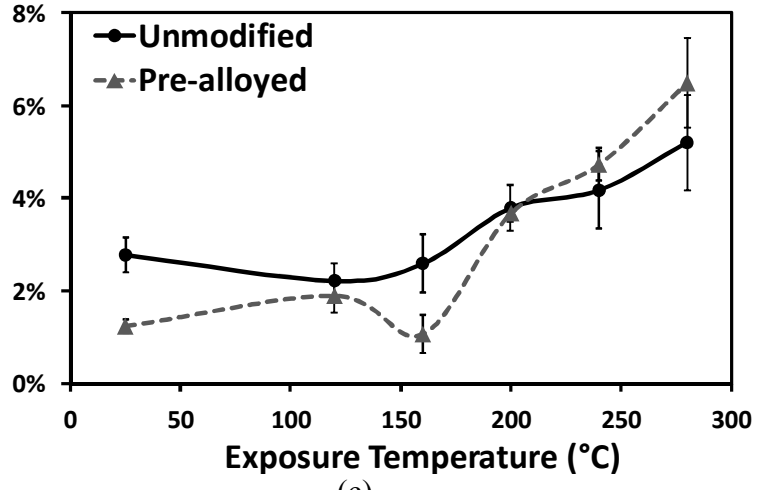

(c)

Figure 66 - Effects of thermal exposure temperature on the tensile properties of unmodified and pre-alloyed materials. (a) Yield strength, (b) UTS, and (c) ductility. All specimens held for 100 h at the temperatures indicated.

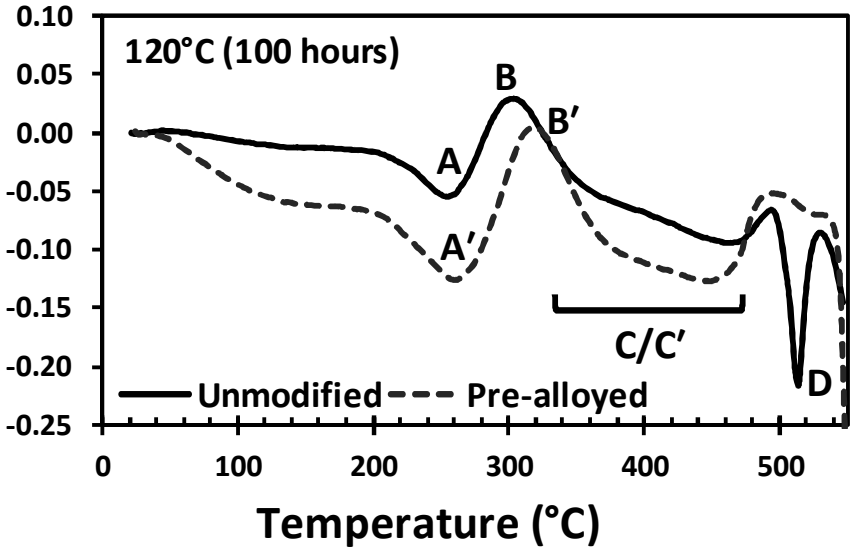

Figure 67 - DSC traces of unmodified and pre-alloyed alloys subject to 120°C for 100 h. Scan rate = 20°C/min.

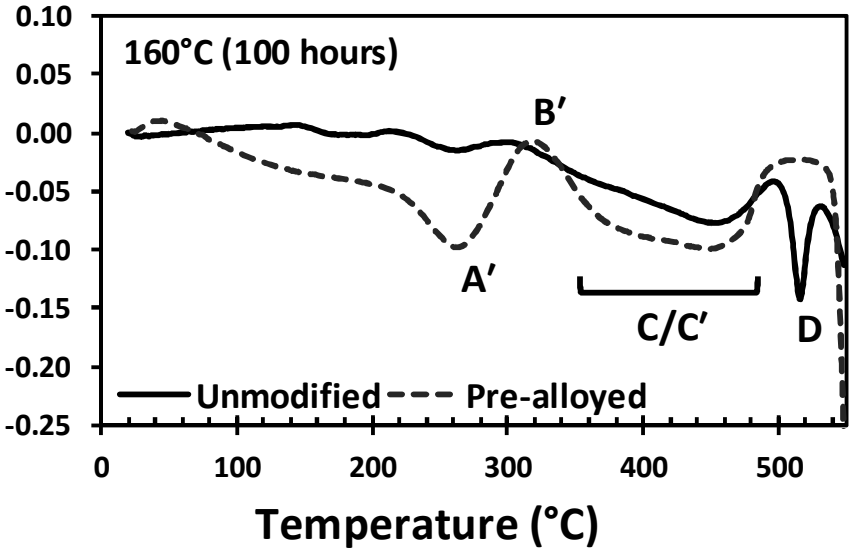

Figure 68 - DSC traces of unmodified and pre-alloyed alloys subject to 160°C for 100 h. Scan rate = 20°C/min.

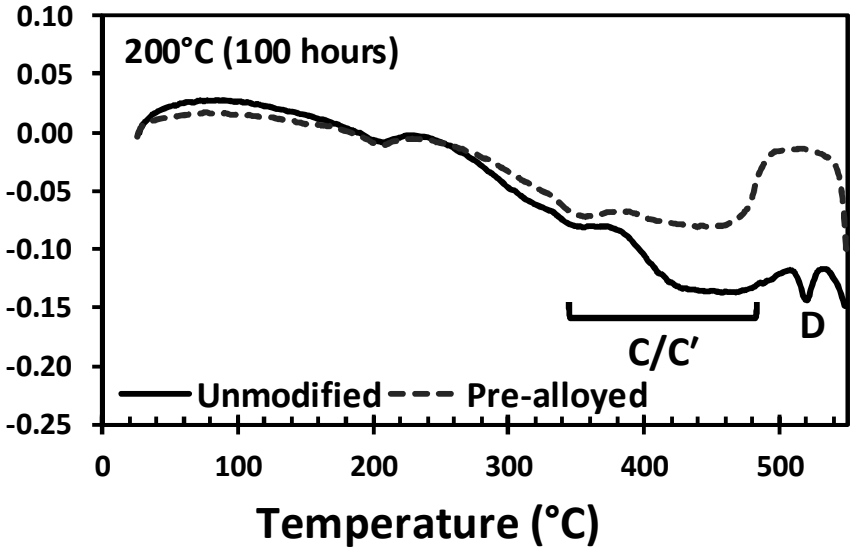

Figure 69 - DSC traces of unmodified and pre-alloyed alloys subject to 200°C for 100 h. Scan rate = 20°C/min.

Table 25 - Temperatures corresponding to peaks A/A' and B/B' acquired from DSC experiments. The temperature range of each heat effect is shown in parentheses.

(100 h) Exposure Temperature	A	A'	B	B'
No Exposure	**243°C** (218-255)	**262°C** (215-284)	**273°C** (255-303)	**312°C** (284-347)
120˚C	**252°C** (207-277)	**261°C** (211-286)	**302°C** (277-330)	**314°C** (286-353)
160˚C	-	**258°C** (213-287)	-	**315°C** (287-352)
200˚C	-	-	-	-

The exact reasoning for the differences in precipitate stability remains unknown. However, it is hypothesized that two factors were likely playing a role. These are the nominal Cu contents of the α-Al grains wherein the precipitation events transpired and the presence of Fe and/or Ni bearing aluminide phases. Prior studies on the microstructure of the alloys [73] have shown that the Cu concentration in grains in the unmodified alloy is nominally the same as the bulk content of the alloy yet lower in the

pre-alloyed material owing to the formation of phases such as Al_7Cu_2Fe and Al_7Cu_4Ni (as also confirmed here in Figure 63). In this sense, the unmodified alloy was largely comparable to wrought 2024 whereas the pre-alloyed material was more representative of a wrought system such as 2618 that contains less Copper and an abundance of dispersoids of intermetallic species such as Al_9FeNi. Owing to their chemical differences, these particular wrought alloys require different aging conditions to attain peak strength. For 2024 the parameters are 10 h at 190°C while 2618 requires a longer aging period of 20 h at a higher temperature of 200°C. This would imply that the precipitates in wrought 2618 are more stable given the higher amount of energy input needed to mature them into a form associated with peak strength. Accordingly, the noted differences in this study between the unmodified alloyed and its pre-alloyed counterpart would seem logical as well.

8.5 Conclusions

Through the research completed in this study the following conclusions have been reached:

1. The pre-alloyed material was successfully processed in an industrial setting. Data on the resultant processing response as well as sintered properties and microstructure of this alloy were essentially identical to prior data derived in a controlled laboratory setting.
2. DSC analyses of the unmodified and pre-alloyed materials in the T6 condition implied that both adhered to a classic S-phase type of precipitation sequence.
3. Isothermal tests revealed that the tensile properties of both alloys were stable during prolonged exposure at 120°C. However, a higher temperature of 280°C prompted over aging in both alloys and appreciable losses in properties such as yield strength for all of the exposure times considered. This was accompanied by appreciable over aging of the S precipitates in the materials as evident through DSC tests and microstructural observations.

4. Isochronal exposure trials (100 h) revealed that the pre-alloyed material was microstructurally and mechanically stable at temperatures as high as 160°C. Under the same conditions, the unmodified alloy experienced measurable degradation. DSC data confirmed that precipitates in the pre-alloyed material offered enhanced thermal stability at temperatures ≤160°C. It was postulated that this fact coupled with the strengthening derived from Fe/Ni-based dispersoids were responsible for the enhanced performance noted in the pre-alloyed system.

Chapter 9 Discussion

Al PM provides a cost effective and environmentally friendly means of creating lightweight, high performance, near net shape automotive components, relative to conventional casting/die casting technology. However, the limited number of commercially available powder blends provides end users with a narrow scope of mechanical properties that has hindered widespread industrial use of this technology. For instance, a number of commercial wrought alloys (i.e. A2618) have been specifically designed for enhanced elevated temperature stability and are now used extensively in the manufacture of high performance pistons. Conversely, no press and sinter Aluminum PM alloys have been designed for similar conditions. Therefore, with the objective of enhancing the elevated temperature stability of Al PM alloys, the PM processing behaviour and elevated temperature properties of an emerging Al-Cu-Mg-Sn PM alloy modified with Fe and/or Ni additions was the focus of this research.

To observe the effectiveness of alloying with Fe and/or Ni, alloys containing 1 wt% Fe, 1 wt% Ni and 1 wt% Fe + 1 wt% Ni were prepared and evaluated. The method of incorporating these transitional metals was a key variable with elemental powders and prealloyed additions considered. In all 7 different blends were assessed in considerable detail. The first phase of research emphasized tests designed to assess the PM processing behaviour of each alloy. This included powder flow rate, apparent density, compressibility, green strength, sintered density/dimensional change, microstructure assessment (SEM, XRD, DSC) and the T6 mechanical properties of each alloy. The most desirable alloy was the identified and subjected to additional experimental work. Here, research was focussed on industrial sintering behaviour and the effects of thermal exposure trials (isothermal and isochronal) under different combinations of exposure time and temperature. The latter involved tensile testing and microstructural assessments through a DSC, XRD, and SEM imaging.

Based on the data achieved through the aforementioned studies the following conclusions were reached:

1. Overall, the compressibility of powder blends containing elemental sources of Fe/Ni was minimally affected. However, pre-alloyed blends achieved slightly inferior green density values while exhibiting superior green strength.
2. Elemental Fe additions were significantly detrimental to the sintering response of the baseline (unmodified) alloy while pre-alloyed Fe additions exhibited superior performance.
3. Elemental Ni additions appeared to have a negligible effect on the physical properties of the baseline alloy in the as-sintered condition. However, tensile testing revealed that it was slightly detrimental to the mechanical properties.
4. The combination of elemental Fe and Ni yielded properties intermediate between those achieved with individual additions.
5. All pre-alloyed additions resulted in a finely dispersed secondary phases within the α-Al grains although a slightly greater amount of residual porosity was also observed.
6. Overall, pre-alloying increased the stiffness of the baseline alloy while decreasing ductility. This was likely a result of the superior hardness of the dispersoid phases contributing to the overall elastic modulus of the alloy.
7. The material that contained 1 wt% Fe + 1 wt% Ni as pre-alloyed additions was identified as the most promising system and was successfully processed in an industrial setting. The sintered properties and microstructure of the alloy were essentially identical to data obtained in the laboratory setting.
8. The pre-alloyed material was successfully processed in an industrial setting. Data on the resultant processing response as well as sintered properties and microstructure of this alloy were essentially identical to prior data derived in a controlled laboratory setting.
9. DSC analyses of the unmodified and pre-alloyed materials in the T6 condition implied that both adhered to a classic S-phase type of precipitation sequence.
10. Isothermal tests revealed that the tensile properties of both alloys were stable during prolonged exposure at 120°C. However, a higher temperature of 280°C prompted over aging in both alloys and appreciable losses in properties such as yield strength for all of the exposure times considered.

References

[1] **Bhanu Prasad, V.V., B.V.R. Bhat, K. Soma Raju., and P. Ramakrishnan**, (2002). *Development of MMC Connecting Rods for Automobile Applications*, Powder Metallurgy in Automotive Applications - II. Vol. 2. 257-266.

[2] **Sankar, R. and Singh, Paramanand**, (2002). *Aging Behaviour of SiC - Particulate Reinforced 7075 Al Alloy Composites Prepared By Mechanical Alloying*, Powder Metallurgy In Automotive Applications - II. Vol. 2. 219-225.

[3] **Purohit., Rajesh, and Rakesh Sagar**, (2002). *Modelling and Simulation of Press Forming of Aluminum-5 Weight % SiCp Composites*, Powder Metallurgy in Automotive Applications - II. Vol. 2. 159-168.

[4] **Mann, Ryan, and D. P. Bishop**, (2010). *Hot Deformation of Aluminum-Copper-Magnesium Powder Metallurgy Alloys*, M.A.Sc. Thesis, Dalhousie University, Halifax, NS.

[5] **German, Randall M**, (2005). *Powder Metallurgy & Particulate Materials Processing*, Metal Powder Industries Federation, Princeton, New Jersey.

[6] **Lawley, Alan**, (1992). *Atomization: the Production of Metal Powders*, Metal Powder Industries Federation, Princeton, N.J..

[7] **German, Randall M. and Seong Jin Park**, (2008). *Mathematical Relations in Particulate Materials Processing: Ceramics, Powder Metals, Cermets, Carbides, Hard Materials, and Minerals*, Wiley, Hoboken, NJ.

[8] **B. Champagne and R. Angers**, (1984). *REP Atomization Mechanisms*, Powder Metall. International. Vol. 16. 125-127.

[9] **Ünal, A., D. D. Leon, T. B. Gurganus, and G. J. Hilderman**, (1998). *Production of Aluminum and Aluminum-Alloy Powder*. ASM Metals Handbook Volume 7 - Metal Powder Technologies and Applications. Vol. 7. 352-354.

[10] **German, Randall M.**, (1989). *Particle Packing Characteristics*. Metal Powder Industries Federation, Princeton, NJ:

[11] **Erhard Klar, C. B. Thompson,** (1998). *Powder Treatment and Lubrication*, ASM Metals Handbook Volume 7 - Metal Powder Technologies and Applications. Vol. 7. 750-760.

[12] **German, Randall M.**, **(**1996). *Sintering Theory and Practice*, Wiley, New York, NJ.

[13] **German, Randall M.**, (1985). *Liquid Phase Sintering*, Plenum, New York, NJ.

[14] **Martin, J. M., and F. Castro**, (2003). *Liquid Phase Sintering of P/M Aluminum Alloys: Effects of Processing Conditions*, Journal of Powder Processing Technology, Vol. 143-144. 814-21.

[15] **Schaffer, G. B., T. B. Sercombe, and R. N. Lumley**, (2001). *Liquid Phase Sintering of Aluminum Alloys*, Materials Chemistry and Physics, Vol. 67. 85-91

[16] **Sundaresan, R., and P. Ramakrishnan**, (1978). *Liquid Phase Sintering of Aluminum Base Alloys*, the International Journal of Powder Metallurgy and Powder Technology, Vol. 14. 9-15.

[17] **Lumley, R. N., and G. B. Schaffer**, (1996). *The Effect of Solubility and Particle Size on Liquid Phase Sintering*. Acta Metallurgica, Vol. 35. 589-595.

[18] **Schaffer, G. B., J. Y. Yao, S. J. Bonner, E. Crossin, S. J. Pas, and A. J. Hill**, (2008). *The Effect of Tin and Nitrogen on Liquid Phase Sintering of Al-Cu-Mg-Si Alloys*, Acta Materialia, Vol. 56. 2615-2624.

[19] **Martin, J. M., and F. Castro**, (2003). *Alloy Development and Associated Dimensional Changes of Aluminum Alloys During Liquid Phase Sintering.* Materials Science, Vol. 426-432. 107-114.

[20] **Murray, J. L.**, (1983). *Al (Aluminum) Binary Phase Diagrams*, ASM Metals Handbook Volume 3 - Alloy Phase Diagrams, Vol. 3. 291.

[21] **McAllister, A. J., and D. J. Kahan**, (1983). *Al (Aluminum) Binary Phase Diagrams*, ASM Metals Handbook Volume 3 - Alloy Phase Diagrams, Vol. 3. 322.

[22] **R. F. Smart and E. C. Ellwood**, (1958). *Introduction to Physical Metallurgy*, McGraw-Hill, New York, NJ, Vol. 181. 833-834.

[23] **R. Q. Guo, P. K. Rohatgi, and D. Nath**, (1997). *Preparation of aluminium-fly ash particulate composite by powder metallurgy technique*. Journal of Materials Science, Vol. 32. 3971-3974.

[24] **Z. A. Munir,** (1979). Journal of Materials Science, Vol. 17. 2733-2740.

[25] **Z. A. Munir**, (1981). Journal of Powder Metallurgy, Vol. 24. 177-180.

[26] **P. K. Higgins and Z. A. Munir**, (1982). *Application of the surface oxide model in the sintering of metallic particles,* Powder Metallurgy International, Vol. 14. 26-29.

[27] **Davis, J. R.**, (1993). *Aluminum and Aluminum Alloys*. ASM International, Materials Park, OH.

[28] **Ecka Granules**, (2007). *ECKA Alumix 13: Press Ready Mix for Aluminum Sintered Parts*, ECKA Granules – Metal Powder Technologies, Product Information sheet.

[29] **Ecka Granules**, (2007). *ECKA Alumix 123: Press Ready Mix for Aluminum Sintered Parts*, ECKA Granules – Metal Powder Technologies, Product Information sheet.

[30] **G. B. Schaffer**, (2006). *Fatigue Crack Propagation in a Sintered 2xxx Series Aluminum Alloy*, Materials Science and Engineering A, Vol. 434. 1-6.

[31] **Boland, C. D., Hexemer Jr. R. L., Donaldson, I. W., Bishop, D. P**., (2010). *On the development of an aluminum P/M alloy for "press-sinter-size" technology,* Proceedings of the 2010 International Conference on Powder Metallurgy and Particulate Materials, Vol. 7. 64-77.

[32] **Boland, C**., (2010). *The Development and Characterization of a Novel Al-Cu-Mg P/M Alloy*, M.A.Sc. Thesis, Dalhousie University, Halifax, NS.

[33] **Rooy, Elwin L.**, (1992). *ASM Handbook: Nonferrous Alloys and Special-purpose Materials – Introduction to Aluminum and Aluminum Alloys,* ASM International, Materials Park, OH.

[34] **Rösler, Joachim, H. Harders, and M. Bäker**, (2007). *Mechanical Behaviour of Engineering Materials: Metals, Ceramics, Polymers, and Composites*, Springer, Berlin, Germany.

[35] **Dieter, George Ellwood**, (1976). *Mechanical Metallurgy*. McGraw-Hill, New York, NJ.

[36] **Kobavasahi, Toshiro**, (2004). *Strength and Toughness of Materials*, Springer, Tokyo, Japan.

[37] **A. A. Alekseev, L. B. Ber, L. G. Klimovich, and O. S. Korobov**, (1978). Phys. Met. Metalloved, Vol. 46. 548-556.

[38] **A. A. Alekseev, L. B. Ber, S. G. Pavlenko, L. G. Klimovich**, (1982). Fiz. Met. Metalloved, Vol. 53. 772-779.

[39] **L. F. Mondolfo**, (1976). *Aluminum Alloys: Structure and Properties*, Butterworths, London, England**.**

[40] **Totten, George E., and D. Scott. MacKenzie**, (2003). *Handbook of Aluminum*, CRC Press, New York, NJ.

[41] **Smith, William F**., (1981). *Structure and Properties of Engineering Alloy,* McGraw-Hill, New York, NJ.

[42] **Wang, S. C., and M. J. Starink**, (2007). *Two Types of S Phase Precipitates in Al-Cu-Mg Alloys*, *Acta Materialia,* Vol. 55. 933-941.

[43] **Singh, S.**, (2005). *Influence of thermomechanical aging on fatigue behaviour of 2014 Al-alloy*, Bulletin of Materials Science, Vol. 28. 91-96.

[44] **Özbek, İ.**, (2007). *A Study on the Re-solution Heat Treatment of AA 2618 Aluminum Alloy*, Journal of Materials Characterization, Vol. 58. 312-317.

[45] **Yu, K.**, (2004). *Mechanical Properties and Microstructure of Aluminum Alloy 2618 with $Al_3(Sc,Zr)$ Phases*, Materials Science and Engineering A, Vol. 368. 88-93.

[46] **Eskin, D. G.**, (2008). *Physical Metallurgy of Direct Chill Casting of Aluminum Alloys*, Solidifications of Aluminum Alloys, CRC/Taylor & Francis. 54-56.

[47] **Feng, Wang**, (2009). *Microstructural Characterization of an Al-Cu-Mg Alloy Containing Fe and Ni*, Journal of Alloys and Compounds, Vol. 487. 445-449

[48] **Kaufman, J. G**., (1999). *Properties of Aluminum Alloys: Tensile, Creep, and Fatigue Data at High and Low Temperatures*, ASM international, Materials Park, OH.

[49] **R.E. Sanders, Jr., G.J. Hildeman, and D.L. Lege**, (1979). *Contract F33615-77-C-5086 Report*, U.S. Air Force Materials Laboratories.

[50] **G.J. Hildeman and R.E. Sanders, Jr**., (1987). *Alloys CU78 and CZ42 for Elevated Temperature Applications, in Wrought P/M Alloys*, U.S. Patent 4,379,719*,* Aluminum Company of America.

[51] **K.S. Chan**, (1989). *Evidence of a Thin Sheet Toughening Mechanism in Al-Fe-X Alloys*, Metallurgical Transactions A*,* Vol. 20. 155-164.

[52] **A.R. Cox**, (1978). *Report FR 100754*, U.S. Air Force Materials Laboratories.

[53] **P.S. Gilman**, **M.S. Zedalis, J.M. Peltier, and S.K. Das**, (1989). *Rapidly Solidified Aluminum, in Transition Metal Alloys for Aerospace Applications*.

[54] **Allied Signal Inc.**, (1989). *Rapidly Solidified Aluminum Al-Fe-V-Si Alloy*, Alloy Dig. FVS 0812, Allied-Signal Laboratories.

[55] **Hummert, Klaus**, (2010). *Aluminium Alloys for Demanding Applications*. International Powder Metallurgy Directory. Proc. of 2010 Hagen Symposium, Germany.

[56] **Dunnett, K. S., R. M. Mueller, and D. P. Bishop**, (2008). *Development of Al-Ni-Mg-(Cu) Aluminum P/M Alloys*, Journal of Materials Processing Technology, Vol. 98. 31-40.

[57] **Xiang, S**., (1999). *An Investigation of the Age Hardening Behavior of PM 2024Al-Fe-Ni Alloys and the Effects of Consolidation Conditions*, *Journal of Materials Science,* Vol. 34. 1953-1958.

[58] **Duan, Xiaoman**, (1991). *Processing of a Modified 2024 Plus 2 Wt. % Fe and 2 Wt. % Ni Aluminum Alloy by Liquid Dynamic Compaction*, Proc. of Advances in Powder Metallurgy - 1991 Powder Metallurgy Conference and Exhibition, Illinoise, Chicago. Vol. 6. 75-82.

[59] **Cooke, R. W., Hexemer Jr. R. L., Donaldson, I. W., Bishop, D. P**., (2011). *Dispersoid Strengthening of Al-Cu-Mg P/M alloy utilising metal additions*, Journal of Powder Metallurgy. 1-10.

[60] **ASTM Standard B964**, (2009). *Standard Tests Methods for Flow Rate of Metal Powders Using Carney Funnel*, ASTM International, West Conshohocken, PA.

[61] **ASTM Standard B703**, (2010). *Standard Tests Method for Apparent Density of Metal Powders and Related Compounds Using the Arnold Meter*, ASTM International, West Conshohocken, PA.

[62] **ASTM Standard B528**, 2010, "Standard Test Method for Transverse Rupture Strength of Metal Powder Specimens" ASTM International, West Conshohocken, PA, 2008, DOI: 10.1520/B0528-10.

[63] **MPIF Standard 42**, (2002). *Method for Determination of Density of Compacted or Sintered Powder Metallurgy Products*, Metal Powder Industries Federation, Princeton, NJ. 59-61.

[64] **MPIF Standard 43**, (2002). *Method for Determination of the Apparent Hardness of Powder Metallurgy Products*, Metal Powder Industries Federation; Princeton, NJ. 63-66.

[65] **MPIF Standard 10**, (2002). *Method for Determination of the Tensile Properties of Powder Metallurgy Materials*, Metal Powder Industries Federation; Princeton, NJ. 31-32.

[66] **Vale INCO ltd.**, (2009). *Type 123 Ni Carbonyl Powder*, Product Information Sheet. Toronto, ON. Canada.

[67] **Hoeganaes Corp.**, (2008). *Ancorsteel 1000 Fe Powder*, Product Data Sheet, Hoeganaes Corp., Cinnaminson, NJ, USA.

[68] **Below, Nikolav A., Andrey A. Aksenov, and Dmitry G. Eskin**, (2005). *Multicomponent Phase Diagrams: Applications for Commercial Aluminum Alloys*, Elsevier, Amsterdam.

[69] **Ducker Research Company**, **(**1996). *Study to Determine Aluminum Content in North American Vehicles in 1996*, Aluminum Association Inc., Arlington, VA.

[70] **Lall, C. and Heath, W.**, (2000). *P/M Aluminum Structural Parts – Manufacturing and Metallurgical Fundamentals*, International Journal of Powder Metallurgy, Vol. 36. 41-43.

[71] **Bishop, D.P.**, (2010*). Recent Advances in the Development of "Press-and-Sinter" Aluminum PM Alloys for the Production of Light Weight Automotive Components*, Proceedings of the 2010 International Conference on Powder Metallurgy and Particulate Materials, Vol. 7. 92-110.

[72] **Kent, D., Schaffer, G.B. and Drennan, J.**, (2005). *Age hardening of a sintered Al-Cu-Mg-Si-(Sn) alloy*, Material Science & Engineering-A. Vol. 405. 65-73.

[73] **Moreau, E.D., Donaldson, I.W., Bishop, D.P.**, (2012). *Effects of Fe and Ni Additions on the Processing and Properties of an Emerging Al-4.4Cu-1.5Mg Powder Metallurgy Alloy*, Canadian Metallurgical Quarterly.

[74] **Cooke, R. W., Hexemer Jr. R. L., Donaldson, I. W., and Bishop, D. P.**, (2011). *Powder Metallurgy Processing of Al-Cu-Mg Alloy with Low Cu/Mg Ratio*, Journal of Powder Metallurgy. 1-7.

[75] **Starink, M.J.**, (2004). *Analysis of Aluminum Based Alloys by Calorimetry: Quantitative Analysis of Reactions and Reaction Kinetics*, International Materials Reviews, Vol. 49. 191-226.

[76] **Polmear, I.J. and Couper M.J.**, (1986). *Design and Development of an Experimental Wrought Aluminum Alloy for Use at Elevated Temperatures*, Metallurgical Transactions A, Vol. 19. 1027-1035.

[77] **Wang, S.C., Starink, M.J., and Gao, N.**, (2006) *Precipitation Hardening in Al-Cu-Mg Alloys Revisited*, Scripta Materialia, Vol. 54. 287-291.

[78] **Wang, S.C., and Starink, M.J.**, (2007). *Two Types of S Phase Precipitates in Al-Cu-Mg Alloys*, Acta Materialia, Vol. 55, 933-941.

[79] **Parel, T.S., Wang, S.C., and Starink, M.J.**, (2010). *Hardening of an Al-Cu-Mg alloy containing Type I and II S phase precipitates*, Materials and Design, Vol. 31. 52-55.

[80] **Perlitz H, Westgren A. And Arkiv Kemi**, (1943). Mineral Geol., Vol. 16.

[81] **Wang, S.C., and Starink, M.J.**. (2009). *The thermodynamics of and Strengthening Due to Co-Clusters: General Theory and Application to the Case of Al-Cu-Mg Alloys*, Acta Materialia, Vol. 57. 2376-2389.

[82] **Starink, M.J., and Wang, S.C.**, (2010). *Comments on "Modeling Differential Scanning Calorimetry Curves of Precipitation in Al-Cu-Mg"*, Scripta Materialia, Vol. 62. 720-723.

[83] **Prince, Alan and Effenberg, Gunter**, (2003). *Aluminium-Copper-Magnesium*. Materials Science International. 547-566.

Appendix A

T1 Properties of PM2324 Alloys

Table I - Mechanical properties PM2324-T1 when modified with additions of 1 wt% Fe.

Alloy (T1)	Hardness (HRB)	E (GPa)	Yield Strength (MPa)	UTS (MPa)	Elongation (%)
Unmodified	***61 ±2***	***68 ±15***	***223 ±10***	***259 ±8***	***1.5 ±0.5***
Elemental Fe	41 ±7	64 ±6	185 ±12	202 ±25	0.8 ±0.3
Pre-Alloyed Fe	62 ±1	71 ±7	216 ±7	264 ±13	1.6 ±0.4

Table II - Mechanical properties PM2324-T1 when modified with additions of 1 wt% Ni.

Alloy (T1)	Hardness (HRB)	E (GPa)	Yield Strength (MPa)	UTS (MPa)	Elongation (%)
Unmodified	***61 ±2***	***68 ±15***	***223 ±10***	***259 ±8***	***1.5 ±0.5***
Elemental Ni	59 ***±2***	64 ±8	194 ±7	215 ±15	0.9 ±0.2
Pre-Alloyed Ni	64 ***±1***	68 ±4	208 ±15	224 ±8	0.8 ±0.3

Table III - Mechanical properties PM2324-T1 when modified with combined additions of 1 wt% Fe and 1 wt% Ni.

Alloy (T1)	Hardness (HRB)	E (GPa)	Yield Strength (MPa)	UTS (MPa)	Elongation (%)
Unmodified	***61 ±2***	***68 ±15***	***223 ±10***	***259 ±8***	***1.5 ±0.5***
Elemental Fe+Ni	54 ***±1***	63 ±5	176 ±5	186 ±7	0.6 ±0.1
Pre-Alloyed Fe+Ni	68 ***±1***	71 ±8	206 ±8	222 ±8	0.6 ±0.3

Table IV – Mean chemistries of the α-Al grains in PM2324-T6 with and without 1 wt% Fe additions.

Alloy (T1)	Mean α-Al Composition (wt%)		
	Al	Cu	Mg
Unmodified	***95.0 ± 0.5***	***4.1 ± 0.5***	***0.9 ± 0.1***
Elemental Fe	94.9 ± 0.6	3.9 ± 0.5	1.2 ± 0.1
Pre-Alloyed Fe	93.9 ± 0.3	4.2 ± 0.4	1.9 ± 0.5

Table IV – Mean chemistries of the α-Al grains in PM2324-T6 with and without 1 wt% Ni additions.

Alloy (T1)	Mean α-Al Composition (wt%)		
	Al	Cu	Mg
Unmodified	***95.0 ± 0.5***	***4.1 ± 0.5***	***0.9 ± 0.1***
Elemental Ni	95.6 ± 0.6	3.3 ± 0.5	1.1 ± 0.1
Pre-Alloyed Ni	94.3 ± 0.6	4.0 ± 0.4	1.6 ± 0.3

Table V – Mean chemistries of the α-Al grains in PM2324-T6 with and without combined 1 wt% Fe and 1 wt% Ni additions.

Alloy (T1)	Mean α-Al Composition (wt%)		
	Al	Cu	Mg
Unmodified	***95.0 ± 0.5***	***4.1 ± 0.5***	***0.9 ± 0.1***
Elemental Fe + Ni	95.0 ± 1.1	3.9 ± 0.8	1.1 ± 0.4
Pre-Alloyed Fe + Ni	94.4 ± 0.6	4.3 ± 0.4	1.2 ± 0.2

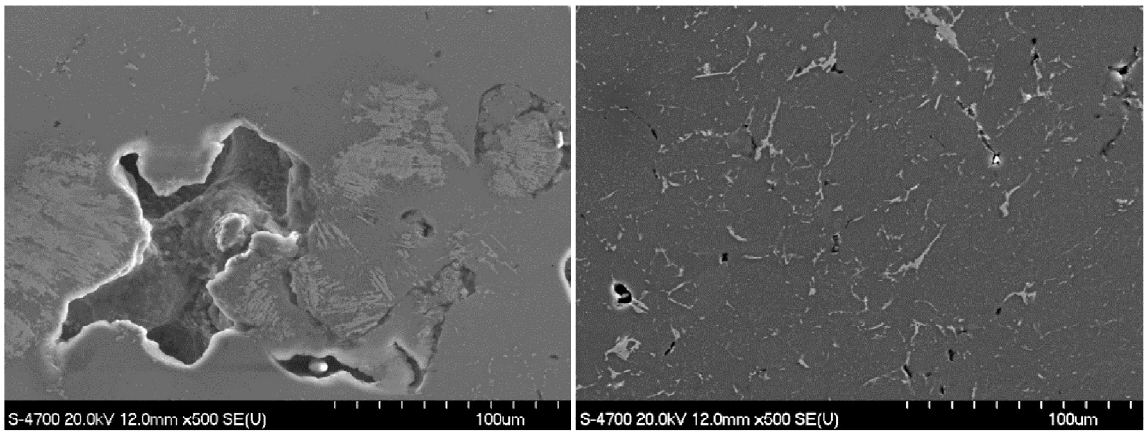

Figure I - SEM images taken of the polished unetched microstructure of elemental (left) and pre-alloyed (right) PM2324 + 1 wt% Fe in the T1 condition.

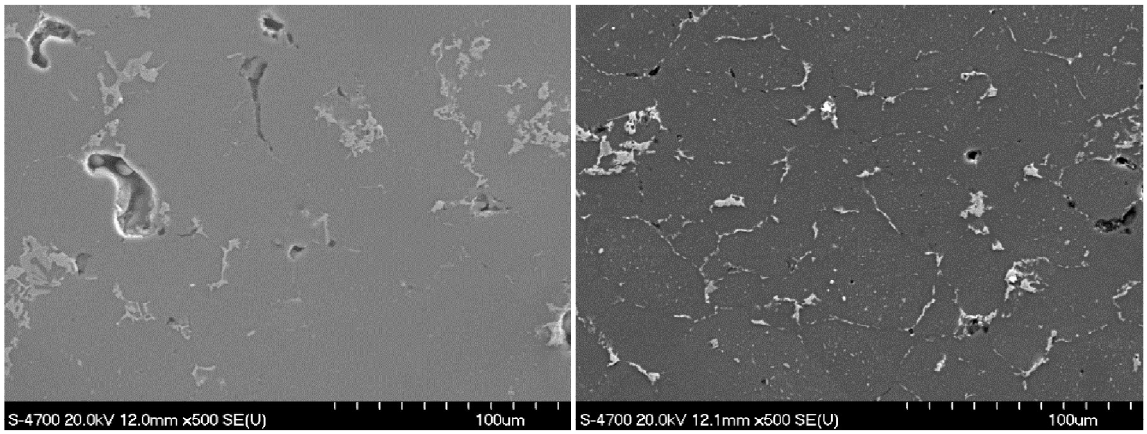

Figure II - SEM images taken of the polished unetched microstructure of elemental (left) and pre-alloyed (right) PM2324 + 1 wt% Ni in the T1 condition.

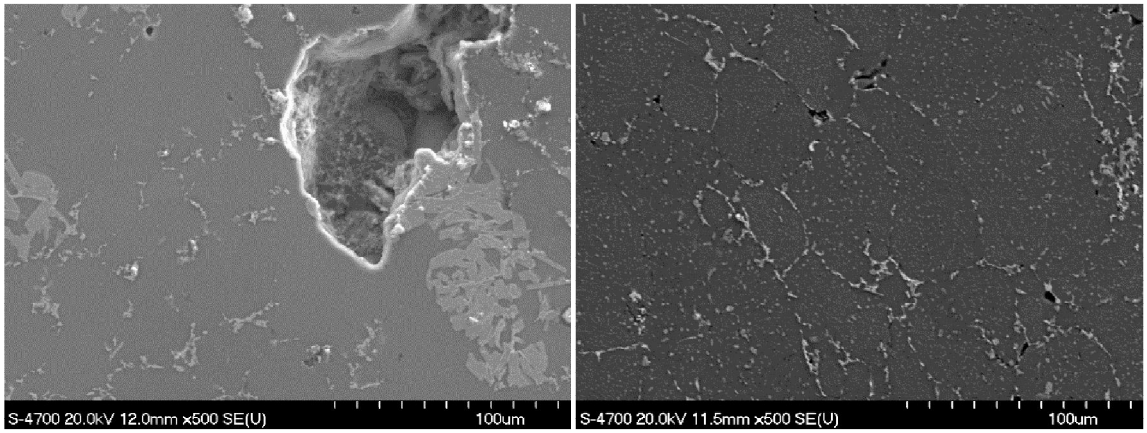

Figure III - SEM images taken of the polished unetched microstructure of elemental (left) and pre-alloyed (right) PM2324 + 1 wt% Fe + 1 wt% Ni in the T1 condition.